Design and Engineering of Hierarchically Porous Transition Metal-based Electrocatalysts for Rechargeable Zn-air Batteries

by

Moon Gyu Park

A thesis

presented to the University of Waterloo

in fulfillment of the thesis requirement for the degree of

Doctor of Philosophy

in

Chemical Engineering

Waterloo, Ontario, Canada, 2019

© Moon Gyu Park 2019

Examining Committee Membership

The following served on the Examining Committee for this thesis. The decision of the Examining Committee is by majority vote.

External Examiner	Dr. De-Tong Jiang
Associate Professor	
Supervisor	Dr. Zhongwei Chen
Professor	
Internal Member	Dr. Eric Croiset
Professor	
Internal Member	Dr. Michael Fowler
Professor	
Internal-external Member	Dr. Adrian Gerlich
Associate Professor	

Author’s Declaration

This thesis consists of material all of which I authored or co-authored: see Statement of Contributions included in the thesis. This is a true copy of the thesis, including any required final revisions, as accepted by my examiners.

I understand that my thesis may be made electronically available to the public.

Statement of Contributions

This thesis is based upon a combination of published works. Various chapters are adapted from the following list of publications, with specific reference to the published work provided within the chapter.

Chapter 4: Park, M. G., D. U. Lee, M. H. Seo, Z. P. Cano, Z. Chen, "3D Ordered Mesoporous Bifunctional Oxygen Catalyst for Electrically Rechargeable Zn-air Batteries", *Small*, 12 (2016) 2707-2714. DOI: https://doi.org/10.1002/smll.201600051

The paper was co-authored by myself, my supervisor, Dr. Lee, De. Seo, and Dr. Cano. In this work, I designed and carried out the experiment, collected and analyzed the characterization results, and wrote the manuscript. Dr. Lee and Dr. Cano assisted the writing of the manuscript. Dr. Seo contributed on the discussion on the electrochemical half-cell testing results. All authors reviewed the manuscript.

Chapter 5: Park, M. G., M. H. Seo, D. U. Lee, X. Wang, W. Ahn, S. H. Noh, S. M. Choi, Z. P. Cano, B. Han, Z. Chen, "Bifunctionally Active and Durable Hierarchically Porous Transition Metal-based Hybrid Electrocatalyst for Rechargeable Metal-Air Batteries", *Applied Catalysis B: Environmental*, 239 (2018) 677-687. DOI: https://doi.org/10.1016/j.apcatb.2018.06.006

The paper was co-authored by myself, my supervisor, Dr. Seo, Dr. Lee, Dr. Wang, Dr. Ahn, Dr. Noh, Dr. Choi, Dr. Cano, and Dr. Han. I and Dr. Seo equally contributed on this research.

I contributed on designing the experiment and synthesis of electrocatalysts, collecting and analyzing the characterization results, and writing the manuscript. The contribution of Dr. Seo is on the computational simulation through density functional theory to investigate the correlation between thermodynamic theory and experimental electrocatalysis. Dr. Lee, Dr. Wang, Dr. Ahn, Dr. Noh, Dr. Choi, Dr. Cano, and Dr. Han helped writing manuscript and discussing the characterization results. All authors reviewed the manuscript.

Chapter 6: Park, M. G., W. Ahn, D. U. Lee, M. H. Seo, G. Jiang, Z. P. Cano, F. M. Hassan, Z. Chen, "Hollow Multivoid Nanocuboids Derived from Ternary Ni–Co–Fe Prussian Blue Analog for Dual-Electrocatalysis of Oxygen and Hydrogen Evolution Reactions", *Advanced Functional Materials*, 28 (2018) 1802129. DOI: https://doi.org/10.1002/adfm.201802129

The paper was co-authored by myself, my supervisor, Dr. Ahn, Dr. Lee, Dr. Seo, Dr. Jiang, Dr. Cano, and Dr. Hassan. I and Dr. Ahn equally contributed on this published work, where I contributed on designing catalyst materials, conducting electrochemical testing of the developed catalysts and physical characterizations such as XRD, SEM, and TEM, as well as writing the manuscript. Dr. Ahn contributed on designing catalysts and carrying out the physical characterizations including XPS and TEM. Dr. Lee, Dr. Seo, Dr. Jiang, Dr. Cano, Dr. Hassan helped writing manuscript and discussing the characterization results. All authors reviewed the manuscript.

Abstract

Electrochemical oxygen reduction reaction (ORR) and oxygen evolution reaction (OER) are the critical cathodic and anodic reactions, respectively, in electrically rechargeable Zn-air battery. With a variety of advantages including relatively high energy density (1218 Wh kg^{-1}), the abundance of zinc in the earth, and secure handling and safe operation, electrically rechargeable (secondary) Zn-air battery technology has been regarded as highly promising energy applications in consumer electronics, electric vehicles, and smart grid storage. Zn-air batteries consist of not only zinc anode, polymer separator, and an alkaline electrolyte that are typical battery components, but also air-breathing cathode that makes Zn-"air" battery unique technology. Unlike other general battery systems such as lithium-ion batteries, there is no active material stored in cathode, but gaseous oxygen molecules in the air are used as the fuel for energy-generating reaction in the air cathode of Zn-air technology. The reactions occurring during battery discharge and charge are ORR and OER, respectively, which are mostly dominating the overall energy efficiency of the Zn-air battery system due to their intrinsically sluggish kinetics. The high energy barrier attributed to conversions between oxygen molecules diffused from the air and hydroxide ions in the electrolyte at the thin layer of the electrode leads to low charge/discharge energy efficiency and insufficient cycle stability hindering the commercialization of rechargeable Zn-air batteries to the market. Therefore, it is necessarily required to facilitate the slow kinetics of oxygen electrocatalytic reactions by using bifunctionally active and durable oxygen electrocatalyst materials to progress the reactions at practically viable and stable rates. With the use of bifunctional oxygen catalysts, kinetics of ORR and OER can be improved, leading to enhancement of Zn-air battery performances such as higher operating

voltage and longer battery cycling life. The current best-known catalysts for ORR and OER are noble metals, including platinum (Pt) and iridium (Ir), respectively. However, high cost and scarcity of the precious metal-based catalysts hinder their employment in large scale energy applications. Furthermore, the electrochemical stability of these materials is well known to be very insufficient for long term usage even under typical device operating conditions. Therefore, the development of non-precious transition metal-based electrocatalysts has significantly been a momentous research field. Along with this movement, the facile synthesis and inexpensive preparation of highly active and durable electrocatalysts will take the top priority for the fulfillment of practically available rechargeable Zn-air battery technology in a variety of energy applications from portable electronics to electric vehicles and smart grid storage systems.

In this work, novel design strategies of bifunctionally active and durable electrocatalysts possessing robust three-dimensional framework with hierarchical porosity are presented. A porous structure with a large surface area is essential to improve the oxygen electrocatalysis since the oxygen reactions take place at the surface of materials, where active sites reside, and thereby the large surface indicating plenty of catalytically active sites enhances kinetics of the reactions. Additionally, the porous architecture facilitates diffusion of oxygen gas molecules during the oxygen electrocatalysis, leading to enhanced mass transport of reactants and reduced overpotentials for ORR and OER polarizations, eventually resulting in improved activities. In addition to the improvement of activities, electrochemical stability is an essential fundamental property for the rational design of electrocatalysts. Thus, the 3D porous structure must have robust framework which can endure the highly oxidative environment in OER potential range. Therefore, the work presented in this thesis is aiming

for the design and engineering of hierarchically porous transition metal-based electrocatalysts involving high porosity as well as electrocatalytically robust frameworks to improve the oxygen electrocatalytic activities and durability and thereby put the rechargeable Zn-air battery technology at a commercially viable level.

In the first study, a facile polymer template-derived method has been used to synthesize three-dimensionally ordered meso/macro-porous (3DOM) spinel cobalt oxide as a bifunctional oxygen electrocatalyst. Physicochemical characterizations have revealed the morphology of the designed electrocatalyst to be a hierarchically meso/macro-porous metal oxide framework. As investigated by electrochemical characterizations, 3DOM Co_3O_4 shows far enhanced ORR and OER activities with improved kinetics compared to the bulk material. The enhancement is majorly attributed to the five times higher specific surface area and significantly greater pore volume, leading to the increased number of catalytic active sites and facilitated diffusion of oxygen molecules into and out of the structure, respectively. Moreover, the robust frameworks of 3DOM Co_3O_4 helps to withstand harsh cycling environments by exhibiting significantly small performance reduction and retaining the original morphology. The improved oxygen electrocatalytic activity and durability have been well demonstrated in the rechargeable Zn-air battery system. 3DOM Co_3O_4 presents remarkably enhanced rechargeability over 200 cycles while retaining quite comparable operating voltage gap in comparison with the precious benchmark catalyst.

In the second study, palladium (Pd) nanoparticle is deposited on the surface of 3DOM Co_3O_4 via a simple chemical reduction process. The morphological advantages of the 3DOM framework, as confirmed in the previous study, are expected to facilitate

diffusion of oxygen molecules into and out of the structure leading to the decreased overpotentials during ORR and OER. However, using metal oxides as electrocatalysts restricts fast electron transfer leading to limited activity for oxygen catalysis due to their intrinsically low electrical conductivity. Therefore, Pd nanoparticles are introduced into 3DOM Co_3O_4 by expecting synergy from the combination of the morphological advantage of 3DOM architecture and the significant thermodynamic stability as well as the excellent ORR activity of palladium metal. Electrochemical characterizations have revealed that the combination demonstrates synergistically improved bifunctional electrocatalytic activity and durability. Moreover, computational simulation via density-functional-theory (DFT) verifies Pd@Co_3O_4(3DOM) is superior in two ways; (i) Activity-wise: the d-band center of Pd deposited on 3DOM Co_3O_4 was found to decrease significantly, resulting in increased electron abundance at the Fermi level, which in turn enhanced the overall electrical conductivity; (ii) Durability-wise: synergistic hybrid of Pd and 3DOM Co_3O_4 resulted in a significantly improved corrosion resistance, due to the much higher carbon oxidation potential and bulk-like dissolution potential of Pd nanoparticles on 3DOM Co_3O_4. The remarkable electrochemical activities and stabilities of Pd@3DOM-Co_3O_4 obtained from the half-cell testing resulted in excellent rechargeability of a prototype Zn-air battery, demonstrating the synergistic introduction of Pd into 3DOM Co_3O_4.

In the last study, a type of metal-organic-framework (MOF) is selected as a template to synthesize MOF-based electrocatalyst possessing robust framework with multi-level porosity. Typically, MOF materials consist of metal centers linked by functional organic ligands, which gives them unique material characteristics such as high porosity and surface area, morphological and compositional flexibility, and high crystallinity. Especially,

transition metal-based Prussian blue analogue (PBA) nanocubes with a chemical formula $M_x^{II}[M_y^{III}(CN)_6]_z \cdot H_2O$, where M^{II} and M^{III} are divalent and trivalent transition metal cations, respectively, are employed as the MOF precursors due to a several material advantages such as simple precipitation synthesis, various possible compositions, and robust structure with high porosity. Specifically, a ternary nickel-cobalt-iron (Ni-Co-Fe) PBA nanocube precursor is designed to maintain the nano-cubic structure while optimizing the composition of transition metal centers for efficient OER and hydrogen evolution reaction (HER) activities for water-splitting technique. Physicochemical characterizations have revealed several advantages of the PBA-derived electrocatalysts, including (i) enlarged active surface area with high porosity and robust architecture, (ii) active nitrogen species formed during synthesis, and (iii) favorably tuned electronic structure by hybridizing the transition metals possessing the different number of valence electrons. This NCF-MOF is highly promising because (i) the unique rigid and interconnected porous structure significantly improves material utilization and allows rapid mass transport to be maintained, (ii) the fine-tuned ternary transition metal composition optimizes the electronic structure to accelerate the intrinsically sluggish OER, and (iii) the in-situ nitrogen-doping during synthesis enhances the interaction of reaction intermediates with active sites during HER. The unique material advantages successfully render reduced overpotential and significant durability for OER and HER, resulting in excellent water-splitting reactions.

Acknowledgments

First of all, I would like to thank my supervisor, Professor Zhongwei Chen, for his continuous support, mentoring, and encouragement throughout my Ph.D. studies. I am deeply impressed with his endless enthusiasm and thirst for academic research. Without his genuine guidance, I could not have accomplished the creation of this Ph.D. thesis.

I would like also express my heartfelt appreciations to my Ph.D. thesis examining committee, including Professor Eric Croiset, Professor Michael Fowler, and Professor Adrian Gerlich from the University of Waterloo, and Professor De-Tong Jiang as my external examiner from University of Guelph for the valuable time and contributions during this important process.

I also wish to thank my friends and colleagues, Dr. Dong Un Lee, Dr. Minho Seo, Dr. Hey Woong Park, Dr. Wook Ahn, Dr. Yun Suk Jun, Dr. Tae-Jung Kwon, Mr. Jun-geun Um, Dr. Ja-Yeon Choi, Mr. Seyoung Kim, Mr. Yong-wook Kim, Mr. Hyunki Bae, Dr. Gaopeng Jiang, Dr. Fu Jing, Dr. Fathy M Hassan, Mr. Zachary P Cano, Dr. Xiaolei Wang, and Dr. Ge Li for their encouragements and companionships in and outside of my school life.

Special thanks go to Dr. Sungho Park for always giving me courage and happiness to enjoy the Waterloo life and for being my mentor with helpful advice for my graduate studies.

Most of all, my deepest gratitude goes to my parents, Ji-Yang Park and Mi Seob Shin, my sibling, Mi Ji Park, for providing a tremendous wealth of unconditional love and sincere support as well as making my life enjoyable and delightful.

Finally, I would like to mention my gratitude to the University of Waterloo for their support and funding. They provided excellent research opportunities during my Ph.D. and allowed me to stay focused on research.

LIST OF FIGURES

LIST OF TABLES

LIST OF ACRONYMS

3DOM – Three-dimensionally ordered mesoporous

ADT – Accelerated durability testing

BET – Brunauer-Emmett-Teller

CNT – Carbon nanotube

CV – Cyclic voltammetry

CP – Chronopotentiometry

DDI – Distilled de-ionized water

EDS – Energy-dispersive X-ray spectroscopy

EES – Electrical energy storage

EV – Electric vehicles

FFT – Fast Fourier transform

GDL – Gas diffusion layer

GO – Graphene oxide

HER – Hydrogen Evolution Reaction

HR-TEM – High-resolution TEM

HR-XPS – High-resolution XPS

Ir/C – Carbon support iridium catalyst

K-L – Koutecky-Levich

LIB – Lithium-ion battery

LSV – Linear sweep voltammetry

MAB – Metal-air battery

NCNT – N-doped carbon nanotube

NP – Nano-particles

OCV – Open circuit voltage

ORR – Oxygen reduction reaction

OER – Oxygen evolution reaction

Pd – Palladium

PS – Polystyrene

Pt/C – Platinum on carbon catalyst

RDE – Rotating disk electrode

RHE – Reversible hydrogen electrode

SAED – Selected area electron diffraction

SCE – Saturated calomel electrode

SEM – Scanning electron microscopy

STEM – Scanning transmission electron microscopy

TEM – Transmission electron microscopy

TGA – Thermogravimetric analysis

XPS – X-ray photoelectron spectroscopy

XRD – X-ray diffraction

ZAB – Zn-air battery

1. Introduction

1.1 Motivation

Currently, most of energy generation and consumption technologies are highly dependent on natural resources such as fossil fuels, including coal, oil, and natural gas. The high dependence on fossil fuels has resulted in a significant increase in petroleum price and environmental issues such as air pollution and world-wide climate change. Specifically, the burning of unsustainable and non-renewable energy sources from nature has triggered the destruction of the ozone layer majorly due to dichloromethane (CH_2Cl_2) and dramatic build-up of greenhouse gases in the atmosphere, leading to unnecessary and tremendous spending for environmental damage recovery. Furthermore, the natural energy resources utilized in the old-fashioned technologies such as combustion engine can no longer meet the current energy requirements due to its limited reserves on Earth. Inevitably, they would face depletion at the current rate of being mined and used, and significantly worsen the environmental conditions along the way. Therefore, the world requires clean energy production through a cost-effective method, which can be called alternative sustainable energy generation and storage systems, as the next-generation energy technology to avoid the issues mentioned above. Having said this, novel energy harvesting, conversion and storage technologies such as batteries, supercapacitors, and fuel cells, have attracted tremendous attention as potentially realistic solutions for meeting the rapidly increasing energy demands in the modern society and offering low or net-zero carbon emission, high-efficiency, and excellent energy sustainability.

To date, lithium-ion battery (LIB) technology is the most developed and widely utilized energy storage system for a variety of energy applications from portable electronics such as

smartphones and laptops in small-sized forms to electric vehicles (EVs) and energy storage systems (ESS) in large-sized forms. This is owing to numerous advantages over other energy technologies such as nickel-cadmium (Ni-Cd), lead-acid, and nickel-metal hydride (Ni-MH) batteries.[1-3] However, despite the many advantages, LIB has limited energy density majorly depending on the limited amount of active materials that should be stored inside the battery.[4] This shortcoming stems of fundamental electrochemistry of LIBs which undergo intercalation/de-intercalation reactions between the negative and positive electrodes and the utilization of irreversible and non-sustainable intercalation compound in the positive electrode considerably decreases the energy density resulting in the significantly increased cost of batteries.[5-8] Therefore, the limitation in the energy density of LIB would hinder the fulfillment of ultimate price and energy density requirements for highly energy-intensive applications such as electric vehicles (EVs).

As one of the proposed alternative energy harvesting and storage technology to LIB, electrically rechargeable metal-air batteries have recently drawn a world-wide interest due to their extremely high energy density compared to that of other types of batteries**,** making them practically viable to potentially fulfill EV range requirements. The metal-air batteries consist of characteristics of both batteries and fuel-cells. The usage of metal as an anode, liquid electrolyte, and separator is from the concept of batteries, and the utilization of a highly porous electrode as a cathode is from the feature of fuel cells. The noticeable feature of the metal-air battery technology is an open cell structure in which oxygen gas molecules from the air are utilized as an inexhaustible fuel source at an air-breathing cathode. In contrast, lithium-ion batteries (LIBs) must carry the fuel (intercalation compounds) inside the battery, the amount of which is limited by the size of the battery. Therefore, the absence of cathode active material that must be stored

inside the cathode reduces the total volume and weight of the metal-air battery systems, which eventually enhances energy densities about 2-10 times higher than those of the LIBs.[9, 10]

According to the type of metal in the anode, metal-air batteries achieve various energy densities and operating voltage, where the name of metal-air batteries depends on the metal used as the anode. There are several types of metal-air batteries, as shown in the following **Figure 1-1** and **Table 1-1**, where they are generally classified into two groups by the type of used electrolytes, which are aqueous and non-aqueous (organic). One group using aqueous electrolyte includes Zn-air, Fe-air, Al-air, and Mg-air batteries; such systems are not sensitive to moisture, whereas the other group employing non-aqueous electrolyte involves Li-air, Na-air, and K-air batteries which are water-sensitive making their system highly complicated and non-practical.

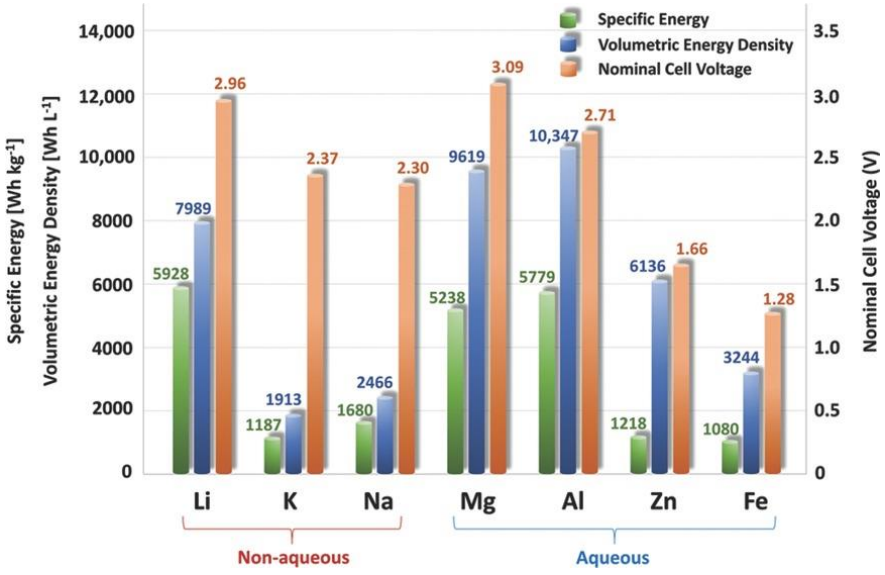

Figure 1-1. Theoretical specific energies, volumetric energy densities, and nominal cell voltages for various metal anodes in aqueous and non-aqueous metal–air batteries. Specific energy values account for oxygen uptake in the battery by numeric integration between the fully charged and fully discharged states. Volumetric energy densities were calculated using the density of the anode in the fully discharged state. Refer to the Supporting Information for calculations and further explanations. Reproduced from reference 11, with permission from the Wiley-VCH (2016).[11]

Battery Systems	Specific Capacity (Ah kg^{-1})	Specific energy density (Wh kg^{-1})	Volumetric Energy density (Wh L^{-1})	Theoretical cell voltage with O_2 (V)	Practical operating voltage (V)	Primary or Rechargeable
Fe-air	844	1080	3244	1.28	1.0	Rechargeable
Zn-air	733	1218	6136	1.65	1.0 - 1.2	Rechargeable
Al-air	2132	5779	10347	2.71	1.1 - 1.4	Primary
Mg-air	1695	5238	9619	3.09	1.2 - 1.4	Primary
Na-air	1072	1680	2466	2.30	2.0 - 2.1	Rechargeable
K-air	501	1187	1913	2.37	2.2 - 2.4	Rechargeable
Li-air	2003	5928	7989	2.96	2.4 - 2.6	Rechargeable

Table 1-1. Characteristic data of various metal-air batteries[11]

Among the non-aqueous systems, Li-air battery, particularly, has been highly attractive alternative energy storage systems owing to its extremely high theoretical energy density and working voltage, 5928 Wh kg^{-1} and 2.96 V, respectively. However, the battery chemistry in aprotic solvents occurs at a much slower rate than in aqueous electrolytes due to the formation of insoluble metal peroxide or superoxide particles leading to electrolyte decomposition. This results in the accumulation of the undesirable materials in the air electrode, not only clogging pores in the electrode and interrupting oxygen diffusion but also gradually shutting off the battery reactions. Additionally, metal availability, high price, and safety concerns of the Li-air battery systems hamper their development and further commercialization. The Na-air and K-air batteries have similar problems to the Li-air battery technology, keeping them from being developed and commercialized. Although the non-aqueous metal-air batteries have tremendous potential, without doubt, they, unfortunately, are tormented by the intrinsic performance limitations containing low power capability and poor cycleability.

1.2 Background and Fundamentals of Rechargeable Zn-Air Batteries

As one of the aqueous electrolyte metal-air batteries, Zn-air battery, in particular, is one of the most promising energy technologies as the next generation energy conversion and storage application. Compared with other metals, Zn metal has various advantages, including high abundance and low cost, and low equilibrium potential. Furthermore, Zn-air single-cell features easy and safe operation, environmental benignity, flat discharge voltage, and long cycle-life in alkaline media.[9, 12-14] More importantly, the fabrication of Zn-air batteries can be done under ambient conditions, while other metals such as lithium, sodium, and potassium require an inert atmosphere (such as in glovebox) for handling and fabricating batteries, which is indicative of that mass production of Zn-air batteries could be much more inexpensive and scalable.

Generally, Zn–air batteries are capable of generating high theoretical energy density of 1218 Wh kg^{-1}, which is about five times higher than that of the current lithium-ion batteries (LIBs). Although Zn-air batteries have inferior gravimetric energy density in comparison to that of Li-air batteries, when normalized volumetrically, Zn-air batteries have notably higher practical volumetric energy density than Li-air batteries owing to much higher atomic density of zinc metal (**Figure 1-2**). The volumetric energy densities are often considered more important in some specific energy applications such as electric passenger vehicles, which is generally due to a limited space for battery installation. Therefore, Zn-air battery has been encouraged as the most feasible alternative energy technology to substitute the current LIBs for future long-range electric passenger vehicle applications.[11]

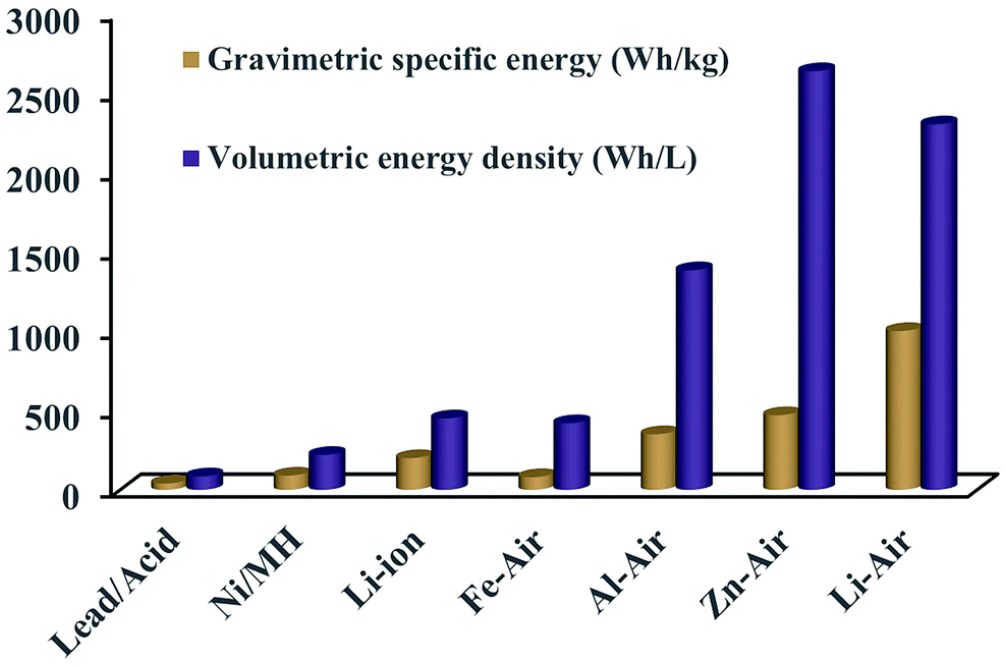

Figure 1-2. Practical gravimetric specific energy and volumetric energy density of rechargeable battery technologies. Reproduced from reference 15, with permission from the Royal Society of Chemistry (2016).[15]

The typical rechargeable Zn-air battery consists of zinc anode, aqueous alkaline electrolyte of 6M KOH, polymer membrane separator, and catalyst coated air-breathing cathode. When discharging the Zn-air battery, oxygen from the air diffuses into the open-structured porous cathode, followed by a reduction process into hydroxide ions (OH^-) at the three-phase reaction surface at which electrolyte (liquid), catalyst (solid), and the oxygen molecule (gas) encounter, eventually accomplishing oxygen reduction reaction (ORR), as shown in **Figure 1-3** below:

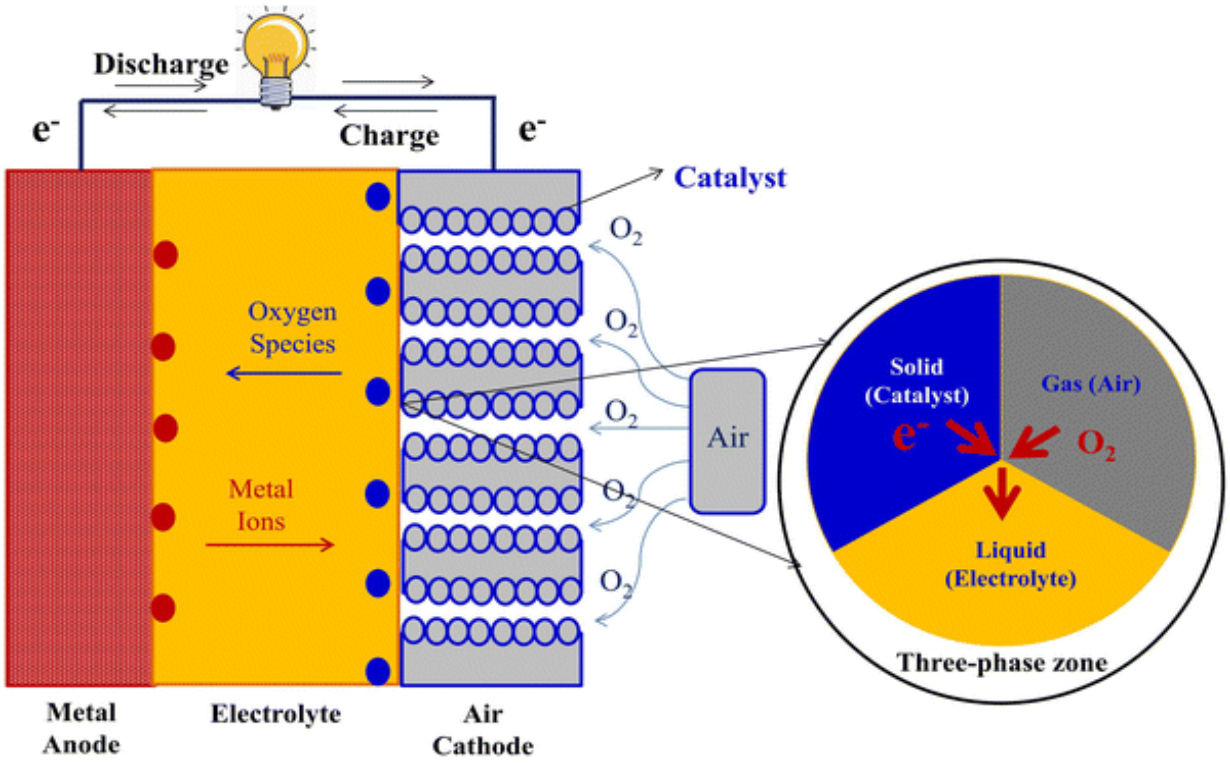

Figure 1-3. A basic metal-air battery (MAB) configuration with a simplified solid–liquid–gas three-phase zone. Reproduced from reference 16, with permission from the Springer (2018).[16]

In the anode part, zinc metal simultaneously is oxidized into zinc ion (Zn^{2+}) and eventually forms zincate ion ($Zn(OH)_4^{2-}$) and zinc oxide (ZnO), resulting from a reaction with hydroxide ions (OH^-) which are migrated from the cathode where ORR takes place. In contrast, during the Zn-air battery charging, the electrochemical processes are reversely implemented, leading to the evolution of gaseous oxygen molecules in the air-breathing cathode, which is an oxygen evolution reaction (OER), while the zincate ions in the electrolyte is reduced back to the zinc anode. By combining the anode and cathode reactions, the overall theoretical battery voltage, typically called "open-circuit voltage (OCV)" of the Zn-air battery, becomes 1.65 V, where $E_{battery} = E_{cathode} - E_{anode}$. The electrochemical reactions of Zn-air are shown below:

$$Anode: Zn + 4OH^- \rightarrow Zn(OH_4)^{2-} + 2e^-$$

$$(E_{anode} = -1.25\,V\,(vs.SHE))$$

$$Zn(OH_4)^{2-} \rightarrow ZnO + H_2O + 2OH^-$$

$$Cathode: O_2 + 4e^- + 2H_2O \rightarrow 4OH^-$$

$$(E_{cathode} = 0.4\,V\,(vs.SHE))$$

$$Overall: 2Zn + O_2 \rightarrow 2ZnO$$

$$E_{battery} = 1.65\,V\,(vs.SHE)$$

Although the theoretical equilibrium potential of the rechargeable Zn-air battery is 1.65 V, the practical discharging voltage is around 1.2 V that is far less than 1.65 V, as shown in **Table 1-1** above. Furthermore, the charging voltage is generally higher than 2 V, which indicates there is substantial energy loss, which is called "overpotential", which is attributed to the activation, ohmic, and concentration losses generated from various resistive reactions during the battery operation.

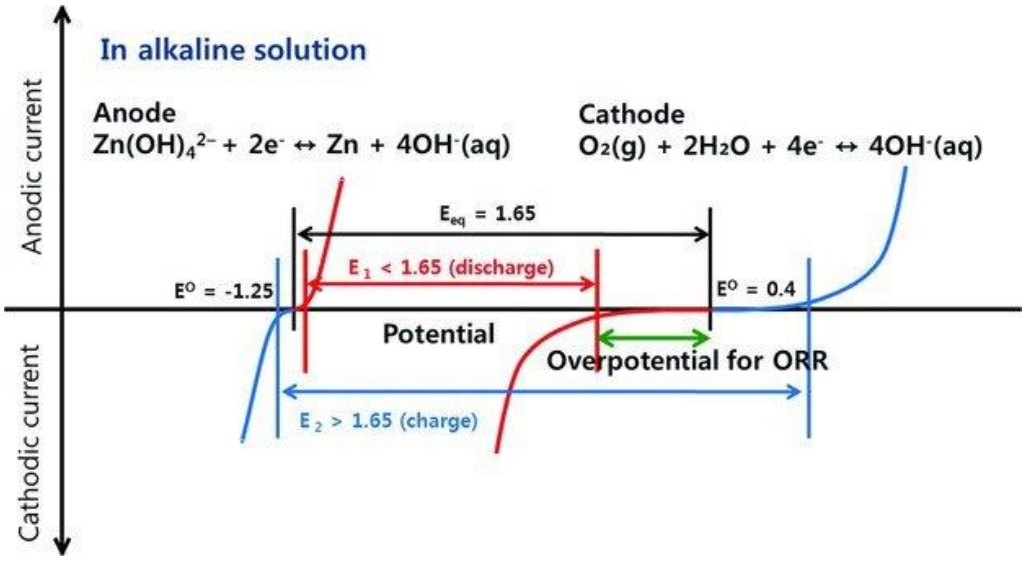

Figure 1-4. Schematic polarization curves of the Zn-air cell. The equilibrium potential of the Zn-air cell (black line) is 1.65 V, but the practical voltage (red line) in discharge is lower than 1.65 V due to the sluggish ORR. A large potential is needed to charge Zn-air battery, higher than the equilibrium potential (blue line). Reproduced from reference 17, with permission from the Wiley-VCH (2011).[17]

An illustration showing polarization curves of Zn-air battery is demonstrated in **Figure 1-4**. Fundamentally, the theoretical equilibrium potential of the Zn-air battery is 1.65 V, and it is highlighted in black lines. The cathodic current occurs at the air electrode (cathode at the right), and the anodic current occurs at the zinc electrode (anode at the left), where the red lines and the blue lines demonstrate current profiles during discharge process and charge process, respectively. Apparently, a big overpotential (green line) indicates the large loss of energy during battery discharge process. Similarly, a large overpotential is also required to charge the battery, demonstrating much more significant voltage loss is carried out in the cathode (air-electrode) than in the anode (zinc). Specifically, at the air-breathing electrode, the both ORR and OER are key reactions in this system since their very slow reaction kinetics derived from high activation barriers significantly reduce overall battery performance consisting of energy density, power density, rechargeability, and energy efficiency. Therefore, a variety of scientific research efforts have been contributed to the battery components such as zinc anode, electrolyte, and catalyst-coated air-electrode to reduce the significant voltage losses during the battery discharge and charge. However, since the overpotentials associated with the zinc electrode and electrolyte are far less than that regarding the air-electrode, specifically at the three-phase interface, most of the studies have focused on the development of efficient electrochemical catalyst materials and air-breathing electrode.

As mentioned above, the significant energy loss is attributed to the considerable energy barriers of the ORR and OER, which must be sufficiently reduced to minimize the degradation and enhance the overall battery performance. By using electrochemical catalyst materials, as known as electrocatalysts, the activation energies for transferring electrons during the oxygen

reactions can be decreased, leading to reduction of the overpotentials. Typically, most of the electrocatalysts are only functional toward either ORR or OER due to their oppositeness, where ORR-active electrocatalysts typically have insufficient activity toward OER whereas OER-active electrocatalysts have unsatisfactory activity toward ORR. Accordingly, it is challenging to develop a highly active material toward both ORR and OER, which is "bifunctional" electrocatalysts, and this will be the ultimate goal of this thesis. To better understand the fundamentals of the oxygen electrocatalysis and the material design, more details regarding the oxygen reaction mechanisms and a variety of strategies for designing and engineering bifunctional electrocatalysts will be introduced in the following parts.

1.3 Theory and Principle of Oxygen Electrocatalysis

The overall energy efficiency of the Zn-air battery is significantly pertinent to the reaction kinetics of oxygen electrocatalysis, such as ORR and OER. Therefore, their intrinsically sluggish reaction rates due to high activation energy barrier are required to be facilitated by using bifunctional electrocatalysts, while enabling simple battery design and architecture, to realize commercially available energy application of rechargeable Zn-air battery. Accordingly, the fundamentals of ORR and OER will be introduced in the following parts.

1.3.1 Oxygen Reduction Reaction (ORR)

Oxygen reduction reaction (ORR) is a primary electrochemical reaction that governs the operation of metal-air batteries (MABs) and fuel cells (FCs). By applying catalytically active materials on a gas diffusion layer (GDL) to form active cathode in these energy systems, the

overpotentials of ORR can be significantly reduced to perform the reaction much efficiently. For the mechanism of ORR, there are two adsorption types as presented in **Figure 1-5**, where one is bidentate O_2 adsorption ((a), two oxygen atoms coordinate with the active site), and the other is end-on O_2 adsorption ((b), one O atom coordinate perpendicularly to the active site), completing the four-electron pathway and the two-electron pathway, respectively.

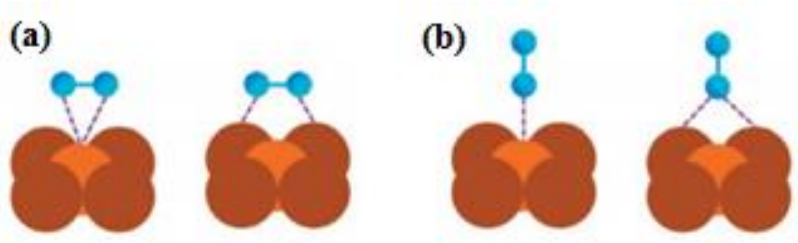

Figure 1-5. O_2 adsorption models on catalyst surfaces: (a) bidentate O_2 adsorption, (b) end-on O_2 adsorption. Reproduced from reference 18, with permission from the Royal Society of Chemistry (2012).[18]

The corresponding reactions of the bidentate adsorption are as follows:[18-20]

$$O_2 + 2H_2O + 2e^- \rightarrow 2OH_{ads} + 2OH^-$$

$$2OH_{ads} + 2e^- \rightarrow 2OH^-$$

$$Overall: O_2 + 2H_2O + 4e^- \rightarrow 4OH^-$$

For the end-on adsorption, the reactions are as follows:

$$O_2 + H_2O + e^- \rightarrow OOH_{ads} + OH^-$$

$$OOH_{ads} + e^- \rightarrow OOH^-$$

$$Overall: O_2 + H_2O + 2e^- \rightarrow OOH^- + OH^-$$

The above two-electron reaction may be followed by either a further two-electron reduction of peroxide or by the chemical disproportionation of peroxide, as shown below:

$$OOH^- + H_2O + 2e^- \rightarrow 3OH^-$$

$$or\ 2HO_2{}^- \rightarrow 2OH^- + O_2$$

The two types of classical oxygen catalysts are transition metals and metal oxides, and the mechanism of the electrochemical oxygen reactions using these catalysts have been intensively studied. For transition metal-based catalysts, the two-electron reduction was reported for less active transition metals such as Co, Ni, Fe, and Mn. On the other hand, regarding the most active ORR catalyst, platinum (Pt)-based materials, the four-electron reduction is generally believed.

Based on the above possible pathways, many researchers have dedicated to identify the rate-determining step (RDS) and understand the exact sequence of the electron transfer. Generally, the kinetics of ORR on the transition metal-based electrocatalysts are mainly hampered by three steps: (1) the first electron transfer of ORR; (2) the hydration of oxygen; and (3) the desorption of the oxygen intermediates such as O^*, OH^*, and OOH^*. For metals holding oxygen molecule too strongly, the reaction rate is restricted due to the removal process of the adsorbed oxygen intermediates. In contrast, in terms of metal surfaces binding oxygen molecule too weakly, the reaction rate is limited due to the dissociation of gaseous oxygen molecule, or more likely, the electron transfer to the adsorbed gaseous oxygen molecule.

For transition metal oxide catalysts, such as spinel cobalt oxide (Co_3O_4), the reaction pathways at the surface follow the same principle, but with a different charge distribution. The surface cations of stoichiometric oxides are not fully coordinated with oxygen atoms, while

anion coordination is completed by the oxygen from a water molecule in aqueous electrolyte. As a result, the reduction of the surface cation conducted by an electron from the external circuit is charge-compensated by protonation of a surface oxygen ligand. The reaction pathway of ORR on a metal oxide catalyst is shown below:[19]

$$2M^{m+}\cdots O^{2-} + 2H_2O + 2e^- \rightarrow 2M^{(m-1)+}\cdots OH^- + 2OH^-$$

$$O^2 + e^- \rightarrow {O_{2,ads}}^-$$

$$2M^{(m-1)+}\cdots OH^- + {O_{2,ads}}^- + e^- \rightarrow 2M^{m+}\cdots O^{2-} + 2OH^-$$

or more probably

$$M^{m+}\cdots O^{2-} + H_2O + e^- \rightarrow M^{(m-1)+}\cdots OH^- + OH^-$$

$$O^2 + e^- \rightarrow {O_{2,ads}}^-$$

$$M^{(m-1)+}\cdots OH^- + {O_{2,ads}}^- \rightarrow M^{m+}\cdots O\cdots O^{2-} + OH^-$$

$$M^{m+}\cdots O\cdots O^{2-} + H_2O + e^- \rightarrow M^{(m-1)+}\cdots O\cdots OH^- + OH^-$$

$$M^{(m-1)+}\cdots O\cdots OH^- + e^- \rightarrow M^{m+}\cdots O^{2-} + OH^-$$

The ORR pathways and mechanisms may vary depending on the electrocatalysts utilized and its surface electronic structure. For instance, the degree of σ* orbital and the metal-oxygen covalency have an influence on the competition between O_2^{2-}/OH^- displacement and OH^- regeneration on the surface of transition-metal ions as the RDS of the ORR. This highlights the importance of the electronic structure of metal oxide catalysts in controlling the catalytic activity.

In spite of the considerable studies and researches for uncovering the reaction mechanisms for more than decades, atomic and molecular-level understanding of the ORR mechanism is still in its early stages owing to the highly complicated ORR kinetics. However, it has been known that the complete electrochemical ORR involves four net electron transfers to oxygen molecules at the cathode. There are several pathways for electrochemical O_2 reduction:[20]

(i) a ‘‘direct’’ four-electron reduction to OH (alkaline media)

(ii) a two-electron pathway contains a reduction of oxygen molecules to hydrogen peroxides

(iii) a ‘‘series’’ pathway with two- and four-electron reduction

(iv) a ‘‘parallel’’ pathway that is a combination of (i), (ii), and (iii)

(v) an associative mechanism contains the adsorption of molecular O_2 and direct electron transfer to it and to OOH, which breaks into O and OH

(vi) a dissociative mechanism includes the splitting of the O–O bond in O_2 and the hydrogenation of atomic O to OH and H_2O

1.3.2 Oxygen Evolution Reaction (OER)

Oxygen evolution reaction is a vital reaction, which is still being investigated and explored to understand their mechanism on different catalyst surfaces. As mentioned in the previous sections, OER typically happens during the charging process of Zn-air batteries and electrolysis in the electrolyzer system. The OER can be considered an opposite reaction of ORR and HER, as OH^- ions are oxidized during charging Zn-air battery as against the reduction process of O_2 during the discharging of Zn-air batteries, and as the oxygen gas evolved at the anode as against the hydrogen gas evolved at the cathode in the electrolyzers, respectively. In this section, OER and HER will be discussed together based more on water electrolysis technology.

Water electrolysis is a process of electrically splitting water into oxygen and hydrogen. The overall water electrolysis can be described by the following equation:[21, 22]

$$2H_2O \rightarrow 2H_2 + O_2$$

Since acidic water splitting typically suffers from the use of scarce and expensive acid-insoluble OER catalysts with cognitive activity, the water splitting in the alkaline electrolyte has emerged as a strong candidate for commercialization toward mass hydrogen production. Hence, it is highly attractive to develop a precious-metal-free active and durable electrocatalyst that is efficient for both OER and HER in strong alkaline media.

The overall process is composed of OER on the anode and HER on the cathode of the electrolyzer. Notably, in alkaline media (pH 14), the corresponding anode and cathode reactions are:

$$4OH^- \rightarrow O_2 + 2H_2O + 4e^- \quad E^o{}_a = 0.404\ \text{V} \quad \text{(OER, anode reaction)}$$

$$4H_2O + 4e^- \rightarrow 2H_2 + 4OH^- \quad E^o{}_c = -0.826\ \text{V} \quad \text{(HER, cathode reaction)}$$

Where $E^o{}_c$ and $E^o{}_a$ are the equilibrium half-cell potentials at standard conditions of 1 atm and 25 ^{o}C. Thus at standard conditions, the equilibrium (reversible) potential is 1.23 V for water electrolysis.

The proposed OER mechanism under alkaline conditions is shown below:[22]

$$M + OH^- \rightarrow M \cdots OH + e^-$$

$$M \cdots OH + OH^- \rightarrow M \cdots O + H_2O + e^-$$

$$M \cdots O + OH^- \rightarrow M \cdots O \cdots OH + e^-$$

$$M \cdots O \cdots OH + OH^- \rightarrow M + O_2 + H_2O + e^-$$

$$\boldsymbol{Overall: 4OH^- \rightarrow O_2 + 2H_2O + 4e^-}$$

Like the above elemental reaction steps proposed, the OER pathways and mechanisms are considerably complicated. Since oxygen is generally evolved from an oxide phase, rather than bare metals, the reaction mechanisms may vary depending on the electrode materials possessing different site geometry of the metal cations. The multi-valence characteristic of transition metal ions is indispensable for catalyzing OER since the reaction is induced from the interaction between the metal ions and the oxygen intermediates such as O^*, OH^*, and OOH^*, and the formation of a bond by changing their valence state. The site geometry of the transition metal cations changes the adsorption energy of the oxygen species, which further determines OER kinetics. For a transition metal oxide electrocatalyst involving surface reactions M^{m+}-O^{2-} = $M^{(m-1)+}$-O^- biased towards the right-hand side, the OER in alkaline electrolyte proceeds as presented below:[19]

$$M^{m+} - O^{2-} + OH^- \rightarrow M^{(m-1)+} \cdots O \cdots OH^- + e^-$$

$$M^{(m-1)+} \cdots O \cdots OH^- + OH^- \rightarrow M^{m+} \cdots O \cdots O^{2-} + H_2O + e^-$$

$$2M^{m+} \cdots O \cdots O^{2-} \rightarrow 2M^{m+} \cdots O^{2-} + O_2$$

Although providing an effective method to produce high-purity oxygen and hydrogen, electrolyzers' practical utilization for mass production of the gases is limited, since OER and HER are sharply uphill reactions with large overpotentials, where commercially available electrolysis systems typically operate at a cell voltage of 1.8–2.0 V which is much higher than the theoretical value of 1.23 V.[23] Therefore, active electrocatalysts for anodic OER and cathodic

HER are indispensably required to minimize the large water-splitting overpotentials, making the process more efficient and consequently achieving fast kinetics for practical applications.[22, 24, 25]

Among a wide variety of available electrocatalysts, platinum (Pt)-group metals show invincible electrocatalytic HER performance, including extremely high exchange current density. Contrarily, OER in alkaline media is more complicated due to the high number of steps involved. The best-known catalysts for OER consist of less abundant and expensive Ir- and Ru-based compounds. However, to gain sustainable oxygen and hydrogen productions, replacement of low-abundance, expensive, and especially poorly unstable noble metal-based catalysts like Pt, Ir, and Ru with cost-effective and environmentally benign alternatives would be highly desirable. Therefore, it is attractive to design and develop efficient OER and HER catalysts via using earth-abundant elements particularly non-precious transition metals. More details with respect to the development of advanced electrocatalysts will be discussed in the following section.

1.4 Bifunctional Oxygen Electrocatalysts

1.4.1 Precious Metal-based Catalysts

Conventionally, the best-known catalysts for ORR and OER are precious metals based catalysts representatively including platinum (Pt), iridium (Ir), and ruthenium (Ru). However, the use of these precious metal-based catalysts for large scale applications such as electric vehicles and energy storage systems is prohibitively expensive due to their scarcity.[20-22] Additionally, the durability of these catalysts has been reported to be insufficient for long-term usage under normal device operating conditions. Perhaps most importantly, the precious metal-based catalysts are vigorously active towards only one of the two oxygen reactions required for

rechargeable applications. For example, carbon-supported platinum (Pt/C) is an excellent ORR catalyst, while carbon-supported iridium (Ir/C) is a strong OER active catalyst. Recently in the literature, a simple physical mixture of these two catalysts have been used to render bifunctionality, but this method is very rudimentary and still requires two separate syntheses for each catalyst.

In this regard, it is thus required to design and develop efficient bifunctional electrocatalysts with low cost, environmentally benignity, and enhanced activity and durability, where the single material should be capable of catalyzing both ORR and OER over the same active surface. In addition to the bifunctional activity, electrochemical stability is also essential when it comes to practicality, where a catalyst possessing a great bifunctional activity that lasts only a few times will not be used. It is required for the bifunctionally active catalyst to withstand both strongly reducing and oxidizing environments during ORR and OER, respectively, while delivering significant bifunctional activities. Therefore, if it is to be considered for commercialization, the catalyst must be able to withstand thousands of cycles before needing to be replaced.

In parallel, the discharge and charge efficiency of the Zn-air battery is directly relevant to the intrinsically slow kinetics of the oxygen electrocatalysis, and it is necessary to progress them at practically viable rates by using bifunctional electrocatalysts. Additionally, the use of bifunctional catalysts in a single air-breathing cathode renders a simple battery design and architecture, which is desired for commercialization of the system. The following section discusses promising alternative materials that can replace the precious metal-based catalysts and be appropriately used for rechargeable Zn-air systems, which will be followed by rational design strategies of the materials.

1.4.2 Design and Engineering of Non-precious Transition Metal-based Catalyst

Generally speaking, efficient bifunctional electrocatalysts should demonstrate sufficiently low overpotentials towards both ORR and OER, alongside with reasonable current densities as well as long stability. Regarding the development of efficient bifunctional electrocatalysts, the selection of an appropriate material should contain various vital factors such as electrocatalytic activity, cost of materials and fabrication, thermodynamic stability, and corrosion resistance. These properties are tunable by changing the composition and morphology of the catalyst, as well as synthetic procedures. The composition is directly relevant to the crystal and electronic structures of the materials, which can affect the firmness of bonding between the catalyst surface and the oxygen intermediates, determining the electrocatalytic activity. Additionally, the morphology is highly associated with the active surface area, density of the active sites, and structural porosity, which can determine mass transport and diffusion effects of the reactants and corresponding intermediates.

As the alternative materials of the impractical precious metal catalysts, non-precious transition metals such as cobalt (Co), nickel (Ni), iron (Fe), and manganese (Mn) have garnered much research attention owing to not only their high abundance and cost-effectiveness but also their intrinsic activity and sufficient stability in highly oxidative electrochemical environments, making the use of them more realistic for commercial use. More importantly, they have various electronic valences and structures, and furthermore, there are a variety of ways one can synthesize the catalyst as well as one can easily control the shape of the catalyst to enhance the surface area and physical properties. Thus, the design and development of the non-precious transition metal-based electrocatalysts have been remarkably important in recent years.

Indeed, considerable progress has been accomplished during the past years in developing non-precious transition metal-based catalysts with high activity for ORR (metal-nitrogen-carbon (M-N-C), metal oxides, chalcogenides, nitrides, and oxynitrides), OER (metal oxides (perovskites and spinels), chalcogenides, phosphides, and layered metal (oxy)hydroxides).[20, 22, 25-39] In particular, high corrosion/oxidation resistive property of transition metal oxides in highly corrosive/oxidative environment within a high potential range of OER, which usually degrades the catalysts leading to poor electrochemical durability, has made them the most promising candidates as non-noble bifunctional electrocatalysts, However, they suffer from an intrinsically low electrical conductivity, which far reduces rates of charge transfers and eventually resulting in the loss of overall energy efficiency. Therefore, high surface conductive carbon materials (i.e., graphenes and carbon nanotubes) with heteroatom doping have been hybridized with the transition metal oxides to overcome the critical issue and further reduce carbon corrosion.[38-46] In addition, there could be synergy between the two different type of materials through a secure bonding environment of transition metal ions and organic ions such as carbon and nitrogen atoms.

In the meantime, metal-organic-frameworks (MOFs) have recently been highlighted as highly promising active and cost-effective candidates for electrocatalysts owing to their intrinsic properties of high porosity, three-dimensional structures, and morphological and compositional flexibility, possibly leading to enhanced active surface area and improved physical properties.[47-59] More importantly, MOFs are typically composed of transition metal cations bridged by functional organic ligands such as carbon and nitrogen atoms. Accordingly, MOFs could be an "all-in-one" solution to the above-mentioned hybrid approaches to enhance the overall efficiency of the bifunctional oxygen electrocatalysis. As a class of crystalline porous materials, MOFs are established with regularly arranged metal centers and organic ligands, leading to inherent

hierarchically porous architectures. Thanks to the unique characteristics of MOFs such as a large surface area with high porosity, and various possible compositions of transition metals and functional organic linkers, it is possible to obtain more accessible catalytic active sites and easily tunable morphology with electronic structures, both of which are crucial for development of bifunctionally active and durable electrocatalysts. Additionally, in terms of the electrochemical stability of MOFs (or MOF-based materials), they seldom suffer from the destruction of coordination bonds between the metal centers and organic ligands.

2. Thesis Objectives and Approach

Generally, an electrocatalysts with superb ORR activity is not able to possess great OER activity due to their opposite direction of oxygen redox reactions. This is directly related to the degree of adsorption/desorption of oxygen molecules, where a surface with strong bonding with oxygen gas would have good ORR activity and vice versa. Therefore, it has been challenging to develop bifunctionally active catalysts toward both ORR and OER. The conventional design of bifunctional electrocatalysts is to combine ORR active material such as high surface carbons and OER active metal oxides, as mentioned in the previous part. However, this is not able to be an ultimate solution for bifunctional catalysts since the hybrid catalysts are not a single material functioning both oxygen reactions, but rather two different materials in which each component is only functionally active to either ORR or OER. In this context, there should be two different synthetic processes and another procedure for the hybridization, decreasing manufacturing efficiency. Moreover, the existence of high surface carbon materials will hamper the long term use of the hybrid bifunctional catalysts due to carbon oxidation, limiting their use in practical energy technology such as Zn-air batteries.

Instead, as a new platform in designing energy materials, nanostructured electrocatalysts have received tremendous interest due to their unique properties such as hierarchically macro/mesoporous structure with an interconnected open framework, which is highly beneficial to enlarge specific surface area exposing more catalytically active sites and enhance charge transfer rates during the oxygen electrocatalysis. In addition to the morphological advantages, which are majorly responsible for improving mass activity, the intrinsic activity of the oxygen electrocatalysis can be regulated by elaborately tuning electronic structures via altering compositions and/or crystal structures.

Accordingly, the ultimate objective of this thesis is to research novel design strategies of bifunctionally active and durable electrocatalysts consisting of non-precious transition metals such as Co, Ni, and/or Fe through the nanostructuring technology. Notably, the design and engineering of robust three-dimensional frameworks with hierarchical porosity will be primarily carried out to obtain both more accessible active sites as well as improved mass transport of reactants, and robust interconnected frameworks for faster charge transfers and enhanced durability during the oxygen electrocatalytic reactions. This class of catalysts eventually can be an “all-in-one” solution for the development of efficient oxygen electrocatalysts and further commercially available rechargeable Zn-air batteries.

This thesis comprises the first important step of this long-term approach, and includes the design, development, and optimization of novel bifunctional oxygen electrocatalysts. The specific objectives of this study include:

i) Design and synthesize bifunctionally active and durable hierarchically porous architecture electrocatalysts derived from non-precious transition metals.

ii) Physicochemical and electrochemical characterizations of the designed and engineered materials to study the effects of the material design strategy onto the targeted electrocatalytic performance such as electrocatalytic activity and stability.

iii) Integration of theoretical prediction and experimental characterization to investigate criteria for improving electrocatalytic activity and durability, and explore a rational design strategy of efficient electrocatalysts.

2.1 Thesis outline

In Chapter 1, an introduction of background information and brief literature review of the work relevant to the electrically rechargeable Zn-air battery and bifunctional electrocatalyst development research have been provided. Chapter 2 provides an outline of the research objectives and how this thesis is organized. In Chapter 3, background information on various experimental procedures used throughout the project is provided, including physicochemical and electrochemical characterization techniques with in-depth details and task specifics provided within subsequent chapters.

Chapter 4 starts with an early development of a bifunctionally active and durable catalyst system, three-dimensionally ordered macro/mesoporous spinel cobalt oxide, which consists of hierarchically porous and robust interconnected frameworks. As an extension of this work, in Chapter 5, the deposition of metallic palladium (Pd) onto the surface of 3DOM Co_3O_4 is carried out to investigate and understand the effects of the second transition metal substituents on oxygen electrocatalytic activity and durability via a combination of experimental and computational analysis. Meanwhile, Chapter 6 discusses metal-organic-framework (MOF) based electrocatalyst, which is designed and synthesized to possess a robust framework with multi-

level porosity. A ternary nickel-cobalt-iron (Ni-Co-Fe) transition metal system has a critical contribution on generation of the hierarchical porosity and optimized composition of transition metal centers for efficient oxygen evolution reaction.

Finally, Chapter 7 provides conclusions of all the research conducted within the thesis, along with recommendations for future work to further push the rational design of highly efficient bifunctional electrocatalyst and improve performance and life-time of rechargeable Zn-air batteries at a practically viable level.

3. Characterization Techniques

This chapter introduces physicochemical and electrochemical characterization techniques employed for the completion of the thesis. Physicochemical characterizations are mainly used to reveal morphology, crystal structures, oxidation states, coordination environment, porosity and thermogravimetric properties of the nanomaterials studied in this study, while electrochemical characterizations are used to investigate the electrochemical performance of the developed electrocatalysts through both oxygen reduction and evolution reactions necessary for the electrically rechargeable Zn-air battery operation. For more details on synthesis procedures of specific nanomaterials and electrochemical performance evaluations, the reader is directed to the Experimental Methods section included in each of the following chapters.

3.1 Physicochemical Characterization Techniques

3.1.1 Scanning Electron Microscopy (SEM)

Scanning electron microscopy (SEM) is an important characterization technique that allows high-resolution investigation of morphological and topological information of materials in the micro and nanoscale. Unlike an optical microscope using visible light as the source of interaction in creating magnified images, SEM uses a focused beam of electrons by scanning the surface of samples to produce images with higher resolution. Through the interaction of the electrons with atoms in the surface, secondary and backscattered electrons are either emitted or reflected, followed by being captured by a detector above the specimen. Therefore, SEM has been utilized extensively to study the micro- or nano-structure of the developed catalyst materials in this research.

3.1.2 Transmission Electron Microscopy (TEM)

Transmission electron microscopy (TEM) is one of the essential material imaging techniques, leading to direct visualization of the sample's morphology. Similar to SEM, TEM also uses a beam consisting of electrons as the source to generate high-resolution images. However, unlike in SEM, which is able to detect reflected or backscattered electrons from the sample surface, electrons are passing through an ultrathin sample, which is called a transmission, and then reaches to a detector below the sample. TEM allows you to observe details as small as individual atoms with the highest possible resolution. As the electrons go through objects, it is able to get information about internal structures such as crystal orientation and planes, which is not possible in SEM. Therefore, TEM has been utilized extensively to study morphological and crystal structure with lattice information of the sample. Additionally, selected area electron diffraction (SAED) study carried out by TEM is able to review reciprocal lattice points from the Ewald Sphere, which is consistent with the results from X-ray diffraction technique handled in the following section. Moreover, high-resolution TEM (HR-TEM) allows the imaging of crystallographic structure of the sample at an atomic level. In comparison to the general TEM, the HR-TEM does not use absorption for generating images; instead, images are obtained from interference in the image plane, where the HRTEM image is an interference pattern between the forward-scattered and diffracted electron waves from the specimen.[60]

3.1.3 Energy Dispersive X-ray Spectroscopy (EDS)

Energy-dispersive X-ray spectroscopy (EDS) is an elemental analysis technique that can identify and quantify the chemical composition of a sample. The technique is commonly

incorporated into SEM and TEM devices to be conducted concurrently with common imaging techniques. EDS involves bombardment of solid surface of material with high energy electrons, leading to the emission of characteristic X-rays collected by a detector, which eventually results in material-specific EDS signal. The energy of the emitted X-rays is specific to each element possessing a unique atomic structure, which enables to identify specific elements in the sample being investigated. Typically, the EDS signal consists of a spectrum with the specific location of X-ray energy and the line intensities for each element in the sample, which is capable of qualitative and quantitative analyses, respectively. Furthermore, element distribution images or elemental "maps" can be produced by EDS, which is a highly interesting technique to investigate the distribution of localized elements on a selected area of a sample. The obtained elemental maps with variations in the emitted X-ray intensities are indicative of variations in the concentration of specific atomic contents at a particular location in the sample being investigated. This is particularly interesting for hybrid electrocatalysts consisting of both organic and inorganic materials to clearly identify the elements and the corresponding information of elemental distribution and concentration in the sample.

3.1.4 X-ray Diffraction (XRD)

X-ray diffraction (XRD) is a prevalent characterization technique in the field of materials science and engineering, which is capable of determination of crystal arrangements of a specimen. X-rays emitted from a source interact with the atoms in the sample being investigated, resulting in the production of a diffraction pattern. The diffracted X-rays at specific angles are collected by a detector, and the resultant diffraction pattern indicates a characteristic crystal

structure of the atoms within the specimen by a theory of Bragg's law. As shown in Equation 3-1 below,

$$n\lambda = 2d\sin\theta \quad \text{(Eq. 3-1)}$$

where d, θ, n, and λ in the Bragg's equation represent the spacing between diffracting planes, the incident angle, the order of the spectrum (any integer), and the wavelength of the X-rays, respectively. The obtained X-ray diffraction pattern can be used to identify the material upon comparison with diffraction pattern databases or theoretically calculated patterns by the crystal planes. In the present study, XRD is majorly used to identify the crystal structure and calculate the lattice spacing of the designed electrocatalysts. The specific instrumental condition of XRD used in the researches is followed: Cu Kα radiation (λ= 1.5405 Å) in the 2θ range of 10°–90°with 0.02° intervals, at a 0.02° min^{-1} scanning rate.

3.1.5 X-ray Photoelectron Spectroscopy (XPS)

X-ray photoelectron spectroscopy (XPS) is a surface-sensitive quantitative spectroscopic technique, also known as electron spectroscopy for chemical analysis (ESCA), allows investigation of surface characteristic information such as elemental composition, valence and electronic states of atoms existing within a material. Specifically, a beam of X-rays with constant energy (*hv*) is irradiated on a sample material, leading to the emission of electrons by the photoelectric effect, which indicates photoelectrons. The ejected photoelectrons and corresponding kinetic energy from the top 0 to 10 nm of the surface of the material being investigated are measured to obtain XPS spectra. Generally, XPS requires ultra-high vacuum conditions, where samples are analyzed at pressures of a few tens of millibar. By determining the

balance between the initial X-ray energy (*hν*) and the kinetic energy of the emitted photoelectrons, the binding energy of an electron can be measured. A specific electron binding energy is a characteristic of several factors, including the type of atom, the chemical state, and the elemental composition of the sample, acting as a fingerprint for identifying the material. Additionally, XPS allows the investigation of electronic (oxidation) states of an element making a prediction of empirical chemical formula possible. In this study, XPS is used to identify and quantify the elements in the developed electrocatalysts as well as their oxidation states.

3.1.6 Brunauer-Emmett-Teller (BET) Surface Analysis

Brunauer-Emmett-Teller (BET) analysis is a useful technique for the measurement of specific surface area and porous nature of materials, where the theory of BET is aimed to explain the physical adsorption/desorption phenomena of gas molecules onto a solid surface. Inert gas such as nitrogen (N_2), argon (Ar), and carbon dioxide (CO_2) are usually utilized as adsorbates to avoid any chemical reactions with the material surface being analyzed. The BET theory applies to systems of multilayer adsorption, which is an extension of Langmuir theory for monolayer molecular adsorption. The following representative hypotheses for BET theory is as followed: i) physical adsorption of gas molecules on a solid in layers infinitely at the saturation pressure, and ii) only interaction of the gas molecules with the adjacent layers. In the specific research field of the development of hierarchically porous electrocatalysts, this surface analysis tool is highly useful to investigate their high specific surface area and large porosity due to the fact that electrocatalysis studied here including oxygen reduction and oxygen evolution reactions are all surface reactions. In terms of data analysis, as the shape of adsorption/desorption isotherm is classified into several types depending on the porous nature of materials, it is possible to

determine the surface and porous nature of materials. Particularly, enlarging the specific surface area and porosity of electrocatalysts through design and engineering of materials is one of the primary goals of this research since more electrocatalytic active sites can be exposed to reactants such as gaseous oxygen (O_2) from the outside and hydroxide ions (OH^-) in electrolyte for ORR and OER, respectively. Therefore, designing and engineering nanostructured materials accompanying the hierarchical architecture with large specific surface and porosity area is significantly essential for the enhancement of both activity and durability of electrocatalysts.

3.1.7 Thermogravimetric Analysis (TGA)

Thermogravimetric analysis (TGA) is a technique of thermal analysis in which the weight change of the sample is measured over time as a function of temperature. For the purpose of this study, TGA is used to estimate the weight of metals (oxides) after removing any carbonaceous materials at high temperatures in an air atmosphere to determine the ratio between metals and carbons existing within the developed metal/carbon hybrid catalyst materials.

3.2 Half-Cell Electrochemical Evaluation Techniques

Various electrochemical characterization techniques using the half-cell system are employed in this study to investigate electrochemical properties and electrocatalytic performances such as activities and durability of the developed catalyst materials. This section provides background information with related theory regarding these techniques. It should be noted that ideal experimental parameters for electrochemical testing depend on the catalyst under investigation, which specifically involves catalyst loading, the concentration of ionomer

(polymeric binder), and type of solvents for catalyst ink preparation. Therefore readers are guided to the Experimental Methods section of the following chapters within this thesis for information regarding the preparation and testing parameters used for different catalysts.

3.2.1 Cyclic Voltammetry (CV)

Cyclic voltammetry (CV) is a potentiodynamic electrochemical measurement technique employed to investigate reduction and oxidation characteristics of the developed catalysts. During the CV process, a potential of the working electrode is linearly swept forward and backward at a certain scan rate within a desired potential range. By sweeping the potential, a current is measured, showing a plot of the current versus potential leading to a cyclic voltammogram, which further indicates a unique redox property of the analyzed catalyst. This enables identification of redox reactions in an electrocatalyst and degree of reversibility. Therefore, in this thesis, CV is utilized to confirm oxygen reduction reaction (ORR) and oxygen evolution reaction (OER) performances of the developed catalysts in oxygen-saturated and nitrogen-saturated electrolyte, respectively. In addition, CV is carried out in nitrogen-saturated inert electrolyte for the sake of verification of possible existence of undesired reactions where they should not be applied to the measured ORR cyclic voltammograms.

3.2.2 Rotating Disc Electrode (RDE)

The half-cell electrochemical testing via rotating disk electrode (RDE) measurement is a fundamental technique widely utilized not only for electrochemical analysis of redox reaction mechanisms but also for rapid evaluations of the developed electrocatalysts.[61] Typically, RDE is composed of a glassy carbon disk electrode embedded in an insulating Teflon outer layer, where

the developed catalysts are solely coated on the smooth surface of glassy carbon. Rotating the electrode generates a flow of electrolyte, triggered by convection, by allowing mass transport of active species such as hydroxide ions and gaseous oxygen saturated in electrolyte.

A series of experimental data is obtained *via* a variety of rotating speeds of the RDE, where they are required for the sake of analyzing electrochemical catalytic reactions at a determined speed and further investigating correlations among the data obtained at the different rotation speeds. In this study, a rotating disc electrode (RDE) half-cell equipment was employed to investigate both oxygen reduction reaction (ORR) and oxygen evolution reaction (OER) catalytic activity of the prepared materials.

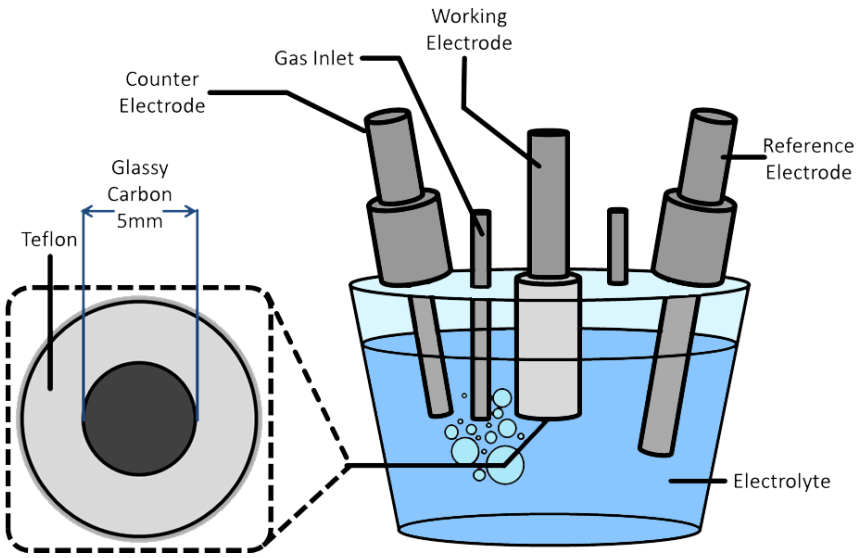

Figure 3-1. Conventional three-electrode half-cell system

As depicted in **Figure 3-1**, a conventional three-electrode half-cell system consisting of a working electrode, a reference electrode, and a counter (auxiliary) electrode was used. Electrocatalyst-coated glassy carbon disk electrode and a platinum wire were used as working and counter electrodes, respectively, while a saturated calomel electrode (SCE) or reversible hydrogen electrode (RHE) were employed as the reference electrode. 0.1 M KOH solution was

used as an aqueous electrolyte. To obtain an oxygen or nitrogen saturated electrolyte, the oxygen or nitrogen gas was purged into the KOH solution for 30 minutes before the evaluations while continuing bubbling during the tests. In order to prepare a catalyst coated working electrode, a glassy carbon electrode (Diameter: 5mm & surface area: 0.196 cm^2) was employed. It was first polished by using alumina powder (size: 0.3 μm & 0.05 μm), and then the electrode was directly ultrasonicated in deionized and distilled (DDI) water for a short time then dried with nitrogen gas stream.

Generally, the preparation of sample inks was done by the following steps. 4 mg of the catalyst was put into 1 mL of ethanol pre-treated by Nafion solution (0.05 wt. %), and the mixture was ultrasonicated for longer than 30 minutes until obtaining a homogenously mixed catalyst ink. 20 μL of the as-prepared dispersion was dropped onto the circle-shaped glassy carbon surface, followed by dry under ambient conditions, leading to 0.4 mg cm^{-2} of catalyst loading.[62-65] As mentioned above, the ideal experimental parameters for electrochemical testing rely on the properties of developed electrocatalysts, and thus the parameters for catalyst ink preparation could vary in different projects. Meanwhile, electrocatalytic ORR activity was recorded from 0.1 to -1.0 V vs. SCE at a scan rate of 10 mV s^{-1} in the oxygen-saturated electrolyte under a series of rotating electrode speeds (400, 900, 1600, and 2500 rpm). The ORR polarization curves were corrected by subtracting background currents by the same test procedures obtained with nitrogen saturated electrolyte in order to remove capacitive current contributions. The electrochemical performance of the OER was measured from 0 to 1 V vs. SCE at a scan rate of 10 mV s^{-1} (50 mV s^{-1} for the OER durability test, which is accelerated degradation testing (ADT)) with nitrogen-saturated electrolyte with 900 or 1600 rpm in order to sufficiently remove oxygen bubbles generated on the electrode surface during the OER test.

Figure 3-2 illustrates typical ORR and OER polarization curves, where there are some important values such as half-wave potential ($E_{1/2}$), OER potential at 10 mA cm^{-2} (E_{10}), and onset potential (E_{onset}). Firstly, the half-wave potential ($E_{1/2}$) is a primary activity measurement tool, which is the potential at which the current density reaches exactly half that of the mass transport limited current. Half-wave potential thereby provides an indication of intrinsic ORR activity, along with mass transport and catalyst utilization in the electrode. Next, OER potential at 10 mA cm^{-2} (E_{10}) is an important indicator for evaluating OER activity, where E_{10} is the potential at which the OER current density reaches 10 mA cm^{-2} (j_{10}). Additionally, onset potential (E_{onset}) commonly indicates the potential at which the reaction current deviates from the baseline at which no reaction current occurs (zero current). Since experimental determination of the onset potential could be quite ambiguous, a common approach is either to measure a potential at a small current density such as 1 mA cm^{-2}, which can vary in accordance with the current scale determined by pH of the electrolyte, or to obtain the intersection of the tangents between the baseline and the rising current in the voltammogram. The overall overpotential for both ORR and OER is measured by frequently adopting the potential difference between the half-wave potential ($E_{1/2}$) from ORR and the OER potential at 10 mA cm^{-2} (E_{10}) from OER, where the smaller the overpotential is obtained, the better electrocatalytic activity is achieved.

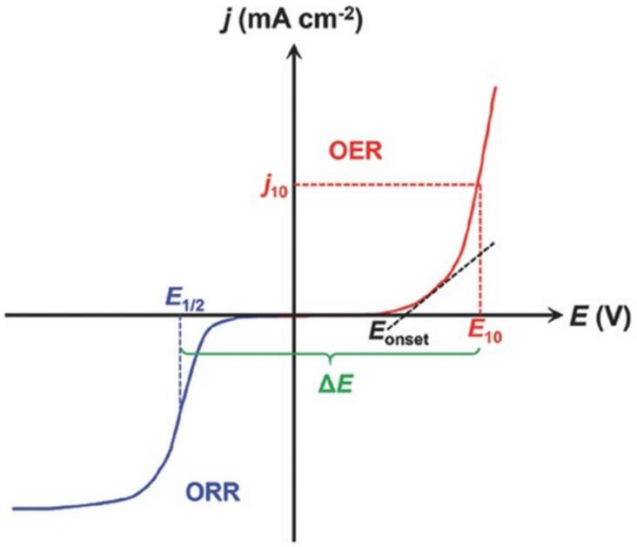

Figure 3-2. ORR and OER polarization curves with half-wave potential ($E_{1/2}$), OER potential at 10 mA cm^{-2} (E_{10}), and onset potential (E_{onset}). Reproduced from reference 32, with permission from the Wiley-VCH.[66]

From the ORR polarization curves obtained at the different rotation speeds, it is possible to study the reaction kinetics and mechanisms of the developed catalyst via a Koutecky-Levich (K-L) equation which is as following:[67]

$$\frac{1}{j} = \frac{1}{j_K} + \frac{1}{j_{Lev}} = \frac{1}{j_K} + \frac{1}{B\omega^{0.5}}$$

$$j_K = nFkC_{O_2} \textit{ (kinetic current)}$$

$$B = 0.62nFD_{O_2}^{2/3}C_{O_2}v^{-1/6} \textit{ (Mass transport limiting current constant)}$$

In the above equations, the limiting current (j) is related to kinetic current (j_K) and Levich current (j_{Lev}), where j is the observed current. n is the number of electrons transferred per O_2 molecule; F is the Faraday constant (96,485 C mol^{-1}); k is heterogeneous electron transfer rate constant; C_{O_2} is the saturated concentration of O_2 in the electrolyte (1.1×10^{-6} mol cm^{-3}); D_{O_2} is the diffusion coefficient of O_2 (1.9×10^{-5} cm^2 s^{-1}); v is the kinematic viscosity of the solution

(0.01 cm^2 s^{-1}); and $\boldsymbol{\omega}$ is the rotation rate of RDE. The linear fitting of K-L plots between $\boldsymbol{j^{-1}}$ vs. $\boldsymbol{\omega^{-0.5}}$ is based on the Koutecky-Levich equation.[67]

The K-L plots are mainly used to determine the number of electrons transferred at the surface of the catalyst during ORR.[68] As presented in **Figure 3-3**, by the linear fitting of the K-L plots, the transferred electrons during ORR can be calculated and an average numbers of the electrons also can be obtained at different working electrode potentials. Furthermore, the Y-intercept of the K-L plot represents the kinetic current ($\boldsymbol{j_K}$) and the slope of the K-L plot directly leads to the number of electrons transferred. The number of electrons transferred has an ideal number, which is four, where the four electrons transferred during ORR means that ORR is ideally occurring, and only hydroxyl ions are made during the catalytic reaction without the creation of peroxide species. Typically, the number of electrons transferred is much less than the four when using non-precious catalysts.

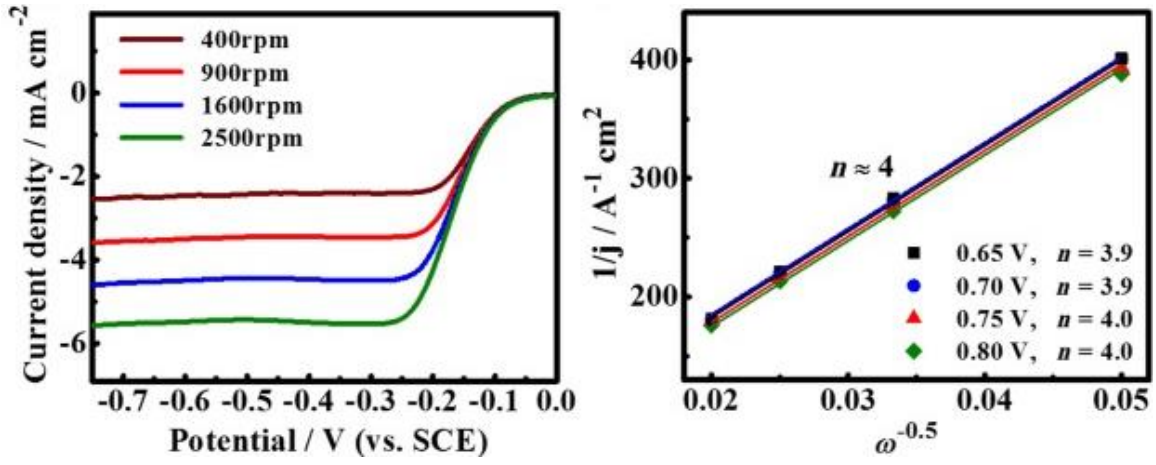

Figure 3-3. RDE measurements of Co_3O_4 NC/N-CNT hybrid catalyst in O_2-saturated 0.1 M KOH electrolyte at different rotation rates with the corresponding Koutecky–Levich plot at various potentials. Reproduced from reference 35, with permission from the Wiley-VCH.[69]

3.2.3 Accelerated Degradation Testing (ADT)

Accelerated degradation testing (ADT) is conducted to investigate the durability of the catalyst in a shortened period of time. This technique consists of repeating CV cycles up to 2000 within a potential range involving ORR and/or OER in an N_2-saturated electrolyte at a certain temperature. The electrochemical stability of the catalyst being analyzed is obtained by comparing the initial electrocatalytic activities of ORR and/or OER with the final activity after ADT, which results in a determination of the degree of performance degradation.[62, 64, 65, 70, 71]

3.2.4 Chronopotentiometry (CP)

Chronopotentiometry (CP) is one of the galvanostatic methods in which the rate of change of potential at an electrode is measured at constant current. Typically, the galvanostatic method uses the three-electrode system, where a current is applied between the working and counter electrodes, and the potential of the working electrode, measured associated with the reference electrode, is monitored. The criterion for the experiments is that a redox reaction during which electron or charge transfers must occur at the surface of the working electrode to support the applied current. In voltammetry, when the current flowing through the working electrode is fixed at a constant value, the potential of the working electrode varies with time. When a controlled current is passed through a cell between the working and counter electrodes, initially, the potential of the working electrode will change rapidly as charge builds up at the electrode-electrolyte interface until potential is reached at which the electrolysis of an electrochemically active component of the electrolyte begins. In the cases of OER and HER, when the current is applied to the cell at a constant value, the certain potential is measured on the

electrode surface (working electrode) along with the amount of the applied current based on the electrocatalytic reactions as a function of time (*v*-*t*). One advantage of the constant current techniques is that the ohmic drop (resistance), which is typically generated due to solution resistance, is also constant, since it is equal to the product of the current and the solution resistance. Therefore, the ohmic distortion can be simply corrected by a constant potential offset to investigate more accurate values. On the other hand, during the potentiostatic experiments (e.g., cyclic voltammetry), the current, and hence the ohmic drop, varies with potential.

3.3 Rechargeable Zn-air Battery Performance Evaluation Techniques

Zn-air battery (ZAB) is one of the most mature metal-air battery systems and used as the major energy conversion and storage application for the evaluation of electrocatalysts performances in this thesis. There are important experimental parameters such as open-circuit voltage (OCV), operating voltage, energy efficiency, energy density, power density, and cycleability that should be investigated to evaluate the performance of the developed electrocatalysts. Typically, ZAB consists of not only the air electrode and zinc plate as a cathode and an anode, respectively, but also electrolyte and separator. The experimental parameters such as air electrode loading applied current density, and cycling time for rechargeable ZAB testing could vary in different projects depending on their optimal condition.

3.3.1 Galvanodynamic Discharge and Charge

The galvanodynamic technique allows investigation of charge and discharge behaviors of the catalyst being evaluated in Zn-air battery. This technique is generally carried out by applying gradually increasing negative (for battery discharge) and positive (for battery charge) currents from 0 A up to a desired value with a set current rate (A/s), and monitoring the change in the battery operation voltage. As shown in **Figure 3-4**, the operation voltage responses are plotted as a function of the applied current, leading to discharge and charge polarization curves. The voltage gap between the polarization curves for discharge or charge and the OCV measured initially at zero current indicates a total voltage losses (i.e., discharge or charge overpotential, respectively). The overpotentials are majorly associated with the oxygen electrocatalytic reactions such as ORR and OER occurring at the catalyst-coated air electrode, which is due to the substantial activation energy barrier for electron transfer from the electrode to electrolyte during the oxygen redox reactions. In addition to obtaining overpotentials from the galvanodynamic polarization curves, a power density of the Zn–air battery can be obtained by plotting the applied current density with the value acquired by multiplying the discharge voltage by the applied current density. When the applied current density is sufficiently high (the value usually depends on the catalyst being used and the current density), we could observe a peak power density at a specific current density. The polarization curves obtained from this technique are used to identify overpotentials associated with the electrocatalytic oxygen redox reactions and resistances primarily related to activation and ohmic polarization phenomena occurring during the Zn-air battery operation.

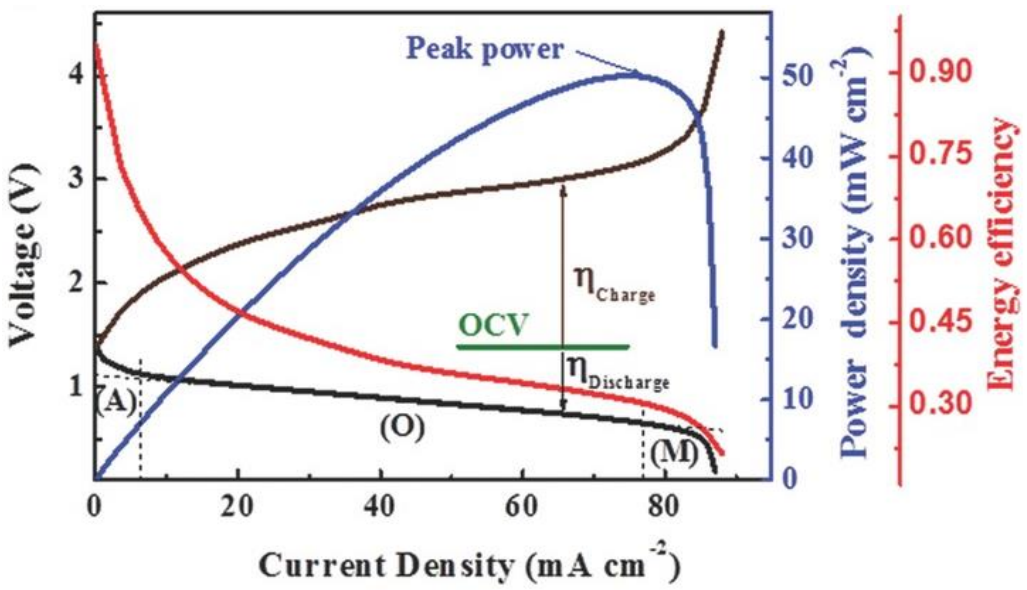

Figure 3-4. Typical discharge and charge polarization curves for the rechargeable Zn-air battery, as well as the power density and energy efficiency. Reproduced from reference 11, with permission from John Wiley and Sons (2016).[11]

3.3.2 Galvanostatic Cycling

Galvanostatic cycling is an accelerated battery testing technique to investigate the electrochemical durability of catalyst material included Zn-air battery. This technique is carried out by applying a fixed negative (for discharge) and positive current (for charge) and measuring the operation voltage profile of the battery. A single cycle consists of charge and discharge region induced by the applied current of the same magnitude but opposite polarity (i.e., negative and positive currents) for a fixed amount of time for each side. Then, the galvanostatic battery cycling test is done by repeating the single cycle for the desired number of cycles and recording battery voltage profile change over a specified time length of battery cycling. The time interval for each cycle can be adjusted to simulate either pulse cycling (i.e., 10 minutes per cycle) or extended cycling (i.e., 4 hours per cycle), as demonstrated in **Figure 3-5**. The pulse cycling technique is an excellent diagnostic tool for evaluating the battery's rechargeability by switching

the polarity in short intervals and extended cycling measures more practical cycling capabilities of the battery. Since the two different testing methods provide uniquely useful information, it is suggested to perform both types of techniques for a more accurate investigation of Zn-air batteries. As a result, the observed degree of voltage retention over a total number of cycles (total length of time) is directly indicative of the durability of the catalyst being studied.

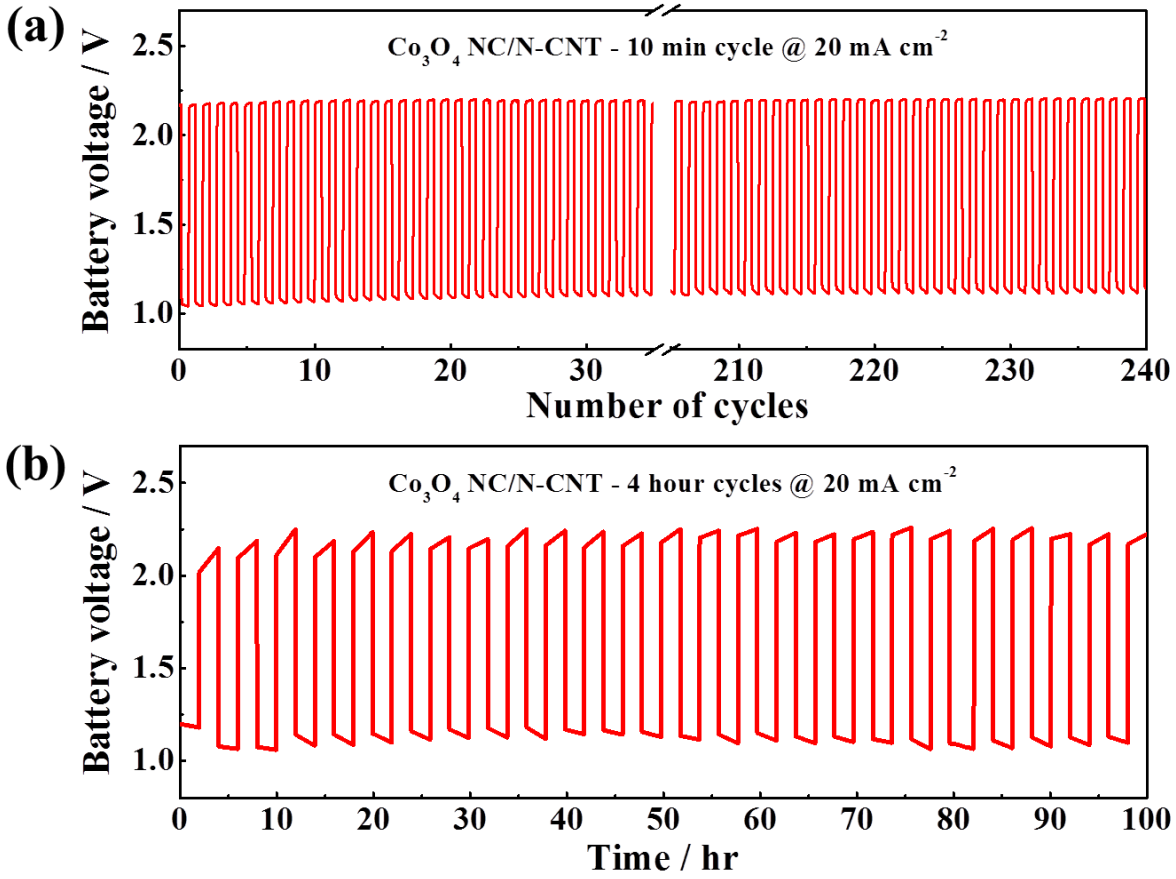

Figure 3-5. Typical galvanostatic cycling of rechargeable Zn-air battery. (a) pulse cycling with 10 minutes per cycle (5 min discharge & 5 min charge) and (b) extended cycling with 4 hours per cycle. Reproduced from reference 35, with permission from John Wiley and Sons (2014).[69]

4. Sacrificial Polymer Template derived Hierarchically Porous Co_3O_4 as Bifunctional Oxygen Electrocatalyst for Rechargeable Zn-air Batteries

This chapter is reprinted in adapted form from the below article[62] with permission from Wiley.

Park, M. G., D. U. Lee, M. H. Seo, Z. P. Cano, Z. Chen, "3D Ordered Mesoporous Bifunctional Oxygen Catalyst for Electrically Rechargeable Zn-air Batteries", *Small*, 12 (2016) 2707-2714.

4.1 Introduction and Motivation

With increasing costs of natural fuels and environmental issues associated with their use, novel battery technologies such as metal-air batteries are attracting much attention due to their extremely high energy density compared to currently most widely used lithium-ion batteries.[72-74] Since metal-air batteries utilize oxygen in atmospheric air as cathodic fuel, no onboard fuel reservoir is required, making them highly viable for electric vehicle (EV) applications. Currently, however, a few technical challenges hamper widespread commercialization of metal-air batteries such as slow kinetics of oxygen reduction reaction (ORR) and oxygen evolution reaction (OER), which are the electrochemical reactions that govern discharge and charge processes of the battery. Relatively large overpotentials associated with these reactions lead to reduced energy efficiencies, which motivates research and development of active catalysts that can enhance the reaction kinetics. Currently, metal-air battery investigations are much focused on the development of bifunctionally active and durable catalysts to enhance both ORR and OER using inexpensive, Earth-abundant, and environmentally friendly materials. As a family of non-precious electrocatalysts, transition metal-based catalysts have been rigorously investigated and utilized as the bifunctional catalysts for metal-air batteries.[5, 63, 64, 75-82] In particular, transition

metal oxides have attracted much attention for bifunctional application due to their unusual activity and stability since they possess multiple valences and abundant crystallographic structures resulting in rich redox electrochemistry and materials chemistry, providing a vast opportunity.[83-89] However, more rigorous research effort is required to further improve the catalytic activity and stability potentially by altering chemical compositions, morphologies, or crystal structures. Among various non-precious metal oxide catalysts, spinel cobalt oxides (Co_3O_4) having different morphologies such as nano-particles, nano-wires, and nano-flakes are widely utilized as efficient bifunctional electrocatalysts, demonstrating enhanced catalytic activity and electrochemical stability.[6, 65, 77, 90, 91] Among previous research of spinel cobalt oxides as bifunctional catalysts in our group, Co_3O_4 nanodisks and nanowires have been prepared with enhanced active surface area accompanied by improved ORR and OER activities.[92, 93] Especially, the Co_3O_4 nanowires directly grown on stainless steel mesh have provided a promising possibility of a practically available rechargeable Zn-air battery by demonstrating long durability. However, their performance until now is still insufficient to be commercially mass-produced for widespread usage. To further advance the performance of non-precious metal catalysts, it is necessary to develop 3-dimensional morphological structures, possessing highly porous and stable architectures that can generate excellent catalytic activity and stability.

Herein, we introduce three-dimensionally ordered mesoporous cobalt oxide (3DOM Co_3O_4) with hierarchical porosity and structural robustness, which is non-precious bifunctional catalyst active towards both ORR and OER as a promising air electrode material for electrically rechargeable Zn-air batteries. This innovative electrocatalyst with advanced morphology is synthesized by a simple template-derived process. Polystyrene bead templates are prepared and

soaked in cobalt precursor solution where the precursor permeates the voids of the beads followed by heat treatment and dissolution process to crystallize cobalt oxide frames and remove polystyrenes, respectively. 3DOM Co_3O_4 is a highly promising candidate for non-precious bifunctional catalysts due to its significantly extended active surface area and highly stable structure, which are derived from three-dimensionally and hierarchically ordered pores and considerably robust metal oxide architecture, respectively. Utilizing the advanced electrocatalyst, highly bifunctional activity and durability are demonstrated by three-electrode half-cell testing and electrically rechargeable Zn-air battery cycling as fundamental and practical electrochemical evaluation techniques, respectively.

4.2 Experimental Methods

4.2.1 Preparation of 3DOM Co_3O_4 and Bulk Co_3O_4

First, polystyrene particles were prepared by simple polymerization using styrene monomer, potassium persulfate, and polyvinylpyrrolidone (PVP) bought from Sigma-Aldrich Canada. In a round flask, 2.5 mg of PVP was dissolved in 200 mL of distilled de-ionized water and heated up to 70 ^oC. Once the temperature reached 70 ^oC, the polystyrene monomer was added, then the potassium persulfate-dissolved solution was put into the mixture with a prolonged rate. The polymerization was carried out for 24 hr under stirring, and condenser was used to stop evaporation of the mixture solution. Additionally, Nitrogen gas was continuously purged to make the inside a no-oxygen environment. After the polymerization, the prepared mixture solution was centrifuged at low speed for more than 12 hr. Then, a highly layered polystyrene chunk was obtained after the drying process at 60 ^oC. Meanwhile, cobalt precursor

solution was prepared by aqueous solvents such as ethanol or ethylene glycol, and cobalt nitrate hexahydrate. Afterward, polystyrene fragments were soaked in the precursor solution for 1 day, followed by drying at ambient temperature. The cobalt-soaked polystyrene fragments were calcined at 300 ^{o}C for 3 hr so as to melt polymer as well as partially solidify the cobalt precursor. Then, in order to utterly remove the polymeric material, toluene or a mixture of hexane and acetone were utilized. After the dissolving process, rest solvent was separated by centrifugation, and the process was repeated a few times. The as-obtained powder was dried at 100 ^{o}C and then followed by calcination at 400 ^{o}C for 3 hr. This process allows cobalt precursors to be entirely transformed into cobalt oxides with high crystallinity. The preparation of bulk Co_3O_4, which was used as a reference catalyst, is as followed: Firstly, $Co(NO_3)_2$•$6H_2O$ (1 mM) is dissolved in ultrapure water (35 mL) and stirred for 30 min. 6 M KOH solution was added until the pH of the solution reached 13. After, the prepared solution was transferred to Teflon liner (50 mL) and put into stainless steel autoclave, followed by heat treatment at 220 ^{o}C for 48 h. After cooled down to room temperature, the solution was washed and filtered by ultrapure water and reagent ethanol and dried at 60 ^{o}C overnight. As a final procedure, the dried powder was annealed at 400 ^{o}C for 3 h to get spinel crystal structured bulk cobalt oxide (Co_3O_4).

4.2.2 Half-cell Electrochemical Measurements

A rotating disc electrode (RDE) half-cell equipment was employed to investigate both oxygen reduction reaction (ORR) and oxygen evolution reaction (OER) catalytic activity of the prepared materials. The conventional three-electrode system consists of a working electrode, counter electrode, and reference electrode was used. Glassy carbon electrode, platinum wire, and saturated calomel electrode (SCE) were utilized as the working electrode, counter electrode, and

reference electrode, respectively. For the preparation of catalyst ink, 4 mg of the catalyst was mixed with 1 ml of isopropanol pre-treated by Nafion solution (0.3 wt. %), and the mixture was ultra-sonicated for 1 h to obtain a homogenous ink. 20 μL of the as-prepared ink was dropped onto the glassy carbon and dried under ambient conditions (catalyst loading: 0.4 mg cm^{-2}). Both oxygen-saturated and nitrogen-saturated 0.1 M KOH solution was exploited as an aqueous alkaline electrolyte in order for the ORR and OER experiments, respectively. For saturation environments, the oxygen or nitrogen gas was purged into the KOH solution for 30 minutes. Electrochemical properties of the catalysts were studied by linear sweep voltammetry (LSV) for ORR and cyclic voltammetry (CV) for OER, where CHI Electrochemical Station (Model 760D) and rotation speed controller (Pine Instrument Co., AFCBP-1) were used to evaluate the performances. ORR test was carried out from 0 to -1.0 V vs. SCE at a scan rate of 10 mV s^{-1} with oxygen saturated electrolyte at a series of rotating electrode speeds (400, 900, 1600 and 2500 rpm). The ORR polarization curves were corrected by subtracting background currents, which are obtained via the same test procedures in nitrogen saturated electrolyte, so as to exclude capacitive contributions during the ORR tests. The electrochemical performance towards OER was gauged within a potential range from 0 to 1 V vs. SCE at a scan rate of 10 mV s^{-1} (50 mV s^{-1} for the OER cycling as a durability test) with nitrogen saturated electrolyte at 900 rpm of rotation speed, which is for removing oxygen bubbles generated onto the glassy carbon surface during the OER test. Meanwhile, the precious metal-based bifunctional active material consisting of both platinum carbon (Pt/C, 28.8 wt. % Pt) and iridium carbon (Ir/C, 20 wt. % Ir), as one of the best ORR and the best OER catalyst, respectively, were employed as the reference material in order to exhibit the effectiveness and practicality of highly active and stable 3DOM Co_3O_4

electrocatalyst. The internal resistance of the working electrode was automatically applied to the experimental data.

4.2.3 Rechargeable Zn-Air Battery Performance Evaluation

Rechargeable Zn-air battery prototype consisting of zinc plate (OnlineMetals, Zinc Sheet EN 988), polypropylene separator (Celgard 5550), catalyst-coated gas diffusion electrode (GDE), and 6.0 M KOH with 0.2 M zinc acetate solution was utilized for investigating practical use of the catalyst. As the name of Zn-air battery says, the zinc plate is utilized as an anode side, and the reason of using separator is mainly to prevent dendritic growth where it has been generated from the oxidation of zinc sources (from zinc metals to solid zinc oxides) and consequently may take place to short-circuit failure. The catalyst-coated GDE is used as a cathode where both discharge and charge processes occur repeatedly. The GDE was prepared by a single-layering method, where all components, including the gas diffusion layer and catalyst layer, were mixed and compressed together onto nickel foam. The components, including developed catalyst, multi-walled carbon nanotube, nickel powder, and poly(tetrafluoroethylene) (PTFE) (a weight ratio of 1 : 0.5 : 0.5 : 7.5 : 0.5, respectively), were put into a mixture of distilled water and 2-propanol and then ultra-sonicated for 2 hr to achieve a uniformly dispersed solution. After being dried by nitrogen gas stream at ambient temperature, the prepared slurry was obtained and put onto the nickel foam covering one side. After the process, the coated-nickel foam was compressed by rolling-press. The gas diffusion electrode (GDE) in this study was prepared by using nickel powder instead of carbon. The interparticle voids that formed between the nickel particle acted as the gas diffusion layer. This type of nickel powder-based GDL has been proven to be effective in previously reported articles, mainly for rechargeable metal-air battery applications, where conventional carbon-based GDLs tend to undergo carbon corrosion due to high potentials

incurred during battery charging. The addition of a small amount of carbon nanotubes (5 wt. %) acted as the electrically conductive linkers to improve charge transfer during the electrocatalytic reaction as well as material utilization.[76, 94] The nickel foam was used not only as a support for the slurry but also as a current collector at the other bare side. Galvanodynamic charge and discharge experiments were carried out with a multichannel potentiostat (Princeton Applied Research, VersaSTAT MC). With a wide range of current change (current density: 0 ~ 70 mA cm^{-2}), discharge and charge polarization curves were obtained (V vs. i). Zn-air battery single cell discharge and charge cycling tests were operated by a cycling tester (BTSDA). The cycling was performed with 2 hr cycles (1 hr discharge and 1 hr charge) and a current density of 10 mA cm^{-2}. The assembled battery was operated in ambient conditions with purging pure oxygen gas.

4.3 Results and Discussion

Figure 4-1 shows a simple schematic process of 3DOM Co_3O_4 synthesis, transmission electron microscopy (TEM) images and a high-resolution TEM (HRTEM) image with selected area electron diffraction (SAED) pattern as well as scanning transmission electron microscopy (STEM) elemental mapping of 3DOM Co_3O_4. The TEM images reveal highly ordered and uniform hierarchical framework structure with regular porosity (average pore diameter of c.a. 150 nm) (**Figure 4-1b and 4-1c**) created by using PS beads as a useful template. The 3DOM structure is thus a negative of the PS template, where highly concentrated Co_3O_4 arranged in a hexagonal pattern is due to the collection of the material in the voids of neighboring beads. **Figure 4-1d** shows that 3DOM Co_3O_4 is highly crystalline evident by apparent lattice fringes observed and the obtained SAED pattern (**Figure 4-1d inset**). Accordingly, the skeletal architecture of 3DOM Co_3O_4 is likely to be robust for enhanced electrochemical durability.

Furthermore, the composition and distribution of elements of 3DOM Co_3O_4 is revealed by STEM elemental mapping (**Figure 4-1e, 4-1f, and 4-1g**), where virtually identical cobalt and oxygen maps are observed in green and yellow, respectively. Additionally, the morphology of 3DOM Co_3O_4 is also verified by scanning electron microscopy (SEM), where both high and low magnification images reveal highly ordered "honeycomb-like" 3D hierarchically framework consistent with the result of TEM analysis with each cluster having micro-scale dimensions (**Figure 4-2**). The micro-sized pores facilitate diffusion of oxygen into and out of the catalyst structure much more effectively during ORR and OER, respectively, which is attributed to the relatively larger sizes of voids having lowered oxygen diffusion resistances compared to those of nano-sized pores. The oxygen readily being transported in and out of the structure could then lead to reduced overpotential for the onsets of ORR and OER, improving the activity of the catalyst.

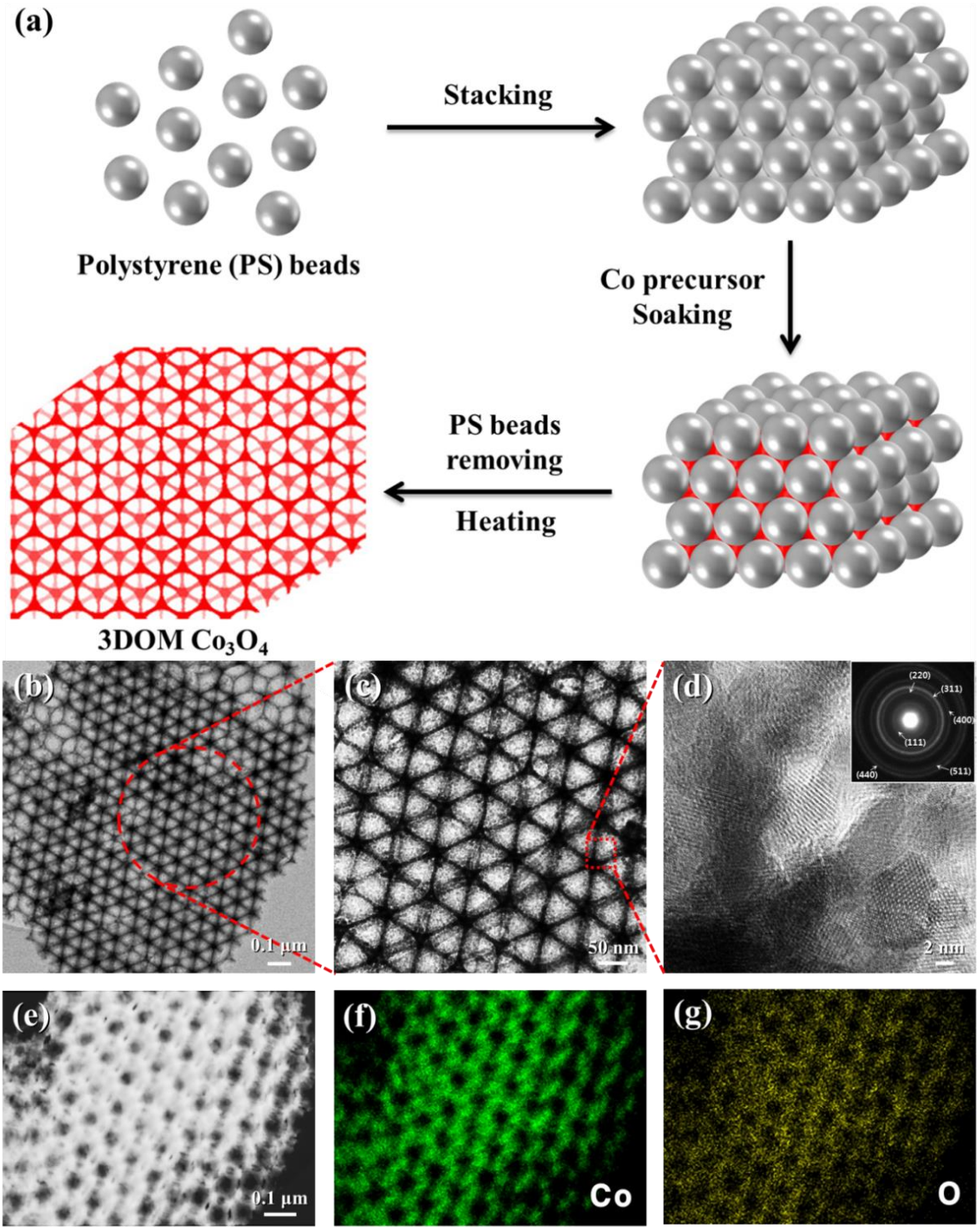

Figure 4-1. a) schematic image of 3DOM Co_3O_4 synthesis, b-d) Bright-field and high-resolution TEM (HRTEM) with selected area electron diffraction (SAED) pattern (inset), and e-g) Dark-field scanning transmission electron microscopy (STEM) with elemental mapping of cobalt and oxygen of three-dimensionally framed cobalt oxide (3DOM Co_3O_4)

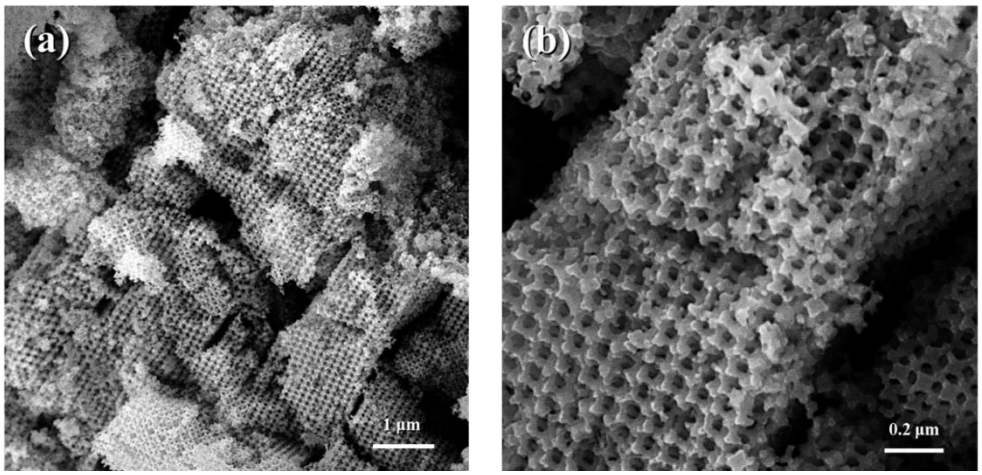

Figure 4-2. SEM image of 3DOM Co_3O_4 in (a) low, and (b) high magnifications

Next, X-ray diffraction (XRD) have been carried out to confirm the crystal structure of 3DOM Co_3O_4 (**Figure 4-3a**) and compare to that of bulk Co_3O_4 prepared as a control, where the bulk Co_3O_4 has been synthesized by a simple hydrothermal reaction followed by annealing at the same temperature applied to the preparation of 3DOM Co_3O_4. The XRD patterns of both 3DOM and bulk Co_3O_4 are indicative of cubic spinel crystal structure consistent with that of typical spinel cobalt oxide (space group: *Fd3m* (227), JCPDS no. 42-1467).[95, 96] The crystal lattices of 3DOM Co_3O_4 previously confirmed by the obtained SAED pattern (**Figure 4-1d inset**) match the peaks of the XRD pattern. Despite having the same crystal structure, the morphology of 3DOM and bulk Co_3O_4 is different, as shown by TEM images in **Figure 4-3c and 4-3d**, respectively, where the innovative morphology of 3DOM Co_3O_4 is the most crucial requisite determining improved electrochemical performance. Overall, 3DOM Co_3O_4 exhibits a highly regular three-dimensionally ordered mesoporous structure, whereas bulk Co_3O_4 is observed to consist of highly compact crystals of Co_3O_4 particles without any signs of pore formation.

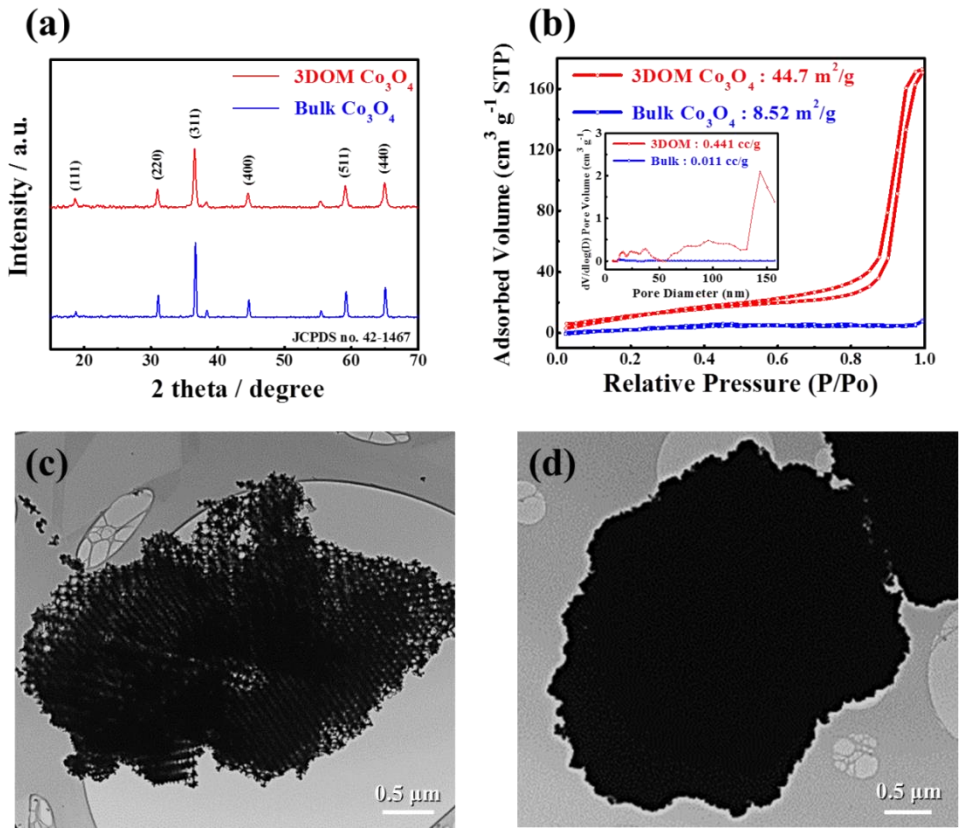

Figure 4-3. a) XRD patterns of 3DOM Co_3O_4(top red) and Bulk Co_3O_4 (bottom blue) (b) Nitrogen adsorption-desorption isotherms and pore size distribution of 3DOM Co_3O_4 (c and d) TEM images of 3DOM Co_3O_4(left) and Bulk Co_3O_4(right). Each scale bar is 0.5 μm.

As observed in SEM and TEM images, hierarchically ordered and interconnected inorganic frames result in a honeycomb-like mesoporous 3DOM Co_3O_4 structure, where the three-dimensionally open structure gives rise to a high surface area exposing more active sites for bifunctional catalysis. This is verified by the N_2 adsorption-desorption isotherms (**Figure 4-3b**), where 3DOM Co_3O_4 results in a type IV isotherm with a type II contribution having a type H3 hysteresis loop in the higher relative pressure (P/Po) range of 0.6-1.0, which are characteristics of a mesoporous material.[97-100] In terms of the specific surface area, the BET measurement has resulted in 44.7 m^2g^{-1} for 3DOM Co_3O_4, which was about five times greater than that of the bulk (8.52 m^2g^{-1}). Similarly, a significantly larger pore volume of 3DOM Co_3O_4

of 0.441 cm^3 g^{-1} has been obtained, which is found to be more than 40 times greater than that of bulk Co_3O_4 (0.011 cm^3 g^{-1}). These results obtained with 3DOM Co_3O_4 is attributed to the existence of mesopores consistently observed in the results of the pore size distribution (**Figure 4-3b inset**). The high surface area of the well-ordered mesoporous structure of 3DOM Co_3O_4 not only facilitates the diffusion of oxygen and electrolyte but also increases catalyst active surface area utilization resulting in improved electrochemical battery performance.

The electronic structure of 3DOM Co_3O_4 has been revealed by X-ray photoelectron spectroscopy (XPS), where the existence of Co and O has been confirmed as expected. Furthermore, the high-resolution XPS spectrum of Co 2p showing two pairs of spin-orbit doublets deconvoluted spectra suggest the coexistence of Co^{2+}/Co^{3+} cations in 3DOM Co_3O_4 (**Figure 4-4**).[93] The bifunctional catalytic activity of spinel Co_3O_4 towards both ORR and OER are attributed to the mixed-valences of coexisting cobalt cations facilitating electron transfer by providing donor-acceptor chemisorption sites for both reversible oxygen adsorption and desorption in the cubic spinel structure. This results in relatively low activation energies for ORR and OER for spinel Co_3O_4 leading to accelerated rates of the oxygen surface reactions.

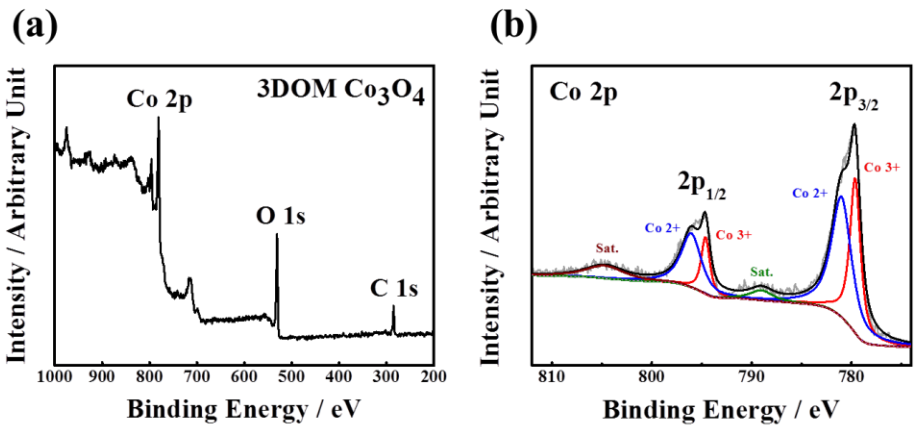

Figure 4-4. a) Full XPS spectrum of 3DOM Co_3O_4 and b) high-resolution XPS showing Co 2p core-level spectrum of 3DOM Co_3O_4.

To investigate the advanced morphological effect of 3DOM Co_3O_4 on bifunctional electrocatalytic activity, three-electrode half-cell testing has been conducted in both the ORR and OER regimes. In terms of ORR (**Figure 4-5a**), the polarization curve obtained with 3DOM Co_3O_4 exhibits positively shifted onset and half-wave potentials (-0.197 and -0.360 V vs. SCE) as well as a much higher magnitude of limiting current (-4.71 mA cm^{-2}). In comparison, the bulk shaped Co_3O_4 shows limited ORR activity, exhibiting relatively negative shifted onset and half-wave potentials (-0.234 and -0.394 V vs. SCE) and lower magnitude limiting current density (-3.57 mA cm^{-2}). A similar trend of morphological effect is observed with the activity of OER (**Figure 4-5b**), where 3DOM Co_3O_4 displays higher OER activity by offering improvement in current density of 21.17 mA cm^{-2} at 0.7 V vs. SCE. Relatively lower ORR and OER Tafel slopes of 3DOM Co_3O_4 have resulted in 72 mV and 58 mV per decade, respectively, in comparison to those of bulk Co_3O_4 (84 mV and 90 mV per decade) indicative of faster kinetics during the electrocatalytic reactions of oxygen as expected (**Figure 4-6**). This could be derived from the enlarged catalytic surface area of 3DOM Co_3O_4 compared to that of bulk shaped spinel cobalt oxide. The ORR activity enhancement of 3DOM Co_3O_4 is attributed to the extended surface area and 3-D architectural morphology previously confirmed by BET and TEM characterizations, respectively (**Figure 4-3**). Since the electrochemical oxygen reactions such as ORR and OER are based on a surface catalytic reaction, the larger exposed area typically provides more surface catalytic active sites toward ORR and OER for the sake of enhanced electrocatalytic performances. Compared to bulk Co_3O_4, 3DOM Co_3O_4 has a large number of pores allowing the advanced catalyst to have drastically expanded surface area and thereby increased number of catalytic active sites.

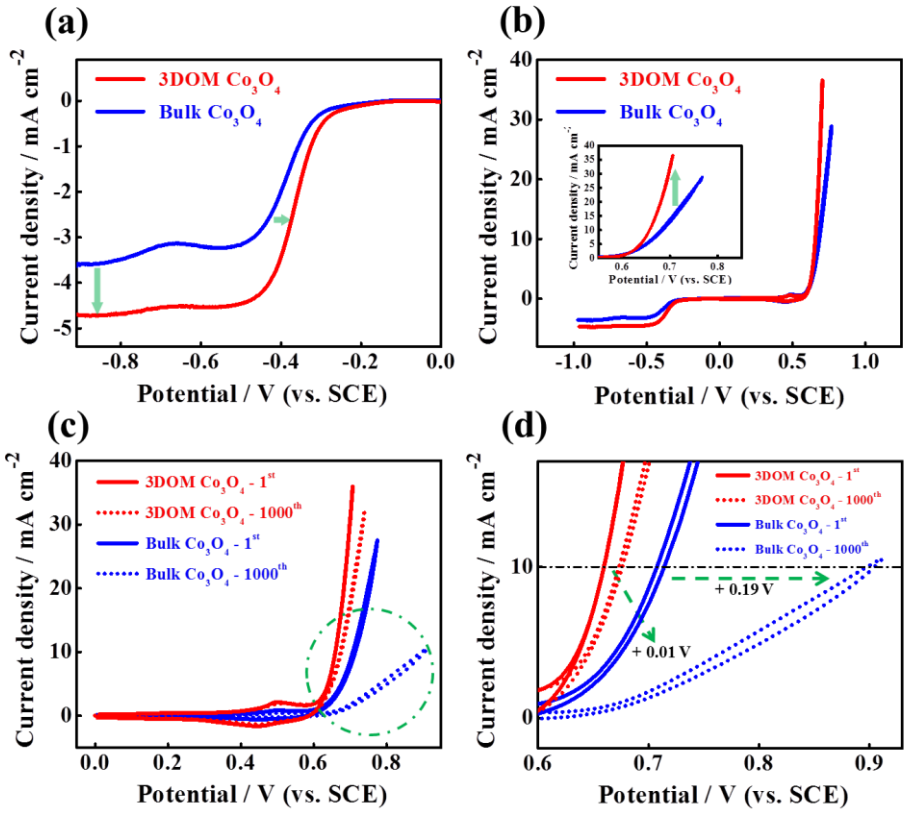

Figure 4-5. a) ORR polarization curves and b) full range ORR and OER polarization curves (rotation speed: 1600rpm, sweep rate: 10 mV S^{-1}) for 3DOM and bulk Co_3O_4. Inset is a detailed comparison between OER activities of the prepared catalysts; c and d) OER polarization curves during cycling durability tests (rotation speed: 1600rpm, sweep rate: 50 mV S^{-1}) for 3DOM and bulk Co_3O_4 after 1000 cycles. Test results in the green circle are enlarged to verify the specific change in the working potential of prepared catalysts.

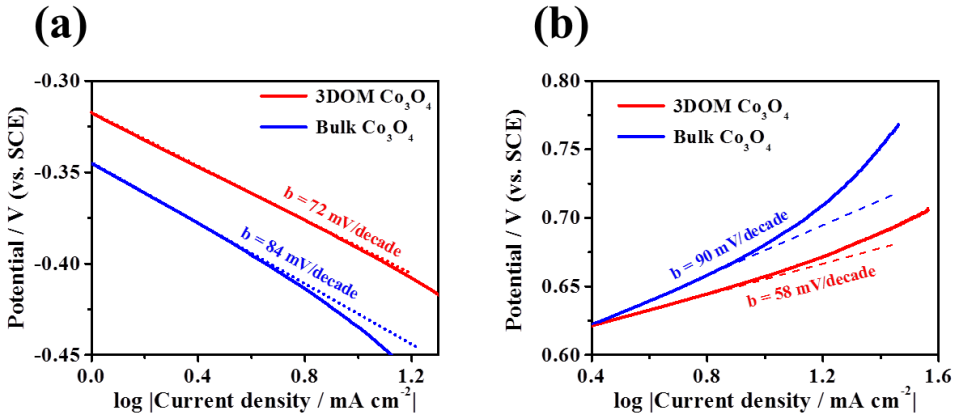

Figure 4-6. Tafel plots correspond to (a) ORR polarization curves and (b) OER polarization curves of 3DOM and bulk Co_3O_4, respectively.

In addition to the effect of improved porosity, the 3-D hierarchical architecture of 3DOM Co_3O_4 also contributes to the enhanced ORR and OER performance in that during the electrochemical reaction, and the cobalt oxide framework serve as pathways for electron transfers which are rigorously generated by the highly catalytic oxygen reactions. The number of electron transfer has been obtained by Koutecky-Levich (K-L) plots, and 3DOM Co_3O_4 shows 3.9 over a wide range of potential transferring close to four electrons (**Figure 4-7**).

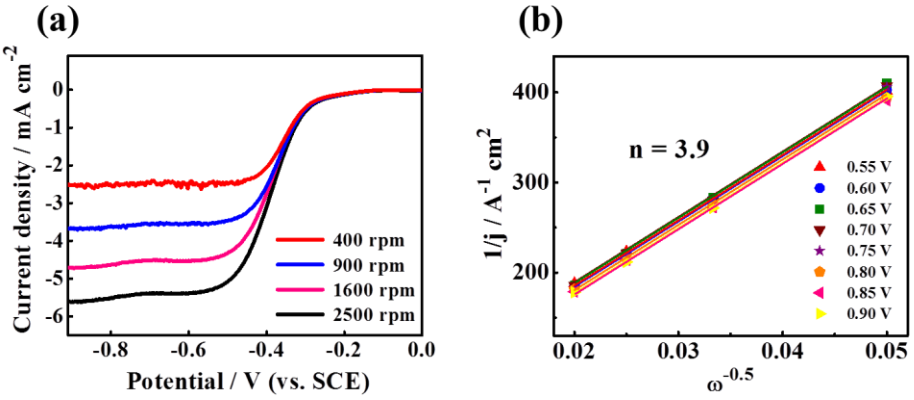

Figure 4-7. a) ORR polarization curves of 3DOM Co_3O_4 obtained at various rotating speeds (400, 900, 1600 and 2500 rpm) and b) K-L plot of 3DOM Co_3O_4 obtained between 0.55 and 0.90 V. The potential points are basically determined in a range of mass transfer controlled area during ORR. ORR experiments were conducted in O_2-saturated 0.1 M KOH solution in ambient conditions (rotation speed 1600 rpm, sweep scan rate 10 mV s^{-1}).

In addition to the excellent bifunctional electrocatalytic activity of 3DOM Co_3O_4 observed, electrochemical durability has been investigated by conducting CV in the high potential OER region, which exposes catalysts under more severe conditions (**Figure 4-5c**). After 1000 CV cycles in the OER potential range, the recorded potential of 3DOM Co_3O_4 at 10 mA cm^{-2} has increased only by 13 mV, while bulk Co_3O_4 has demonstrated a much more substantial increase of 190 mV. The electrochemical durability results in terms of OER potential

change at 10 mA cm^{-2} are more clearly presented in **Figure 4-5d**, where bulk Co_3O_4 is observed to degrade more severely after repeated cycling, demonstrated by more substantial positive potential shift. Interestingly, the final OER current density of 3DOM Co_3O_4 after cycling is higher than the initial OER performance of bulk Co_3O_4, demonstrating its high electrocatalytic activity and durability towards OER. This observed higher electrocatalytic stability of 3DOM Co_3O_4 than the bulk Co_3O_4 is majorly due to the fact that even though an agglomeration of catalyst particles happens during the repeated CV cycling in the harsh potential region, the 3DOM framework can retain its high exposed surface area coming from its open and porous structural characteristic, while the bulk whose catalytic active sites primarily reside onto the surface would experience severe decrease in the number of active sites due to the agglomeration process significantly lowering the contact area with the reactants such as gaseous oxygen and electrolyte.

In parallel, ORR durability of Co_3O_4 also is investigated by comparing the initial ORR activity and the final one that is obtained after the 1000 CV cycles in the OER potential region, as shown in **Figure 4-8**. While bulk Co_3O_4 presents largely increased ORR overpotential with far reduced current density indicating significant catalyst degradation, 3DOM Co_3O_4 demonstrates much smaller overpotential gain and relatively low reduction of ORR current density. This observation clarifies the excellent electrocatalytic stability of 3DOM architecture in both ORR and OER potential region, which is directly indicative of the promising bifunctionality of 3DOM Co_3O_4.

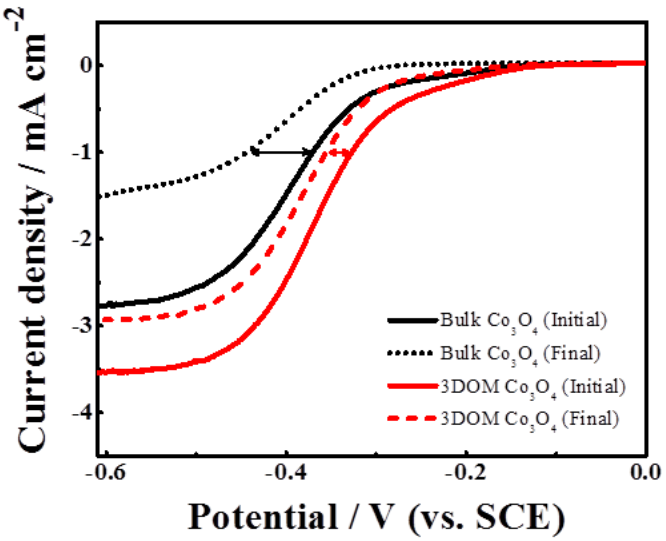

Figure 4-8. ORR polarization curves before OER cycling (Initial) and after OER cycling (Final) of both 3DOM and bulk Co_3O_4. The rotation speed was 900 rpm for all tests.

Precious metal-based bifunctional catalyst created by mixing Pt/C and Ir/C has also been evaluated by half-cell testing, including ORR and OER activity tests and OER cycling durability tests, to further verify the practical viability of 3DOM Co_3O_4 (**Figure 4-9**). The ORR activity of the precious bifunctional catalyst is relatively higher than that of 3DOM Co_3O_4. With respect to OER activity, however, 3DOM Co_3O_4 shows comparable OER performance to that of the precious bifunctional catalyst. The slightly lower OER activity of 3DOM Co_3O_4 is compensated by its significantly lower price and higher abundance than the precious metal-based catalysts, Pt/C and Ir/C. More importantly, however, the precious catalysts are only uni-functionally active towards either ORR or OER, which is why both Pt/C and Ir/C are required to demonstrate ORR and OER, respectively. Utilizing 3DOM Co_3O_4 as a bifunctionally active catalyst, on the other hand, allows demonstration of both ORR and OER on a single active catalyst.

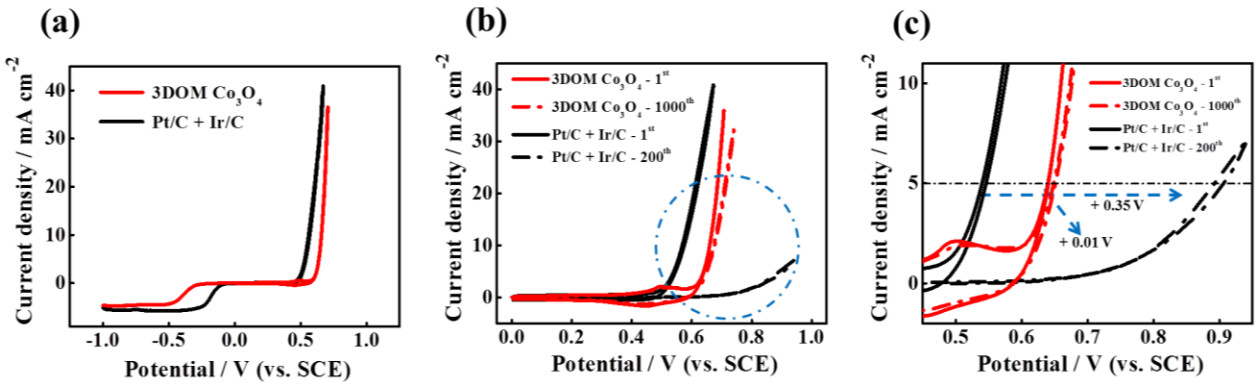

Figure 4-9. RDE half-cell tests: a) Full range ORR and OER polarization curves in O_2-saturated and N_2-saturated 0.1 M KOH solution at room temperature (rotation speed 1600 rpm, sweep rate 10 mV S^{-1}) for 3DOM Co_3O_4 and Pt/C+Ir/C as non-precious and precious catalysts, respectively. b-c) OER polarization curves during cycling durability tests in N2-saturated 0.1 M KOH solution at room temperature (rotation speed 1600rpm, sweep rate 50 mV S^{-1}) for 3DOM Co_3O_4 and Pt/C+Ir/C after 1000 cycles and 200 cycles, respectively. Test results in the blue circle are enlarged to verify the detailed change in the working potential of the prepared catalysts. The overpotentials by the difference between ORR and OER of each catalyst are listed in Table 4-1.

In terms of the OER cycling durability test, even though the initial cycle of the precious catalyst slightly outperforms 3DOM Co_3O_4 in terms of the onset potential and current density, Pt/C + Ir/C becomes very unstable only after 200 cycles demonstrating significantly lowered OER activity majorly due to severe carbon corrosion happening within the high OER potential range. The OER potential is positively shifted by 0.35 V to reach 10 mA cm^{-2} only after 200 cycles as opposed to the shift of only 0.01 V after 1000 cycles obtained with 3DOM Co_3O_4 (**Figure 4-9c**). In addition to excellent oxygen electrocatalytic activities, it is necessary for catalysts to have excellent electrochemical stability under the severe environment high potentials incurred during OER. The robust hierarchically ordered frames of 3DOM Co_3O_4 effectively helps to withstand harsh cycling conditions by demonstrating significantly smaller performance degradation and maintaining the original morphology. The durability of 3DOM Co_3O_4 after cycling is verified by performing TEM analysis in terms of morphology, where the initial

mesoporous framework with highly ordered architecture is observed to remain intact (**Figure 4-10**). The neighboring particles are Vulcan Carbon (VC) physically mixed with 3DOM Co_3O_4 during electrode fabrication. This trend directly correlates with the results of the previous ORR and OER tests in that the electrocatalytic durability of 3DOM Co_3O_4 is exceptionally high by exhibiting only 13 mV of potential shift at 10 mA cm^{-2} even after 1000 cycles as well as undergoing no morphological changes during the long term electrochemical test. A relatively small shift of 13 mV of the OER potential at 10 mA cm^{-2} after cycling is likely due to highly robust three dimensional 3DOM structure, where a considerable amount of internal pores is maintained, resulting in the maintenance of a highly active surface area and catalytic activity even after OER cycling. Bulk Co_3O_4, on the other hand, demonstrates a much more severe OER potential shift of 190 mV after cycling, resulting in significant OER activity loss.

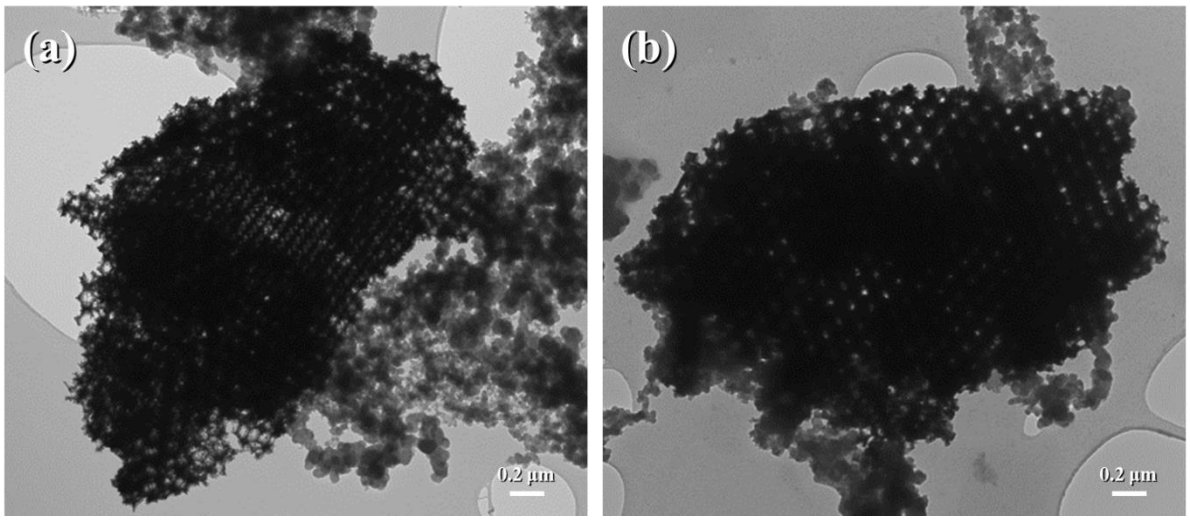

Figure 4-10. TEM images of 3DOM Co_3O_4 (a) before and (b) after the OER durability cycling test (1000 cycles).

To demonstrate electrochemically bifunctional catalytic performance of 3DOM Co_3O_4 in realistic environments, electrically rechargeable Zn-air battery prototypes have been fabricated,

and electrochemical performances have been evaluated. As the air electrode, the as-synthesized catalyst has been incorporated into a nickel-based single-layered air electrode. **Figure 4-11a** presents a schematic illustration of the rechargeable Zn-air battery design utilized in this present study, and **Figure 4-11b** presents a working prototype consisting of two Zn-air batteries connected in series operating in ambient conditions utilizing atmospheric air as the source of fuel. **Figure 4-11c** presents charge and discharge polarization curves (V *vs. i*) of air electrodes with 3DOM Co_3O_4, bulk 3DOM Co_3O_4, and Pt/C + Ir/C galvanodynamically obtained in a wide range of applied current density. With respect to open-circuit voltage (OCV), the precious catalyst demonstrates 1.42 V, which is slightly higher than that of 3DOM Co_3O_4 (1.36 V), whereas bulk Co_3O_4 results in the lowest OCV (1.28 V). The order of the above values is related to the potential of each catalyst most likely based on the intrinsic resistance, which is in the same order of performance demonstrated by ORR and OER half-cell electrochemical tests. Superior discharge and charge voltages of 3DOM Co_3O_4 are clearly observed in the galvanodynamic discharge and charge polarization profiles at the applied current range. During discharge, 3DOM Co_3O_4 shows a remarkably low rate of the potential drop while the current is increased by maintaining the battery potential above 1.2 V until the current density passes 30 mA cm^{-2}. However, bulk Co_3O_4 quickly loses its discharge potential, exhibiting 1.2 V at 5 mA cm^{-2}, with the potential gap between the discharge profiles of 3DOM Co_3O_4 and bulk Co_3O_4 gradually increased at higher current densities. The potential difference between 3DOM Co_3O_4 and Pt/C+Ir/C is relatively significant at a low current due to the high OCV of the precious catalyst. At high discharge current, however, the difference is tiny, elucidating that 3DOM Co_3O_4 has a comparable rate of battery potential drop to that of Pt/C+Ir/C. During charge, the overall increase of charge potential of 3DOM Co_3O_4 is slightly higher than that of Pt/C+Ir/C, but far lower than

that of bulk Co_3O_4. From the potential gap between discharge and charge polarization curves measured at high current density (50 mA cm^{-2}), the overpotential of the catalysts can be obtained. Pt/C+Ir/C presents 0.76 V, 3DOM Co_3O_4 shows 0.85 V, and lastly, Co_3O_4 displays 1.07 V, indicating the comparable catalytic activity of 3DOM Co_3O_4 to that of Pt/C+Ir/C. The results correspond to the trend of overpotentials between ORR and OER evaluated by electrochemical half-cell tests. Power density curves are also acquired by applying current density and measuring discharge voltage within the applied range of current density (**Figure 4-11d**). 3DOM Co_3O_4 presents a highly similar power density to that of Pt/C+Ir/C, whereas bulk Co_3O_4 shows much lower values. The excellent rechargeable Zn-air battery performance of 3DOM Co_3O_4 combined with its excellent cost competitiveness over the precious metal-based bifunctional catalyst clearly demonstrates its potential for practical usage in commercially rechargeable Zn-air batteries.

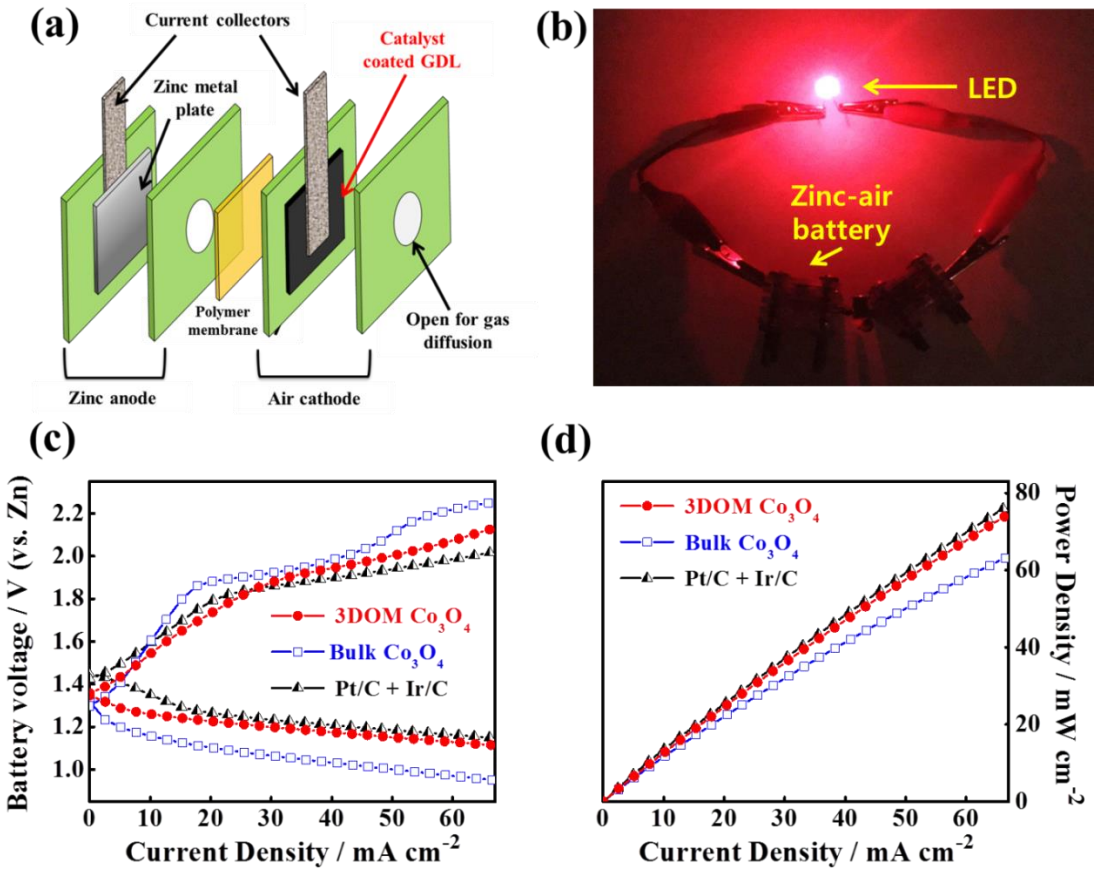

Figure 4-11. Electrochemical performance of the electrically rechargeable Zn-air battery prototypes using 3DOM Co_3O_4, Bulk Co_3O_4, and Pt/C+Ir/C as air electrode bifunctional catalysts. a) schematic illustration of rechargeable Zn-air battery design. b) The prototype in operation consists of two Zn-air batteries in ambient conditions. c-d) galvanodynamic charge and discharge polarization curves and corresponding power density plots of air electrode bifunctional catalysts such as 3DOM Co_3O_4(red circle), Bulk Co_3O_4(blue square), and Pt/C+Ir/C(green triangle).

In **Figure 4-12**, galvanostatic charge and discharge battery cycling tests have been performed by applying 10 mA cm^{-2} and 2 h cycle periods to investigate the rechargeability of the catalyst coated air electrodes in the Zn-air battery. 3DOM Co_3O_4 displays a significantly long battery lifetime over 200 cycles (more than 400 hours) without increasing overpotential measured by voltage gap between discharge and charge potentials (**Figure 4-12a**). In contrast, bulk Co_3O_4 and Pt/C+Ir/C demonstrates limited battery lifetimes by performing only 90 and 7

cycles, respectively, before displaying severely enlarged overpotentials derived from the increased charge potential and decreased discharge potential during cycling (**Figure 4-12b and 12c**). In **Figure 4-12d**, the charge and discharge potentials of the catalysts are demonstrated to highlight the initial performance and durability of 3DOM Co_3O_4 relative to the other tested catalysts. During the first four cycles, Pt/C+Ir/C shows the smallest potential difference of 0.71 V between charge and discharge, and 3DOM Co_3O_4 demonstrates a comparable potential difference of 0.76 V, whereas bulk Co_3O_4 shows the most significant difference of 0.84 V (**Table 4-1**). After four cycles, however, Pt/C+Ir/C rapidly loses its catalytic activity towards ORR and OER, resulting in both severely degraded charge and discharge voltages. Furthermore, the performance of Pt/C+Ir/C noticeably declines after six cycles resulting in drastically enlarged charge and discharge potential difference of ~1.4 V. This severe performance loss is likely due to carbon corrosion at high voltages, as well as dissolution and agglomeration of the precious metal catalyst.[101] Although bulk Co_3O_4 exhibits longer cycle life than the precious metal catalysts, its rechargeable battery performance also rapidly decreases after 90 cycles, which is inferior compared to stable charge and discharge voltages of 3DOM Co_3O_4 over 200 cycles.

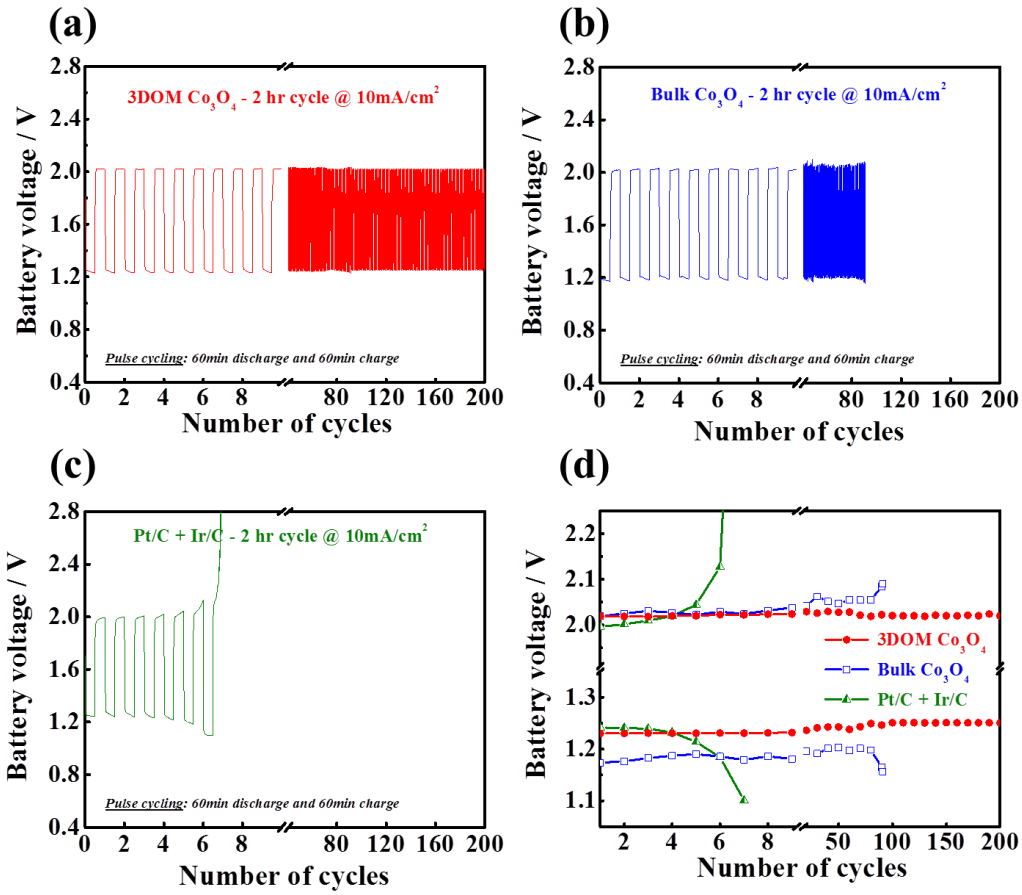

Figure 4-12. Electrochemical galvanostatic charge and discharge cycling curves of the electrically rechargeable Zn-air battery prototypes; a) 3DOM Co_3O_4, b) bulk Co_3O_4, and c) Pt/C+Ir/C as air electrode bifunctional catalysts, and d) the first 10 battery cycles for all prepared catalysts for comparing initial performances. Battery operations in ambient conditions (each cycle period: 2 h; 1h for discharge and 1 h for charge, current density: 10 mA cm^{-2}, pure oxygen gas purged to air electrode).

	Discharge potential (A)	Charge Potential (B)	Charge-discharge voltage difference between A and B
3DOM Co_3O_4	1.24 V	2.0 V	0.76 V
Bulk Co_3O_4	1.19 V	2.03 V	0.84 V
Pt/C+Ir/C	1.27 V	1.98 V	0.71 V

Table 4-1. The performance of rechargeable Zn-air batteries using various electrocatalysts. Charge and Discharge voltages at 10 mA cm^{-2} and charge-discharge voltage difference for the prepared catalysts under ambient conditions.

4.4 Summary

Conclusively, all of the electrochemical characterizations such as half-cell testing, galvanodynamic and galvanostatic charge and discharge cycling tests have demonstrated consistent trends in performances including electrocatalytic activity and durability of the catalysts. In comparison to the other electrocatalysts, 3DOM Co_3O_4 introduces highly advanced and innovative morphology and a 3-D hierarchical honeycomb-like mesoporous structure, which leads to improved electrochemical durability as well as highly active bifunctional performances (discharge and charge potential: 1.24 V and 2.0 V at 10 mA cm^{-2}) confirmed by both half-cell testing (1000 OER CV cycles) and rechargeable Zn-air battery cycling experiments (200 charge/discharge cycles).

5. Second Transition Metal deposition on 3DOM Co_3O_4 for Enhanced Bifunctional Activity and Durability

This chapter is reprinted in adapted form from the below article[102] with permission from the Elsevier.

Park, M. G., M. H. Seo, D. U. Lee, X. Wang, W. Ahn, S. H. Noh, S. M. Choi, Z. P. Cano, B. Han, Z. Chen, "Bifunctionally Active and Durable Hierarchically Porous Transition Metal-based Hybrid Electrocatalyst for Rechargeable Metal-Air Batteries", *Applied Catalysis B: Environmental*, 239 (2018) 677-687.

5.1 Introduction and Motivation

Increased awareness of the harmful effects of fossil fuel use, and accompanying greenhouse gas emissions causing global climate change, have led to a rigorous push for the development of sustainable energy conversion and storage systems.[103, 104] There has been tremendous interest in pursuing both fundamental and applied research towards developing new types of sustainable energy systems such as fuel cells and metal-air batteries,[104, 105] which are expected to have positive impacts on commercialization of smart-grid energy storage and electric vehicles shortly.[106] In particular, metal-air batteries boasting extremely high volumetric and gravimetric energy densities have recently been in the spotlight of energy research for further development of advanced energy storage applications.[11, 105, 107] However, the current metal-air battery systems have a few critical challenges, including i) large overpotentials resulting from sluggish oxygen reduction reaction (ORR) and oxygen evolution reaction (OER) kinetics and ii) catalyst degradation due to relatively unstable electrochemistry during repetitive discharge and

charge cycles. These challenges arise from insufficient activity and durability of the air electrode, one of the main components of a metal-air battery, which includes electrocatalysts that lower activation energies of the reactions to reduce overpotential associated with discharge and charge processes.[15] Hence, recent research efforts in energy materials development have focused on addressing the above challenges, which would ultimately enable commercialization of electrically rechargeable metal-air batteries.[62, 71, 89, 108-115]

Recent approaches combining density functional theory (DFT) and *ab-initio* studies with experimental studies have allowed researchers to precisely simulate catalytic activities and gain fundamental understandings of the oxygen reactions.[116, 117] Further, they have enabled the development of sufficiently active low-cost catalysts by allowing not only the design of efficient non-precious material-based catalysts but also the effective minimization of noble metal loadings in noble metal-based catalysts. Some examples of these oxygen reaction catalysts include non-precious transition metal-based materials (Mn_xO_y, Co_xO_y, $NiCo_xO_y$, $LaNi_xO_y$, etc.),[62, 69, 71, 113-115, 118] functionalized carbon-based materials (heteroatom-doped graphene and carbon nanotubes, etc.),[59, 109-111] metal–nitrogen complexes ($M\text{-}N_x/C$),[119-121] and noble metal-based materials (Pt_3Ni, Pt_3Co, Pt_3Y, etc.).[122, 123] As one of the most notable examples, Pt_3Ni was revealed by Nørskov and associates to show enhanced ORR activity relative to Pt due to a downward shifted d-band center in its electronic structure, which results in weaker adsorption with oxygen intermediates on the catalytic surface.[122, 124-130] For non-precious catalysts such as metal–nitrogen complexes and metal oxides, understanding the e_g orbital of valence electrons makes it possible to predict the oxygen reactivity, which can be controlled by the number of outer electrons of transition metals.[71, 131-133] The electrochemical stability during the oxygen reduction and evolution reactions has been associated with the dissolution potential and cohesive energy term, which can

be modified by changing morphology and size of the transition metal nanoparticles as well as the supporting materials.[134-137] However, most reports incorporating the above design strategy have focused solely on catalytic activities without also considering long-term durability.

Regarding the stability of rechargeable metal-air batteries, thermodynamic electrochemical durability of cathode materials is extremely restricted due to their instability during the charging process, which typically occurs at high potentials (over 0.4 V vs. SHE). This potential range is comparable to the ORR potential region of fuel cell systems using acidic media; these harsh conditions can dissolve metal and carbon-based catalysts, resulting in severe degradation of their electrochemical performance. Although metal oxides are generally more able to retain their solid phase during metal-air battery charging, they are usually not solely used because of their poor conductivity due to band gaps in their electronic structure. Therefore, carbon materials are typically required as conductive and dispersive additives within the electrode, inevitably leading to inherent thermodynamic instability due to CO_2 oxidation above 0.207 V vs. RHE.

Herein, a highly efficient and durable bifunctional oxygen electrocatalyst was designed to address the above challenges by combining three-dimensionally ordered mesoporous spinel cobalt oxide (3DOM-Co_3O_4) with palladium (Pd) nanoparticle deposition. Morphological advantages of the 3DOM structure of Co_3O_4 facilitating diffusion of oxygen molecules in and out of the structure can lead to reduced overpotentials for the ORR and OER. Pd was introduced into the 3DOM Co_3O_4 by expecting synergistic effects, especially to take full advantage of its significant stability as solid-phase below 0.810 V vs. SHE (Standard Hydrogen Electrode) by the Nernst equation with using 10^{-6} M of Pd^{2+}(aq) at pH=0, as well as the well-known excellent electrocatalytic ORR activity. Resulting from our systematic prediction, we demonstrated

synergistically enhanced bifunctional activity and durability within the operating conditions of electrically rechargeable metal-air batteries. Besides, the catalyst was modeled with DFT-based *ab-initio* analysis to elucidate the underlying catalytic mechanisms and interpret the carbon oxidation potentials ($U_{corr,C}$) on the surface of the various catalysts, as well as the dissolution potential (U_{diss}) of various Pd species on the catalyst surface to validate its remarkably high durability. Overall, this investigation provides a framework for rationally designing bifunctional catalysts based on the thermodynamic principles that govern electrochemical stabilities for corrosion-resistant electrocatalysis, and demonstrates the application of the developed catalyst in a single-cell rechargeable Zn-air battery to highlight its performance and durability.

5.2 Experimental Methods

5.2.1 Synthesis of Pd@3DOM-Co_3O_4

Three-dimensionally ordered mesoporous spinel cobalt oxide (3DOM-Co_3O_4) was prepared by a facile sacrificing template method. First, polystyrene (PS) beads were synthesized by a simple polymerization employing styrene monomer, potassium persulfate ($K_2S_2O_8$), and polyvinylpyrrolidone (PVP) all bought from Sigma-Aldrich Canada. 2.5 g of PVP was dissolved in 200 mL of distilled de-ionized (DDI) water heated to 70 ^oC. Next, the styrene monomer (24 mL) was added into the mixture, and a specific volume of $K_2S_2O_8$ dissolved DDI water (5 g L^{-1}) was slowly poured into the solution. The polymerization process was carried out for 24 h under vigorous stirring with a condenser used for preventing evaporation of the solution. Additionally, N_2 gas continuously was purged into the flask to keep oxygen absent from the environment. The resultant PS solution was centrifuged at a low rate for more than 12 h to obtain a well-layered PS

mass followed by a drying process at 60 ^{o}C. The well-layered PS beads were employed as a template material in this method, where the spherical PS beads conform to a three-dimensionally ordered hierarchically porous Co_3O_4 structure with regularly connected voids. In a specific synthesis of 3DOM-Co_3O_4, the PS beads were soaked for 4 h in a precursor solution of cobalt nitrate hexahydrate (30 mmol), citric acid (30 mmol) and ethanol (20 ml), allowing the solution to fill its voids. After drying at ambient temperature for 24 h, the materials were heat-treated at 300 ^{o}C in an airstream (ramp rate of 1 ^{o}C min^{-1}) for 3 h to simultaneously melt the PS beads and solidify the cobalt precursor into the 3DOM structure. The annealed product was placed in a mixture of acetone and hexane (volume ratio of 1:1) at 60 ^{o}C for 30 min to dissolve the remaining PS, followed by drying at 80 ^{o}C for 4 h. The dried material was calcined in an airstream at 400 ^{o}C (ramp rate of 1 ^{o}C min^{-1}) for 3 h to obtain the crystal structure of spinel cobalt oxide with a robust 3DOM framework (3DOM-Co_3O_4). Next, Pd-deposited 3DOM-Co_3O_4 was synthesized by a facile reduction process. As-prepared 3DOM-Co_3O_4 (72 mg) was added into a round-bottom flask (50 mL) with Pd precursor solution in which the 30 mg $PdCl_2$ (weight percent of Pd to Co_3O_4 of 20 %) was dissolved in a mixture of ethanol and hydrochloric acid with a volume ratio of 12:1. The mixture was gently stirred with a magnetic bar and refluxed for 6 h with the addition of 10 mL ethylene glycol solution, followed by filtration and washing with ultrapure water. Finally, the obtained composite was dried at 80 ^{o}C under vacuum condition. As a reference, 20 wt.% Pd/C was also synthesized by the same method where activated carbon black was used instead of 3DOM-Co_3O_4 as the support.

5.2.2 Half-cell Electrochemical Measurements

A traditional three-electrode configuration, consisting of glassy carbon (GC) electrode, platinum wire, and saturated calomel electrode (SCE) as the working electrode, counter electrode and reference electrode, respectively, were utilized to evaluate the electrochemical performance of the catalysts at room temperature. The electrocatalytic activities for ORR and OER were measured by a rotating disc electrode (RDE) half-cell technique and cyclic voltammetry (CV), where a CHI Electrochemical Station (Model 760D) was used to evaluate the performances. The tests were performed from 0 to −1.0 V vs. SCE at 1600 rpm for ORR and from 0 to 1.0 V vs. SCE at 1600 rpm for OER. The scan rate for both electrochemical tests was 10 mV s^{-1}. The accelerated degradation testing (ADT) was conducted by performing CV (~1000 cycles) in the OER potential region of 1-2 V vs. RHE with a scan rate of 50 mV s^{-1}. The potential versus SCE was converted to potential versus RHE at room temperature according to $E_{RHE} = E_{SCE} + 0.241 + 0.0591pH$. The electrolyte was purged with pure oxygen and nitrogen gas for 30 min before ORR and OER measurements, respectively. The ORR polarization curves in the oxygen-saturated electrolyte were corrected by subtracting background curves, which were obtained in the nitrogen-saturated electrolyte, to eliminate capacitive currents during the ORR tests. All measurements were conducted in a 0.1 M KOH solution. The measured overpotentials (η) for ORR and OER were based on the standard oxygen reduction potential (E^o = 1.23 V vs. RHE), where η_{ORR} = 1.23 V − measured ORR potential (vs. RHE) and η_{OER} = measured OER potential (vs. RHE) − 1.23 V. Before testing, the GC electrode (diameter: 5 mm) was polished using alumina suspension (particle size: 0.05 μm) on a smooth polishing cloth. The catalyst ink was prepared by mixing 4 mg of the catalyst and Vulcan Carbon (XC-72) (mass ratio of 1:1) in 1 mL of isopropanol (IPA) pre-treated by Nafion solution (0.3 wt.%) followed by ultrasonication for

30 min to obtain a homogeneous ink. 20 µL of the as-prepared ink was dropped with a micropipette onto the GC surface and dried under ambient conditions, leading to a catalyst loading of 0.2 mg $cm^{-2}_{catalyst}$. Precious metal catalysts consisting of platinum carbon (Pt/C, 28.8 wt. % Pt), iridium carbon (Ir/C, 20 wt. % Ir) and palladium carbon (Pd/C, 20 wt. % Pd) were used as reference materials (without blending with Vulcan Carbon) to demonstrate the relative catalytic efficiency and practicality of bifunctionally active and stable Pd@3DOM-Co_3O_4.

5.2.3 Rechargeable Zn-Air Battery Performance Evaluation

An air electrode was prepared by spray-coating the catalyst ink solution onto a gas diffusion layer (Ion Power Inc., SGL Carbon 35 BC) with an airbrush onto an active area of 0.785 cm^2 (catalyst loading: 1 mg cm^{-2}). The catalyst ink was prepared by mixing the catalyst and Vulcan Carbon in Nafion-containing (5 wt. %) isopropanol (IPA) with a weight ratio of 1:1, followed by ultrasonication for 1 h to obtain a homogeneously dispersed ink solution. Similarly, to the half-cell evaluations, the commercial carbon-supported precious metal catalysts (Pt/C and Ir/C) were used to prepare reference air electrodes by the same method (without Vulcan Carbon). A zinc plate (OnlineMetals, Zinc Sheet EN 988), a microporous polypropylene membrane (Celgard 5550), and a 6.0 M KOH solution with 0.2 M zinc acetate were employed as the anode, separator, and electrolyte, respectively. Stainless steel meshes were utilized as current collectors for both anode and cathode sides. Galvanodynamic discharge and charge experiments were carried out with a multichannel potentiostat (Princeton Applied Research, VersaSTAT MC). With a wide range of currents (current density: 0 to ~ 60 mA cm^{-2}), discharge and charge profiles were obtained. Zn-air single-cell cycling tests were operated by a cycling tester (BTSDA). The cycling was performed with 10 minutes cycles (5 minutes discharge and 5 minutes charge) and a

high current density of 10 mA cm^{-2}. Long term cycling tests were also conducted, where one cycle was 10 hours (5 hours each for discharge and charge) at a relatively low current density (1 mA cm^{-2}).

5.2.4 Computational Modeling and Design

Density functional theory (DFT) calculations implemented in the Vienna ab initio simulation package (VASP) program were utilized for the present study.[116, 117, 138] Exchange-correlation energies of electrons were described by the Perdew, Burke, and Ernzerhof (PBE) functional for generalized gradient approximation (GGA).[139, 140] Core electrons were replaced by the projector augmented wave (PAW) pseudopotentials,[141, 142] and Kohn-Sham wave functions of valence electrons were expanded by the plane-wave basis set with cut-off energy of 520 eV. The Hubbard U parameter (GGA+U) was employed to improve the description of correlation effects and to reduce the self-interaction error in bulk Co_3O_4.[143-145] The optimized effective interaction parameter U_{eff} (U_{eff} = U – J) of 3.4 eV was used for Co ions in the Co_3O_4 structure. All ions were fully relaxed during the structural optimization until the total energy was converged within 10^{-4} eV. A gamma point mesh with (15 × 15 × 15) k-points was used for the Co_3O_4 (1 × 1) unit cell to sample the Brillouin zone for bulk calculation. Periodic boundary conditions were imposed on these unit cells in terms of the (001) surface direction, and a vacuum space of 20 Å was employed to avoid interactions between the top and bottom surface. The first five layers were fixed from the bottom, and the rest of the layers were relaxed., A gamma point mesh of (5 × 5 × 1) and the Methfessel-Paxton smearing method were utilized to calculate the total energies of Co_3O_4 slab models on the (001) surface direction.[146] On the relaxed Co_3O_4 slab model, Pd (3 × 2√3) and carbon monolayers (4 × 2√3) were deposited on the (001) Co_3O_4 surface. For the density of states (DOS) calculations, the tetrahedron method with Blçchl's corrections was

employed.[147] From the projected density of states (p-DOS) of a Pd atom, d-band center values of Pd on the Co_3O_4 surface are estimated using equations (1):[148]

$$\varepsilon_d = \frac{\int_{-\infty}^{E_F} E p_d(E) dE}{\int_{-\infty}^{E_F} p_d(E) dE} \quad (1)$$

Here, ε_d is d-band center weight, and p_d is the projected density of states onto the d band of a Pd atom.

5.3 Results and Discussion

The schematic synthesis in **Figure 5-1** shows the facile synthesis procedure used to prepare Pd@3DOM-Co_3O_4. 3DOM-Co_3O_4 was prepared by the template-assisted method using spherical PS beads, resulting in the structure shown in **Figure 5-2 and 5-3a**. Chemical deposition of Pd was conducted on the surface of 3DOM-Co_3O_4 to obtain the final material, Pd@3DOM-Co_3O_4. As shown in **Figure 5-3b**, the 3DOM structure is observed, which was maintained after the deposition of Pd by the reflux method. In addition to the TEM analysis, SEM characterization was conducted to verify the overall 3D morphologies of 3DOM Co_3O_4 after the deposition of Pd. The 3DOM structure is observed to be uniform over a large area, highlighting the robust synthesis technique and the resulting high surface area available for ORR and OER to occur. Detailed HR-TEM inspection of the pristine 3DOM-Co_3O_4 surface shown in **Figure 5-3a-1** reveals the typical (001) cubic surface of Co_3O_4 (space group: *Fd3m* (227), JCPDS no. 42-1467), while the surface particles shown in **Figure 5-3b-1** displays the (111) FCC face of Pd, confirmed by fast Fourier transform (FFT) diffraction. The elemental mapping of 3DOM-Co_3O_4 before Pd deposition shown in **Figure 5-3a-2** reveals Co and O distributed throughout the

3DOM backbone. The elemental mapping of Pd@3DOM-Co_3O_4, on the other hand, reveals a mostly uniform distribution of Pd (with a few regions with higher concentration) in addition to Co and O, as presented in **Figure 5-3b-2**.

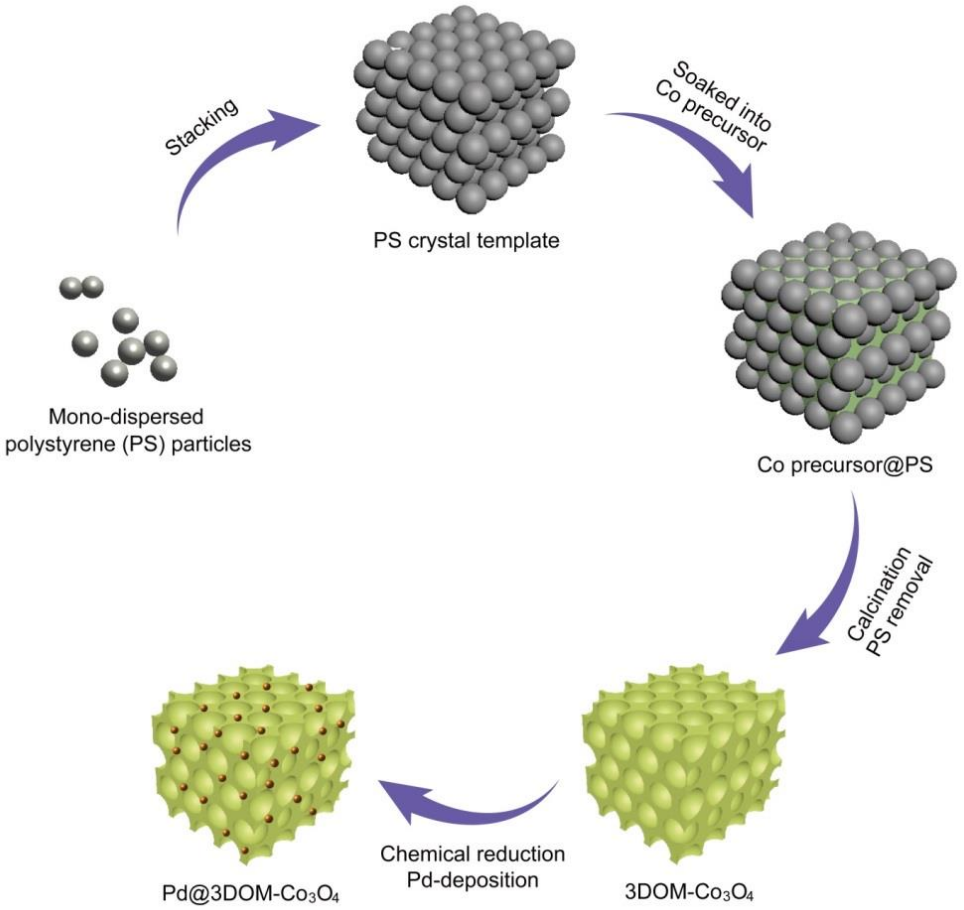

Figure 5-1. Schematic synthesis of Pd-deposited 3D ordered mesoporous spinel cobalt oxide (Pd@3DOM-Co_3O_4)

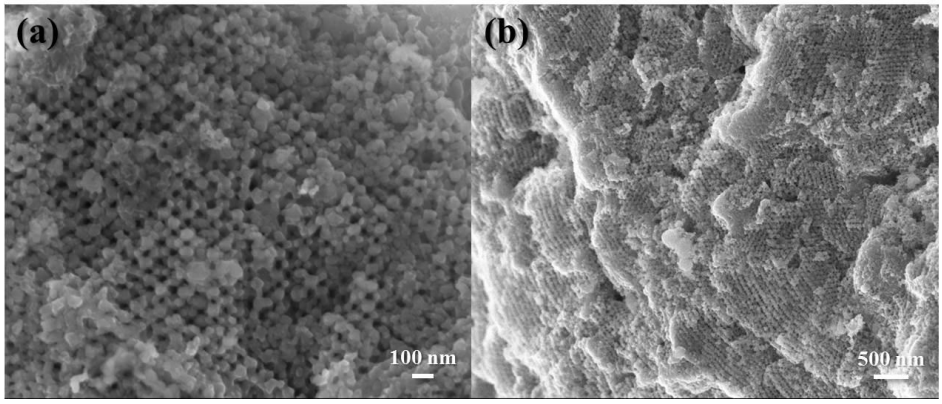

Figure 5-2. SEM images of Pd@3DOM-Co_3O_4 at (a) high, and (b) low magnifications

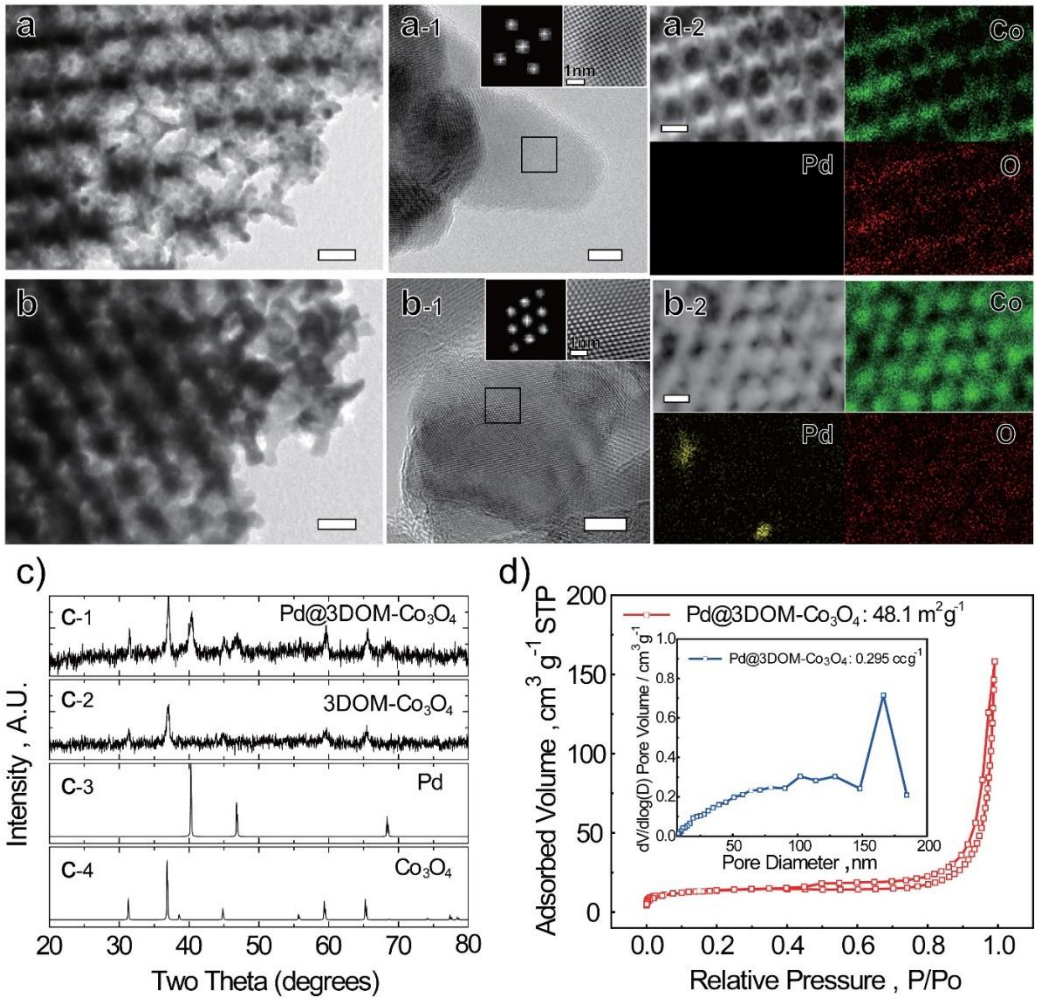

Figure 5-3. Morphological and structural characterization of Pd@3DOM-Co_3O_4. a and b) HRTEM images of 3DOM-Co_3O_4 and Pd@3DOM-Co_3O_4, respectively (Scale bar, 50 nm), with (a-1 and b-1) selected area electron diffraction (SAED) pattern (Scale bar, 5 nm) and (a-2 and b-2) element mapping images including cobalt (green), Pd (yellow), and oxygen (red) (Scale bar, 50 nm), c) X-ray diffraction (XRD) patterns of (c-1) Pd@3DOM-Co_3O_4 and (c-2) 3DOM-Co_3O_4 investigated in this study, and the bulk (c-3) Pd and (c-4) Co_3O_4, calculated XRD patterns based on ICSD, d) Nitrogen adsorption-desorption isotherm (Red) and pore size distribution (Blue) of Pd@3DOM-Co_3O_4.

Additionally, the XRD pattern of Pd@3DOM-Co_3O_4 (**Figure 5-3c**) shows typical peaks representative of both FCC Pd and cubic Co_3O_4, as observed in the TEM images before and after Pd deposition. The XRD patterns of Pd@3DOM-Co_3O_4 and 3DOM-Co_3O_4 (**Figure 5-3c-1** and

5-3c-2) are consistent with those of bulk Pd, and Co_3O_4 (**Figure 5-3c-3** and **3c-4**) obtained from ICSD #64915 and #24210, respectively, confirming the successful formation of the Pd@3DOM-Co_3O_4 composite. The hierarchically porous morphology of Pd@3DOM-Co_3O_4 gives rise to a high specific surface area, which increases the active site exposure for the oxygen reactions. To confirm this, N_2 adsorption-desorption isotherm of Pd@3DOM-Co_3O_4 was obtained (**Figure 5-3d**), which showed a typical type IV isotherm with a type II contribution and a clear H3 hysteresis loop in the higher relative pressure (P/Po) range of 0.45-1.0, which are characteristics of a mesoporous structure. The BET measurement revealed a specific surface area of 48.1 $m^2g^{-1,}$ and the BJH adsorption pore distribution result (**Inset of Figure 5-3d**) indicated the existence of mesopores with a dominant pore diameter of 170 nm, consistent with pore sizes observed in the micrographs above. The 3DOM structure is particularly beneficial in terms of facilitating the diffusion of gaseous oxygen and liquid electrolyte as well as improving the active material utilization, resulting in an overall electrochemical performance enhancement.

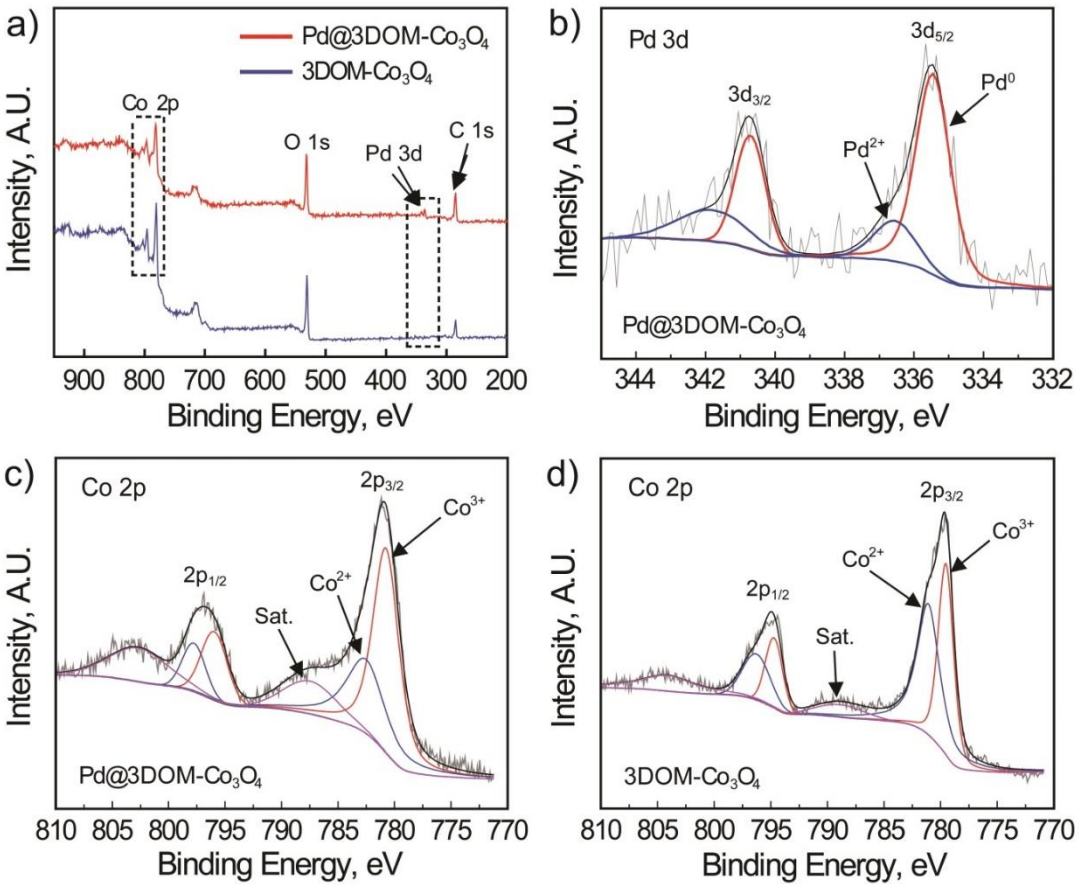

Figure 5-4. Investigations on catalyst surface information of Pd@3DOM-Co_3O_4 by X-ray photoelectron spectroscopy (XPS). a) full XPS survey scan of Pd@3DOM-Co_3O_4 and 3DOM-Co_3O_4 and deconvoluted Pd 3d (b) and Co 2p (c) peaks in Pd@3DOM-Co_3O_4 and Co 2p (d) peak in 3DOM-Co_3O_4.

To further elucidate the electronic structures and surface elemental composition of the prepared 3DOM-Co_3O_4 and Pd@3DOM-Co_3O_4 materials, X-ray photoelectron spectroscopy (XPS) was conducted. As expected, the full XPS survey scan (**Figure 5-4a**) of Pd@3DOM-Co_3O_4 (red line) clearly revealed the existence of Co, Pd and O, while 3DOM-Co_3O_4 (blue line) showed only Co and O. Moreover, the high resolution Pd 3d and Co 2p spectra of Pd@3DOM-Co_3O_4 (**Figure 5-4b** and **5-4c**) and 3DOM-Co_3O_4 (**Figure 5-4d**) were de-convoluted to investigate the relationship between the electronic structures and surface elemental composition

of the catalysts and their effects on electrocatalytic performances. In the d-band center theory, the electronic structure of the surface metal and its catalytic activity is correlated, and the core-level binding energy shift of a metal is an indicator for changes in the center of the occupied d-states.[149, 150] The binding energy (BE) of the spin-orbit split doublet (Pd $3d_{5/2}$ and Pd $3d_{3/2}$) for Pd@3DOM-Co_3O_4 (**Figure 5-4b**) appeared at approximately 335.46 and 340.78 eV (red lines), respectively, which are attributed to the presence of metallic Pd (Pd^0). Another doublet, with BEs for Pd $3d_{5/2}$ and $3d_{3/2}$ peaks at approximately 336.56 and 341.96 eV (blue lines) are attributed to a higher oxidation state similar to that of PdO (Pd^{2+}). The peak positions of metallic Pd are shifted to higher BE as the d-d orbital hybridization increases between Pd and Co_3O_4, compared with the core level BE (e.g., 335.3 eV for Pd $3d_{5/2}$) of Pd nanoparticles supported on carbon as shown in our previous study.[150] This indicates that the d-band center value of Pd on 3DOM-Co_3O_4 is downward shifted compared to that of pure Pd, suggesting the potential to demonstrate a higher ORR activity. In the case of Co 2p in Pd@3DOM-Co_3O_4 and 3DOM-Co_3O_4 (**Figure 5-4c** and **5-4d**, respectively), the mixed valences of Co^{3+}/Co^{2+} were evaluated. The mixed valences of coexisting cobalt cations facilitate electron transfer by donor-acceptor chemisorption for reversible oxygen adsorption and desorption in the cubic spinel structure.[150, 151] The binding energies of Co^{3+} (Co $2p_{3/2}$ and Co $2p_{1/2}$) were observed at 780.86 and 796.06 eV (red lines in **Figure 5-4c**) for Pd@3DOM-Co_3O_4, and 779.52 and 794.72 eV (red lines in **Figure 5-4d**) for Co_3O_4, respectively. In Pd@3DOM-Co_3O_4, the Co^{3+}/Co^{2+} ratio was relatively higher than in Co_3O_4, indicating that some Co^{2+} was oxidized to Co^{3+} after Pd deposition. This led to electron transfer from Co_3O_4 to metallic Pd, resulting in a downward shift of the d-band center of Pd on 3DOM-Co_3O_4, which enhances the ORR activity.

Regarding the OER activity of Co_3O_4, there is a debate about whether Co^{2+} or Co^{3+} is the

active site. Among recently reported studies, Wang et al. demonstrated Co^{2+} is the active site using a series of in operando techniques,[152] whereas Menezes et al. have claimed Co^{2+} is catalytically inactive citing several reports.[153, 154] Likewise, Siwen et al. have demonstrated that Co^{3+} is more catalytically active than Co^{2+} for OER by synthesizing Co^{3+} rich composition.[155] Our results support the latter work since increased Co^{3+} density in the Pd@3DOM-Co_3O_4 revealed higher OER catalytic activity.

To investigate the electrocatalytic activities of Pd@3DOM-Co_3O_4 toward both ORR ($O_2 + 2H_2O + 4e^- \rightarrow 4OH^-$) and OER ($4OH^- \rightarrow O_2 + 2H_2O + 4e^-$), rotating disk electrode (RDE) voltammetry was carried out in the half-cell condition.[114, 156] The cyclic voltammetry (CV) of Pd@3DOM-Co_3O_4, 3DOM-Co_3O_4, Pt/C, Pd/C, and Ir/C was conducted in N_2-saturated 0.1 M KOH, with results shown in **Figure 5-5**.

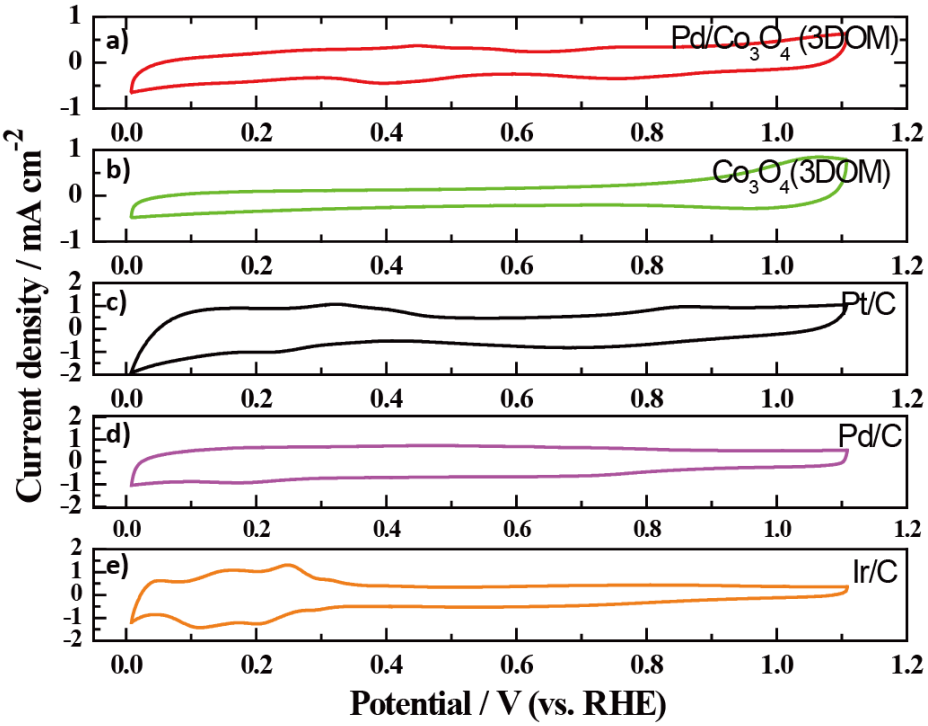

Figure 5-5. Cyclic voltammograms for (a) Pd@Co3O4 (3DOM), (b) Co_3O_4 (3DOM), (c) Pt/C, (d) Pd/C, and (e) Ir/C in N_2 saturated 0.1M KOH electrolyte with 50 mV sec^{-1} scan rate.

ORR polarization curves shown in **Figure 5-6a** and **Figure 5-7a** demonstrated superior catalytic activity of Pd@3DOM-Co_3O_4 towards ORR in comparison to 3DOM-Co_3O_4 as well as Pt/C, Pd/C and Ir/C precious-metal benchmark catalysts, by evaluating the half-wave potential ($E_{1/2}$), specific kinetic current (j_k) normalized by geometric area, and ORR potential at the current density of − 0.1 mA cm^{-2} (E_{ORR}) (refer to **Table 5-1**). Particularly, Pd@3DOM-Co_3O_4 is observed to demonstrate comparable $E_{1/2}$, E_{ORR}, and j_k (0.881 V, 0.986 V, and 2.74 mA cm^{-2} at 0.9 V vs. RHE, respectively) compared to those of state-of-the-art Pt/C (0.898 V, 1.00 V, and 3.71 mA cm^{-2} at 0.9 V vs. RHE, respectively).[157] Meanwhile, the ORR curve of Pd/C exhibits a negatively shifted $E_{1/2}$, E_{ORR}, and lower j_k (0.861 V, 0.981 V, and 1.59 mA cm^{-2} at 0.9 V vs. RHE, respectively) compared to those of Pt/C. Moreover, the number of electrons transferred (n) during ORR on Pd@3DOM-Co_3O_4 was obtained to investigate the electron pathway of the electrocatalytically active sites (**Figure 5-8**). The K-L slope obtained by the Koutecky–Levich (K–L) plot corresponded to almost four electrons (n≈3.9) transferred, demonstrating a pseudo-four electron pathway, which is further indicative of the excellent ORR kinetics of Pd@3DOM-Co_3O_4.

Besides the electrochemical ORR activity, OER activity of the catalysts was investigated by CV, as shown in **Figure 5-6b** and **Figure 5-7b**. Both Pd/C and Pt/C demonstrated poor OER activities with a current density lower than 13 mA cm^{-2} at 2.0 V, which was expected due to their well-known insufficient bifunctionality towards both oxygen reactions. 3DOM-Co_3O_4, on the other hand, demonstrated significantly higher OER activity with a relatively lower overpotential of 0.41 V (1.64 V vs. RHE at 2.0 mA cm^{-2}) and much higher current density of 34.8 mA cm^{-2} at 2.0 V due to its structural advantages discussed above. Interestingly, Pd@3DOM-Co_3O_4 demonstrated even higher current density of 41.3 mA cm^{-2} at 2.0 V with a lower overpotential of

0.38 V relative to 3DOM-Co_3O_4. When compared to Ir/C (one of the best known OER benchmark noble catalysts), which demonstrated a very high E_{OER} (1.57 V vs. RHE) and current density at 2.0 V (40.6 mA cm^{-2}), Pd@3DOM-Co_3O_4 performed very similarly in terms of both E_{OER} and current density. The overall electrochemical results are shown in **Table 5-1**. In brief, Pd@3DOM-Co_3O_4 demonstrates enhanced bifunctional activities towards both ORR and OER, which is attributed to the synergy between chemically deposited-Pd and 3DOM-Co_3O_4. This will be further discussed and elucidated by *ab-initio* computational studies.

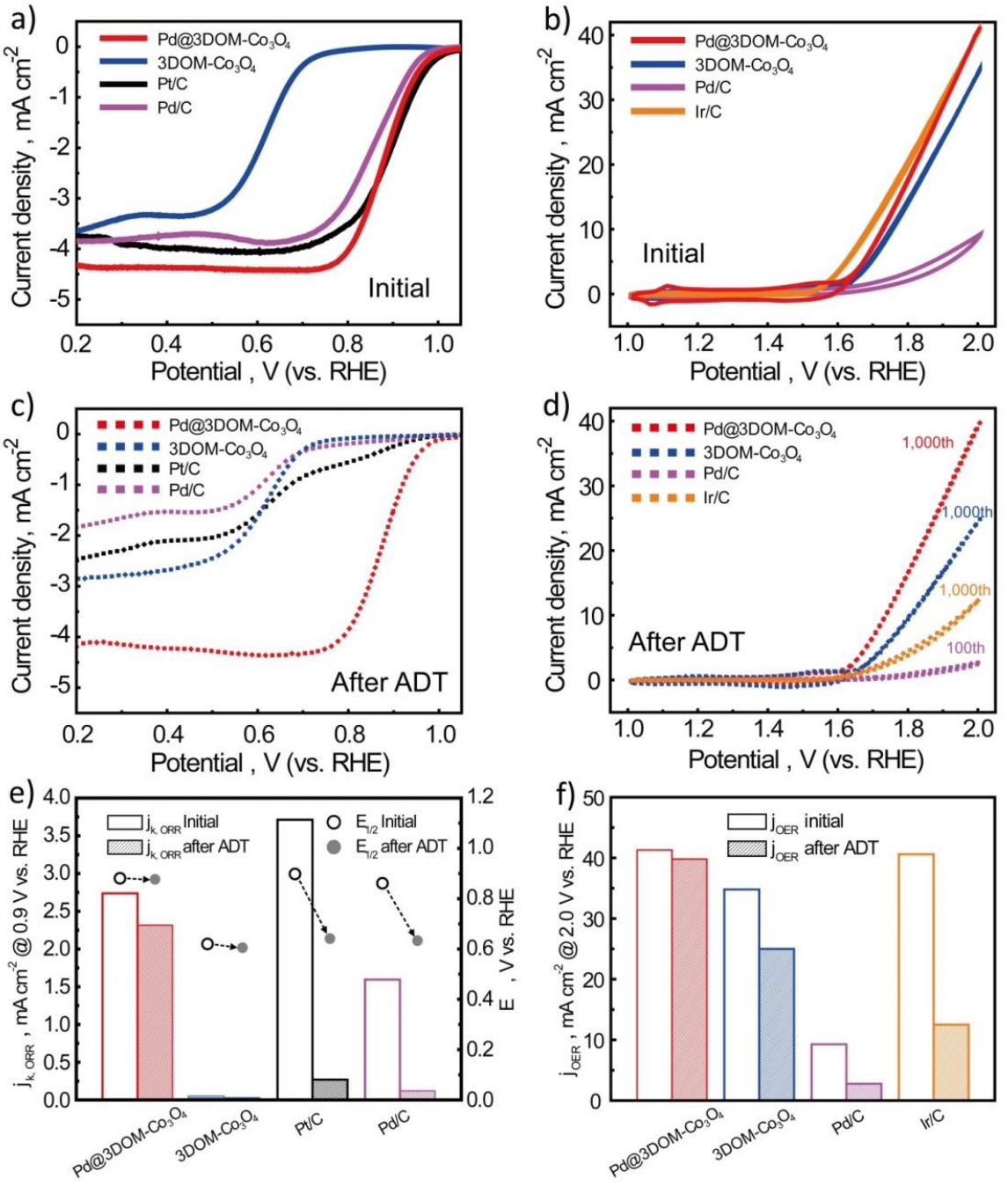

Figure 5-6. Evaluation of oxygen reduction and evolution reaction (ORR and OER). (a and b) initial ORR and OER polarization curves of Pd@3DOM-Co_3O_4, 3DOM-Co_3O_4, Pd/C, and Pt/C or Ir/C, respectively, and (c and d) final (after accelerated degradation testing (ADT)) ORR and OER polarization curves of Pd@3DOM-Co_3O_4, 3DOM-Co_3O_4, Pd/C, and Pt/C or Ir/C, respectively, (e) changes in specific kinetic current density and ORR half-wave potential of the electrocatalysts before and after ADT, (f) change in OER current density at 2.0 V vs. RHE of the electrocatalysts before and after ADT.

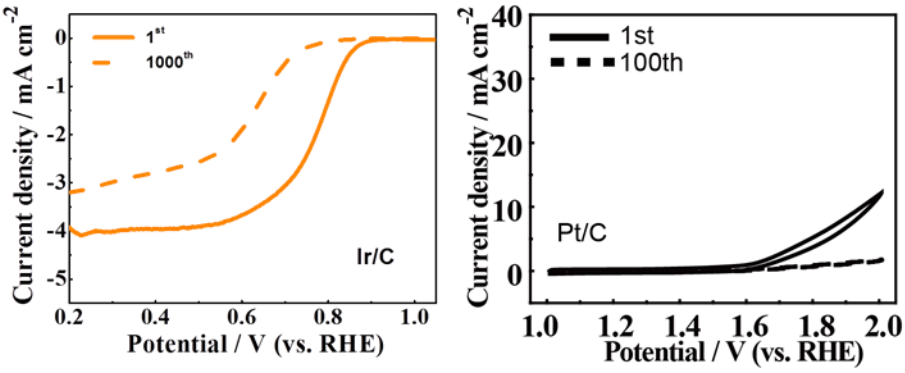

Figure 5-7. ORR and OER polarization curves of Ir/C and Pt/C, respectively, before and after the accelerated degradation test (ADT)

Table 5-1. Comparison of ORR and OER activity data before/after acceleration degradation testing (ADT) (1000 cycles in potential range from 1.0 V to 2.0 V vs. RHE among various catalysts.

Catalysts	ORR					
	E_{ORR}[a] @ − 0.1 mA cm^{-2}, V		$E_{1/2}$[b], V		j_k, mA cm^{-2} @ 0.9 V	
	Before	After	Before	After	Before	After
Pd@3DOM-Co_3O_4	0.986	0.978	0.881	0.877	2.737	2.316
3DOM-Co_3O_4	0.733	0.723	0.620	0.605	-	
Ir/C	0.881	0.784	0.772	0.637	-	
Pd/C	0.981	0.785	0.861	0.633*	1.594	0.119
Pt/C	1.00	0.913	0.898	0.641*	3.713	0.269
Catalysts	OER					
	E_{OER}[c] @ 2 mA cm^{-2}, V		j @ 2 V vs. RHE, mA cm^{-2}		ΔE[d] (=E^c-E^a), V	
	Before	After	Before	After	Before	After
Pd@3DOM-Co_3O_4	1.611	1.666	41.3	39.8	0.625	0.683
3DOM-Co_3O_4	1.641	1.672	34.8	25.0	0.908	0.949
Ir/C	1.573	1.728	40.6	12.5	0.692	0.944
Pd/C	1.725	1.961	9.27	2.76	0.744	1.176
Pt/C	1.675	2 <	12.2	1.72	0.675	2 <

E_{ORR}[a] = E_{ORR} defined at − 0.1 mA cm^{-2}
$E_{1/2}$[b] = Half-wave potential
E_{OER}[c] = E_{OER} defined at 2 mA cm^{-2}
* : potentials of the catalysts were obtained only after 100 cycles in ADT

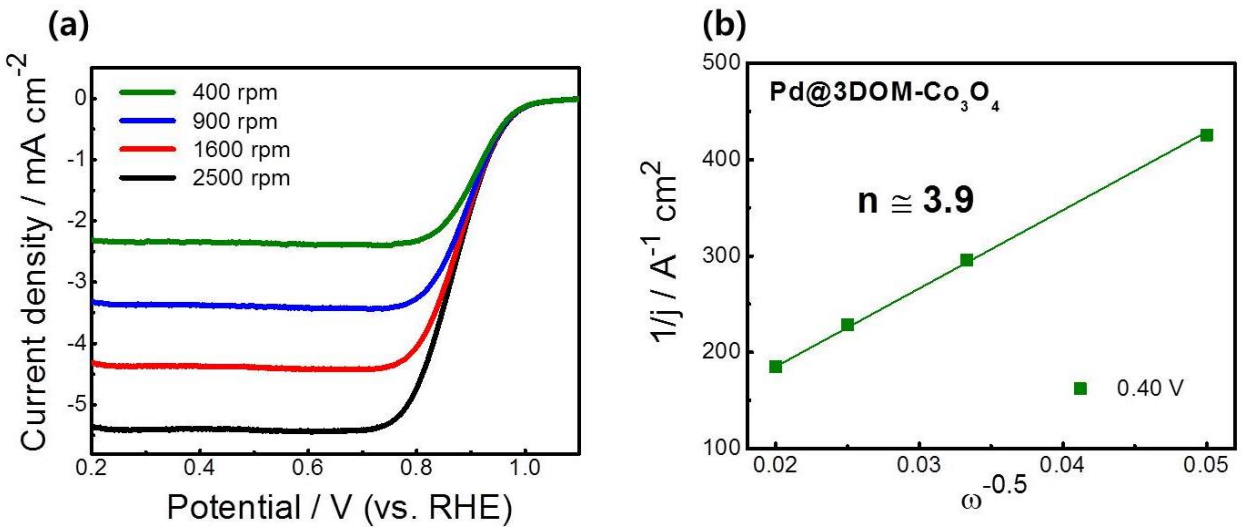

Figure 5-8. a) ORR polarization curves of Pd@3DOM-Co_3O_4 obtained at various rotating speeds (400, 900, 1600 and 2500 rpm) and b) K-L plot of 3DOM Co_3O_4 obtained at 0.4 V (vs. RHE). The potential points are basically determined in a range of mass transfer controlled area during ORR. The ORR experiments were conducted in O2-saturated 0.1 M KOH solution in ambient conditions (sweep scan rate 10 mV s-1).

The DFT calculations provide insight into the electronic structure and corroborate the enhanced electrocatalytic activity of Pd@3DOM-Co_3O_4. Through modification of the electronic band structure by Pd-deposition, the electron abundance at the Fermi level is increased in the DOS of Co (**Figure 5-9**) leading to higher electrical conductivity of Pd@3DOM-Co_3O_4 than 3DOM-Co_3O_4 alone. This indicates the chemical deposition of Pd helps Co_3O_4 to have much improved electrical conductivity jumping over the poor nature of Co_3O_4 itself, and this triggers more rapid electron transfers during both oxygen reactions (ORR and OER), resulting in improved electrocatalytic activities. Regarding oxygen adsorption kinetics through d-band theory,[127, 130] Pd typically has a high-lying d-band center ($\varepsilon_d = -1.82$ eV) that increases oxygen binding energy, leading to slower kinetics for ORR.[122, 129, 150] The combination of deposited Pd with the 3DOM-Co_3O_4 support, however, results in improved ORR performance of Pd@3DOM-Co_3O_4. This is attributed to the modified electronic structure of chemically deposited Pd,

resulting in a low-lying d-band weight (ε_d = −1.98 eV, calculated as described in the experimental section) which designates weaker bonding with oxygen.

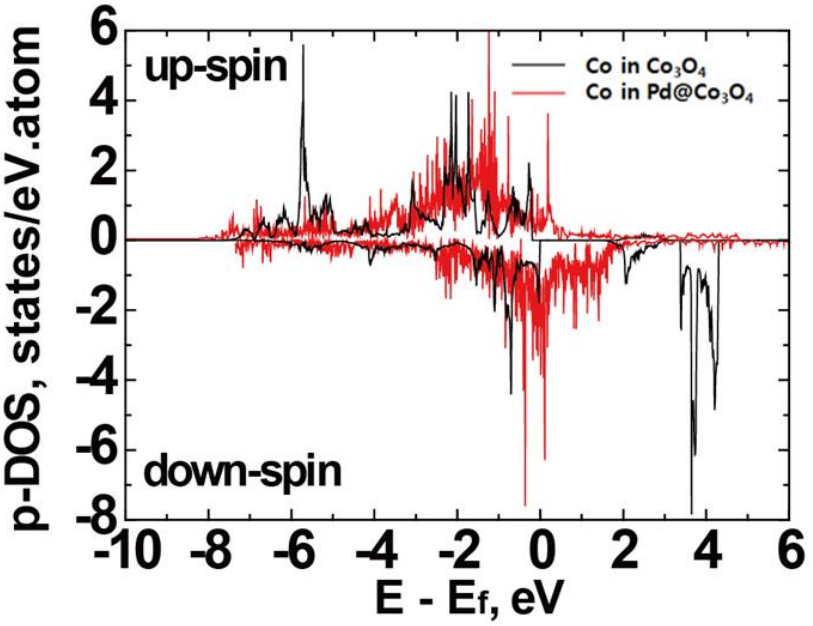

Figure 5-9. The projected density of state (p-DOS) of Co in Co_3O_4 and Pd@Co_3O_4, denoted by the black and red line, respectively. Fermi energy is the energy zero in all cases.

The degradation pathways of catalysts in electrochemical devices are known to proceed by electrochemical dissolution of metals, oxide formation, agglomeration, and corrosion of support materials.[105, 135, 136, 158] In metal-air batteries, high potentials incurred during charging pose harsh conditions for catalysts to retain their original electrochemical surface properties and electrocatalytic activities due to the extremely oxidative irreversible reactions.[18] To demonstrate and explain the excellent electrocatalytic durability of Pd@3DOM-Co_3O_4, direct electrochemical dissolutions of metal catalysts and corrosion of carbon supports were investigated through both experiment and *ab-initio* study (see the initial models of the catalysts surface in **Figure 5-10**. Accelerated degradation testing (ADT) was conducted via repetitive CV (1000 cycles) in the

OER potential region with a scan rate of 50 mV s^{-1} to systematically evaluate the electrocatalytic stability of Pd@3DOM-Co_3O_4 towards OER relative to the other catalysts. After 1000 repetitive OER cycles (only 100 cycles applied to Pd/C and Pt/C), the polarization curves and current densities obtained at 2.0 V vs. RHE for each catalyst are summarized in **Figure 5-6d** and **5-6f**, respectively, and in **Table 5-1**. The highest current retention (at 2.0 V vs. RHE) was observed with Pd@3DOM-Co_3O_4 (96.4 %) compared to 3DOM-Co_3O_4 and benchmarks Pd/C and Ir/C (71.8 %, 29.8 %, and 30.8 %, respectively). This highlights the extremely durable nature of Pd@3DOM-Co_3O_4 towards the electrochemical oxidative conditions of OER typically occurring in the high overpotential range. Similarly for ORR, Pd@3DOM-Co_3O_4 demonstrates negligible half-wave potential and specific kinetic current losses with very high retentions of 99.5 % and 84.6 %, respectively, compared to those of Pt/C (71.7 % and 7.2 %), and Pd/C (73.5 % and 7.5 %) as shown in **Figure 5-6c** and **5-6e**, which is in good agreement with the durability results in OER. 3DOM-Co_3O_4 without Pd displays very low specific kinetic current densities at 0.9 V vs. RHE both before and after ADT since it has virtually no electrochemical ORR activity at 0.9 V vs. RHE and the onset potential is more negative than 0.9 V, as demonstrated in **Figure 5-6a** and **5-6c**. Based on these electrochemical tests, superior ORR and OER activities and excellent electrochemical durability of Pd@3DOM-Co_3O_4 were observed, which will be further investigated by DFT computational analysis.

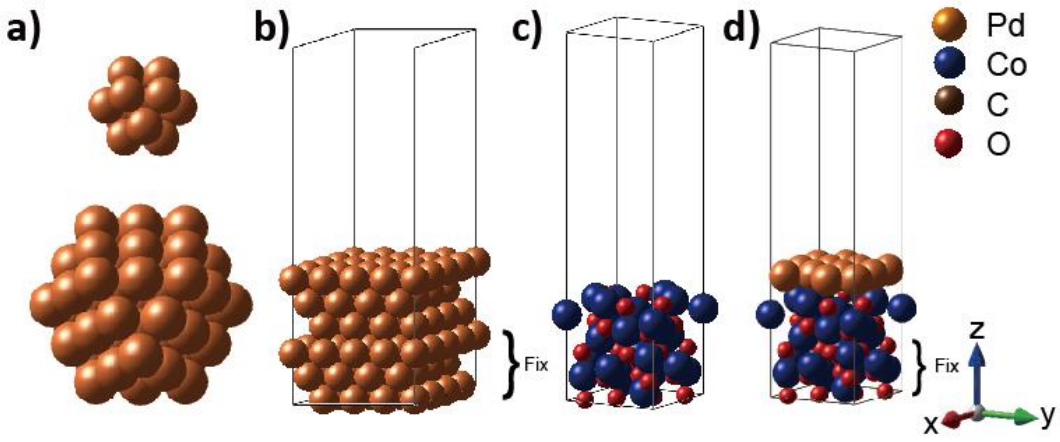

Figure 5-10. (a) Relaxed Pd_{13}(top) and Pd_{55}(bottom) nanoparticles and slab models of (b) Pd (c) Co_3O_4 (001) surface and (d) Pd monolayer deposited on Co_3O_4 (001) surface.

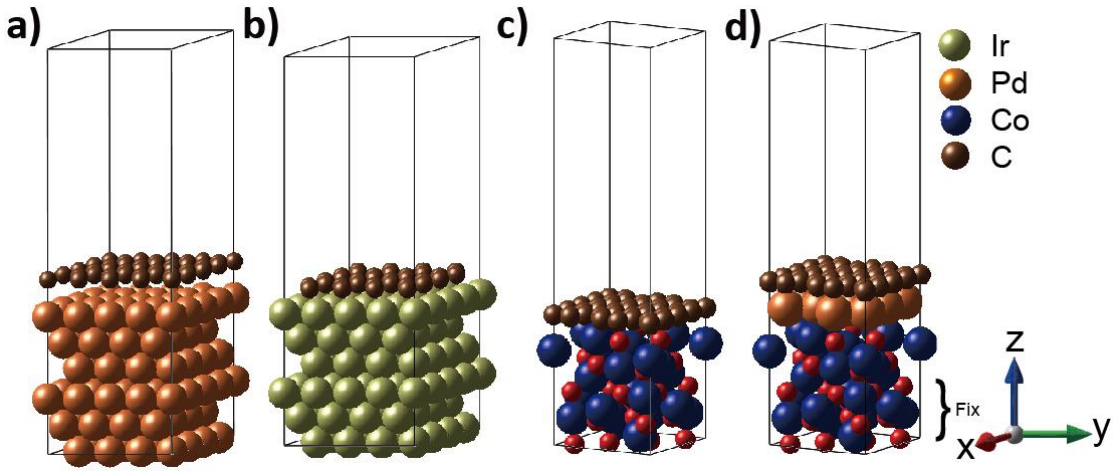

Figure 5-11. Initial model system of graphene deposited on Pd, Ir, Co_3O_4 (001), and Pd/Co_3O_4 (001).

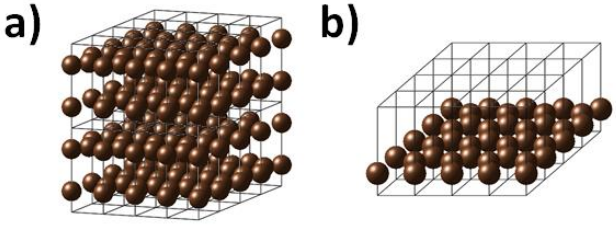

Figure 5-12. The designed model for (a) graphite and (b) graphene

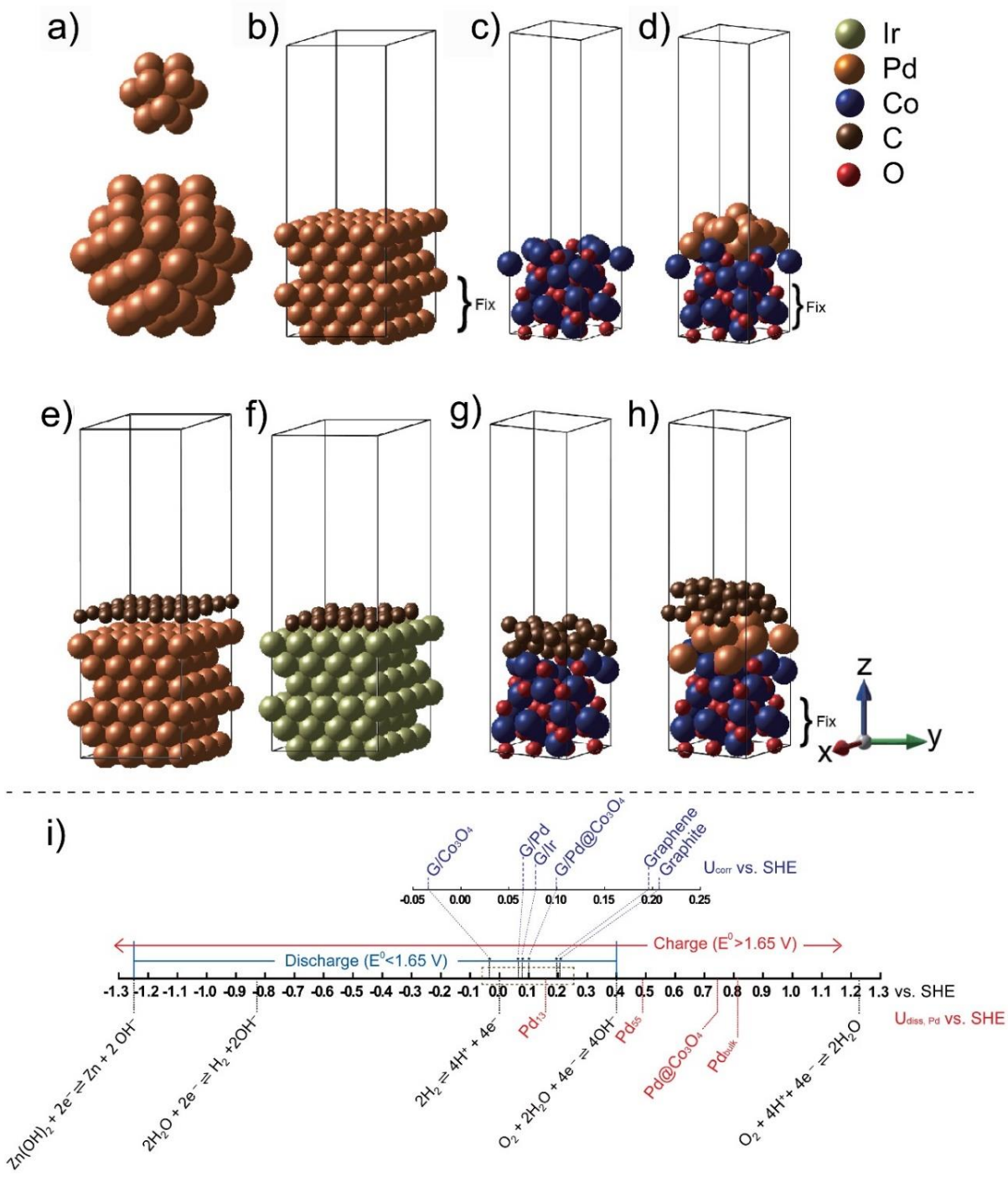

Figure 5-13. Considered DFT models and schematic equilibrium potentials in Zn-air cell denoting the $U_{diss,Pd}$ and $U_{corr;C}$ of Pd, and carbon. a) Relaxed Pd_{13} and Pd_{55} nanoparticles, and slab models of (b) Pd (111) (c) Co_3O_4 (001) and (d) Pd monolayer deposited on Co_3O_4 (001), and the designed models of graphene deposited on (e) Pd, (f) Ir, (g) Co_3O_4 (001) and (h) Pd@Co_3O_4 (001) after structural relaxation. (i) Potential window illustrating relevant electrochemical reactions and dissolution potentials of carbon and Pd.

To understand the fundamental mechanisms behind the high electrochemical stability of Pd@3DOM-Co_3O_4, two basic chemical reactions were considered for employing *ab-initio* calculations, as shown in the following equations (Eq. 5-1 and 5-2):

$$Pd \leftrightarrow Pd^{2+}{}_{,aq} - 2e^- \tag{5-1}$$

$$C_s + 2H_2O_{,aq} \leftrightarrow CO_{2,g} + 4H^+ + 4e^- \tag{5-2}$$

Pd_{13} and Pd_{55} nanoparticles (**Figure 5-13a**) and slab models of Pd (111) (**Figure 5-13b**), Co_3O_4 (001) (**Figure 5-13c**) and Pd monolayer deposited on Co_3O_4 (001) (**Figure 5-13d**) were designed to investigate the Pd dissolution potential ($U_{diss,Pd}$) as a descriptor for thermodynamic stability. The $U_{diss,Pd}$ considers the outermost M shell of the Pd nanoparticle and the Pd monolayer on Co_3O_4, as given by the following chemical equations (**Eq. 5-3** and **5-4**, respectively):

$$Pd_n \leftrightarrow Pd_{n-m} + mPd^{2+}(aq) + 2me^- \tag{5-3}$$

$$Pd_m @(Co_3O_4)_l \leftrightarrow mPd^{2+}(aq) + 2me^- + (Co_3O_4)_l \tag{5-4}$$

The standard Gibbs energy of reaction for the dissolution of the Pd particle and the Pd monolayer on Co_3O_4 can be expressed as follows (**Eq. 5-5** and **5-6**, respectively):

$$\begin{aligned}\Delta G^\circ = {} & \mu^\circ(Pd_{n-m}) + m\{\mu^\circ(Pd^{2+}{}_{,aq}) + kT\ln(a_{Pd^{2+}})\} - 2m\left(\mu^\circ{}_e - e\Delta U_{diss,Pd}\right) \\ & -\{\mu^\circ(Pd_{n,s}) + kT\ln(a_{Pd_n})\}\end{aligned} \tag{5-5}$$

$$\Delta G^{\circ} = \mu^{\circ}(Pd_{n-m}) + m\{\mu^{\circ}(Pd^{2+}, aq) + kT\ln(a_{Pd^{2+}})\} \\ -2me\left(\mu^{\circ}_{e} - e\Delta U_{diss,Pd}\right) + \{\mu^{\circ}(Co_3O_4)_l + kT\ln(a_{(Co_3O_4)_l})\} \\ -\{\mu^{\circ}(Pd_n@(Co_3O_4)_l) + kT\ln(a_{Pd_n@(Co_3O_4)_l})\} \quad \textbf{(5-6)}$$

Where μ^{o} is the standard chemical potential, k is the Boltzmann constant, a is the activity coefficient, and T is the temperature. Then, the $U_{diss,Pd}$ was derived based on free energy via the following equations (**Eq. 5-7** and **5-8**):

$$U_{diss,Pd} = U_{bulk} + \frac{1}{2me}\{mE(Pd_{bulk}) + E(Pd_{n-m}) - E(Pd_n)\} \quad \textbf{(5-7)}$$

$$U_{diss,Pd} = U_{bulk} + \frac{1}{2ne}\{E(Pd_n) + E((Co_3O_4)_l) - E(Pd_n@(Co_3O_4)_l)\} \quad \textbf{(5-8)}$$

The dissolution potentials of various forms of Pd are arranged in **Figure 5-13i**. The reaction potentials shown in **Figure 5-13i** are calculated based on the standard hydrogen electrode (SHE) to show all of the reactions that are relevant to the operation of a rechargeable Zn-air battery on a single potential scale. The calculated U_{bulk} of Pd slab model (bulk surface, **Figure 5-13b**) of 0.81 V vs. SHE is found to be lower than U_{diss} of Pt (1.01 V vs. SHE). The U_{diss} of Pd_{13} and Pd_{55} nanoparticles (**Figure 5-13a**) in DFT design are determined to be 0.16 and 0.49 V vs. SHE, respectively. The larger Pd_{55} particle resulted in higher dissolution potential, indicating higher electrochemical stability, as supported in previous reports.[134, 159] In the Zn-air battery chemistry, the oxygen reduction potential at the air electrode is 0.4 V vs. SHE, which means the smaller sized Pd_{13} nanoparticle with a diameter of 0.5 nm is thermodynamically unstable. Although the Pd_{55} nanoparticle with a diameter of 1.1 nm maintains its solid phase with relatively higher thermodynamic stability within the potential range, it is likely to dissolve at potentials above 0.49 V vs. SHE during charging of the Zn-air battery ($E^{\circ} > 1.65$ V and $E_{(air}$

$_{electrode)}$ > 0.4 V). Interestingly, in contrast, the $U_{diss,Pd}$ of Pd monolayer on Co_3O_4 (**Figure 5-13d**) is comparable to the $U_{diss,Pd}$ of Pd bulk, which means the catalyst is likely to maintain its solid phase if the cathode potential of the battery can be maintained below 0.74 V vs. SHE. This computational prediction of a relatively high $U_{diss,Pd}$ of Pd on 3DOM-Co_3O_4 is consistent with the experimentally observed extreme durability of Pd@3DOM-Co_3O_4 in the half-cell evaluation discussed earlier.

High surface area carbon materials are commonly used as catalyst supports to provide efficient pathways for electron transfer and facilitate reactant flux, as well as to disperse nano-sized catalyst particles that tend to agglomerate due to high surface energies.[160] Particularly for oxide materials such as Co_3O_4 that have intrinsically lower electrical conductivity than metals, they are usually combined with carbon materials to utilize their ORR/OER catalytic properties more effectively.[62, 71] In the rechargeable Zn-air battery testing conducted in this study, Pd@3DOM-Co_3O_4 was dispersed on a microporous layer made of carbon GDL, which acts as a conductive and porous support. Therefore, it is essential to understand the electrochemical corrosion mechanism of the carbon support since it has a direct influence on the cycle life of the battery. Accordingly, to simulate stability of the carbon material supporting various catalysts, a carbon monolayer (e.g., graphene) was designed on Pd (111), Ir(111), Co_3O_4 (001), and Pd@Co_3O_4 (001) as shown in **Figure 5-13e-h** (initial models in **Figure 5-11**).

The calculation of the equilibrium potential for carbon corrosion ($U_{corr,C}$) starts with **Eq. 5-9** shown below, which represents the reaction of carbon oxidation on the supported catalysts.

$$C_p / Supp. + 2H_2O_{,aq} \leftrightarrow pCO_{2,g} + Supp. + 4pH^+ + 4pe^- \quad \textbf{(5-9)}$$

The $U_{corr,C}$ on graphene can be obtained via calculating the change in the standard Gibbs free

energy (ΔG°) as described in **Eq. 5-10** below.

$$\begin{aligned}\Delta G^{\circ} = & p(\mu^{\circ}_{CO_2,g} + kT\ln a_{CO_2}) + (\mu^{\circ}_{Supp.,s} + kT\ln a_{Supp.,s}) \\ & +4p(\mu^{\circ}_{H^+,aq} + kT\ln a_{H^+}) + 4p\left(\mu^{\circ}_{e} - e\Delta U_{corr,C}\right) \\ & -(\mu^{\circ}_{C_p/Supp.,s} + kT\ln a_{C_p/Supp.,s}) - 2p(\mu^{\circ}_{H_2O,aq} + kT\ln a_{H_2O,aq})\end{aligned} \quad \textbf{(5-10)}$$

Lastly, the $U_{corr,C}$ was derived based on the free energy above (Eq. 10) as presented in the following equation (**Eq. 5-11**);

$$U_{corr,C} = \frac{1}{4pe}(E_{C_p/Supp.,s} + 2pE_{H_2O,aq} - pE_{CO_2,g} - E_{Supp.,s} - 2pE_{H_{2,g}} - 4p\times 0.059\,pH) \quad \textbf{(5-11)}$$

where the support (Supp.) is Pd, Ir, Co_3O_4, or Pd@Co_3O_4 in each case. Graphite is oxidized at potentials over 0.207 V vs. RHE, which is the standard potential for the electrochemical oxidation of carbon in aqueous electrolyte.[161] The $U_{corr,C}$ of a graphene monolayer was evaluated to be 0.196 V, which is slightly lower than graphite designed by the DFT model, as exhibited in **Figure 5-12**. Interestingly, $U_{corr,C}$ is significantly decreased when carbon is deposited on noble metals and metal oxides, with values of 0.065, 0.078V, and −0.034 V vs. SHE on Pd, Ir, and Co_3O_4 surfaces, respectively. Pd/C has a very low electrochemical stability and demonstrated severe degradation during exposure to high OER potentials as shown in **Figure 5-6a-d** (Pt/C shows a similar result in **Figure 5-6a** and **5-6c**, and **5-7b**), which is attributed to the fact that the dissolution of carbon accelerates the agglomeration and loss of Pt and Pd nanoparticles. Accordingly, their low $U_{corr,C}$ likely led to the catalyst deactivation only after 100 OER cycles, resulting in significant negative shifted $E_{1/2}$ by 214 mV and 257 mV, respectively (refer to **Table 5-1**). Similarly, Ir/C shows severe degradation having $E_{1/2}$ negatively shifted by 128 mV after ADT, although the degree of degradation is less than Pt and Pd. The

degradation of Ir/C observed experimentally is most likely due to the dissolution of Ir as well as carbon corrosion. Meanwhile, despite the lower $U_{corr,C}$, 3DOM-Co_3O_4 demonstrates much greater OER durability than carbon-supported noble metals in the experiment, which is due to its stability in alkaline media within the OER potential range.[162] In the case of Pd@3DOM-Co_3O_4, however, it is revealed that the $U_{corr,C}$ of the carbon monolayer on Pd@3DOM-Co_3O_4 is significantly increased with a value of 0.1 V vs. SHE, which predicts a much-inhibited rate of carbon corrosion. This is consistent with the experimentally observed excellent stability of Pd@3DOM-Co_3O_4, having only slightly shifted to the final E_{OER} of 1.67 V after ADT from the initial performance of 1.61 V. More notably, as determined previously, the OER current retention of Pd@3DOM-Co_3O_4 after 1,000 OER cycles was 96.4 %, whereas 3DOM-Co_3O_4 itself and Ir/C only retained 71.8 % and 30.8 % of the initial activity, respectively.

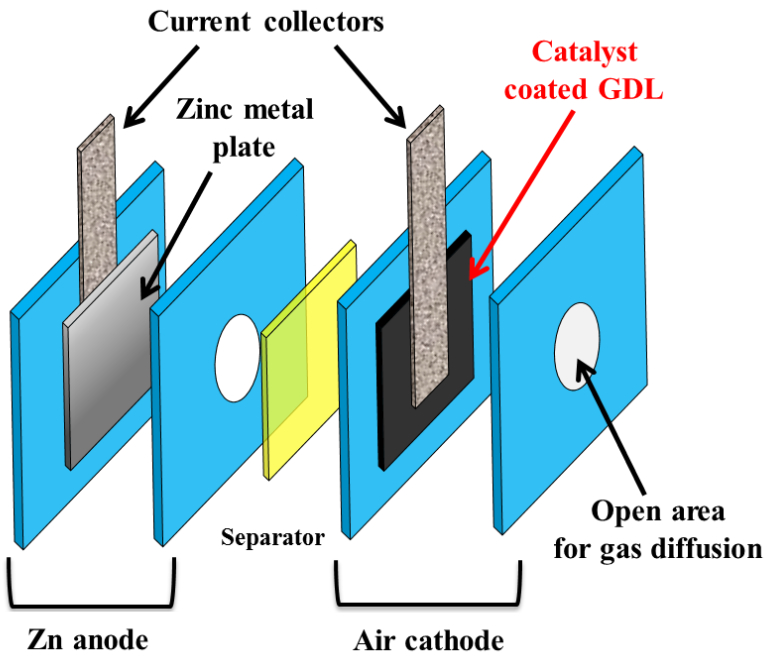

Figure 5-14. Schematic image of prototype Zn-air battery

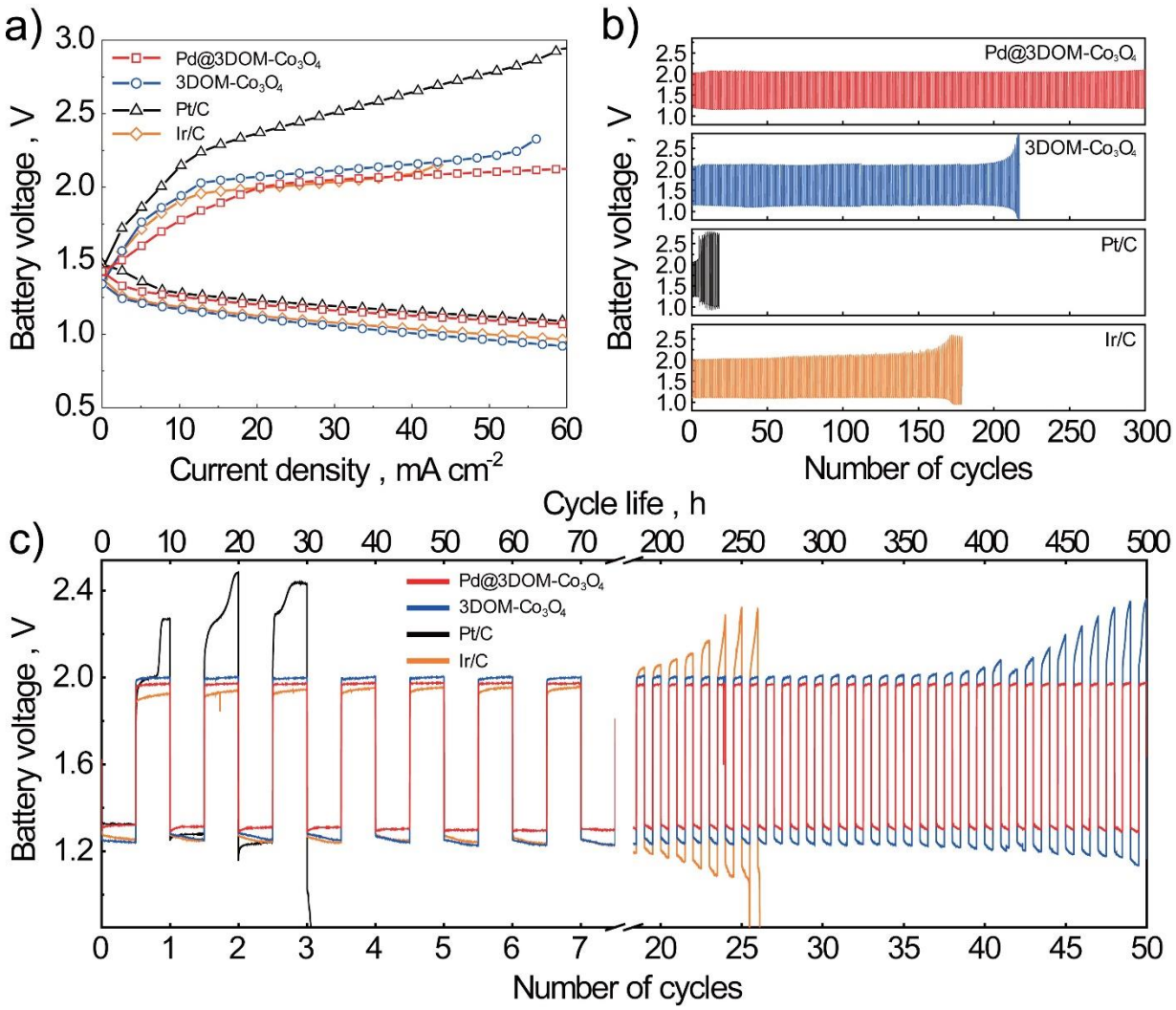

Figure 5-15. Rechargeable Zn-air batteries with Pd@3DOM-Co_3O_4 catalyst at the air electrode. a) Charge and discharge (C/D) polarization curves of the rechargeable Zn-air battery obtained at applied current densities; (b) C/D cycling performance of the rechargeable Zn–air battery using Pd@3DOM-Co_3O_4, 3DOM-Co_3O_4, Pt/C and Ir/C obtained with a 10 min cycle period and applied current density of 10 mA cm^{-2}. (c) Long term C/D cycling performance of the electrocatalysts obtained with 10 hour cycle period at 1 mA cm^{-2}. The DC profile experiments were terminated above 2.5 V or below 0.5 V.

In addition to half-cell testing, Pd@3DOM-Co_3O_4 was tested as a bifunctional catalyst in an electrically rechargeable Zn-air battery prototype (**Figure 5-14**). **Figure 5-15** shows the charge and discharge polarization curves of various electrocatalysts. Although the open-circuit voltage (OCV) for Pd@3DOM-Co_3O_4 (1.43 V) is slightly lower than that for Pt/C (1.46 V), the

discharge potential is highly competitive to that of Pt/C particularly at higher current densities. In contrast, 3DOM-Co_3O_4 and Ir/C demonstrate relatively lower discharge potentials and more significant loss of activity at high current densities, resulting in larger overpotentials and lower efficiency. During charging, Pd@3DOM-Co_3O_4 shows comparable charge potential to that of Ir/C, while the overpotential of Pd@3DOM-Co_3O_4 is much lower than that of Ir/C in the low current density region. Taken together, Pd@3DOM-Co_3O_4 demonstrates enhanced bifunctional electrocatalytic activity with the least overpotential over the extensive range of applied charge and discharge current densities, which is consistent with the trends observed from both ORR and OER half-cell evaluations (**Table 5-1**). As shown in **Figure 5-15b**, the electrically rechargeable Zn-air battery with Pd@3DOM-Co_3O_4 exhibits great rechargeability as well as synergistically improved activity, where the catalyst demonstrates far lower initial overpotential (0.84 V at 10 mA cm^{-2}) between discharge and charge potentials than those with Pt/C (0.89 V), Ir/C (0.86 V) and Co_3O_4 (1.0 V). The battery reliably operated for 300 charge/discharge cycles over a period of 50 h (10 min per a charge/discharge cycle) while effectively retaining its initial performance, which is significantly higher than 3DOM-Co_3O_4 (210 cycles), Pt/C (6 cycles), and Ir/C (170 cycles). Moreover, a more extensive cycling test was conducted with one charge/discharge cycle lasting 10 h to explore the long term durability of Pd@3DOM-Co_3O_4, with results shown in **Figure 5-15c**. As expected, Pd@3DOM-Co_3O_4 demonstrated not only the least overpotential (0.66 V at 1 mA cm^{-2}) but also the most extended cycle life without severe performance loss over 500 h, indicating its enhancements in terms of both electrocatalytic activity and stability. 3DOM-Co_3O_4 itself showed a moderate cycle life, with considerable performance loss starting at the 40^{th} cycle and drastically increased overpotentials thereafter, resulting in significant degradation of charge and discharge performances. Meanwhile, the precious-metal benchmark

catalyst Pt/C lost its stable discharge and charge activities within the first cycle, indicating its instability in the high potential range during the charging process of the battery, whereas the performance of Ir/C degraded relatively slowly, terminating after 26 cycles of battery operation. The excellent rechargeability and extended cycle life observed with Pd@3DOM-Co_3O_4 are most likely due to three main improvements: (i) a decrease in the d-band center of Pd (-1.98 eV) and the enhanced electron abundance at the Fermi level achieved by chemical deposition of Pd, which promotes increased kinetics of oxygen reactions and facilitates faster charge transfer, respectively, resulting in improved electrocatalytic activity and electrical conductivity, (ii) relatively higher carbon corrosion potential for Pd@3DOM-Co_3O_4 ($U_{corr,C}$ = 0.1 V vs. SHE), resulting in less corroded surfaces and (iii) the increase in dissolution potential of Pd deposits within Pd@3DOM-Co_3O_4 ($U_{diss,Pd}$ = 0.74 V vs. SHE), leading to both a thermodynamically and electrochemically stable catalyst even at high charging potentials within the Zn-air battery.

5.4 Summary

The bifunctional ORR and OER activities and electrochemical stability observed with a unique three-dimensionally ordered mesoporous Pd@3DOM-Co_3O_4 catalyst were elucidated by electrochemical testing and *ab-initio* computational calculation (DFT). Experimentally, both ORR and OER activities were observed to benefit from synergistically combining chemically deposited Pd and 3DOM-Co_3O_4, resulting in activities higher than those of the individual components. Specifically, Pd@3DOM-Co_3O_4 showed a comparable half-wave potential ($E_{1/2}$) of 0.881 V to that of the precious metal benchmark Pt/C (0.898 V) during ORR and significantly higher current density (41.3 mA cm^{-2} at 2.0 V vs. RHE) and lower overpotential (0.38 V) compared to the precious metal benchmark Ir/C (40.6 mA cm^{-2} and 0.34 V) during OER. Both

computational and physicochemical investigations were utilized to elucidate high bifunctional activities demonstrated by Pd@3DOM-Co_3O_4. Not only did the modified electronic structure of Pd on 3DOM-Co_3O_4 result in a downward shift in ε_d of Pd that weakens the bond with oxygen, resulting in increased ORR kinetics, but it also increased Co^{3+} active sites in Co_3O_4 after Pd deposition leading to improvements in the OER activity. Additionally, electron abundance at the Fermi level in the DOS of Co in Pd@3DOM-Co_3O_4 enhances its electrical conductivity, promoting a rapid charge transfer during both oxygen reactions. Besides the enhanced bifunctional oxygen electrocatalysis, Pd@3DOM-Co_3O_4 shows remarkable electrochemical stability in the severely oxidative potential range of OER. After 1000 cycles of accelerated degradation testing, Pd@3DOM-Co_3O_4 demonstrated very high retentions of 99.5 % and 84.6 % of its initial half-wave potential and specific kinetic current, respectively, compared to those of Pt/C (71.7 % and 7.2 %) and Pd/C (73.5 % and 7.5 %). Moreover, while 3DOM-Co_3O_4 without Pd and Ir/C showed high losses in their OER activity displaying 71.8 % and 30.8 % OER current retention, respectively, excellent OER stability was observed with Pd@3DOM-Co_3O_4 showing 96.4% OER current retention. The superior experimentally-observed electrochemical durability was corroborated by DFT computational investigations of the bulk-like dissolution potential of Pd on 3DOM-Co_3O_4 and the high corrosion potential of carbon on Pd@3DOM-Co_3O_4. The remarkable electrochemical activities and stabilities of Pd@3DOM-Co_3O_4 resulted in excellent rechargeability of a prototype Zn-air battery, which demonstrates the attractiveness of the computationally-aided catalyst design demonstrated in this work.

6. Metal-Organic-Framework (MOF) derived Hierarchically Porous Nanocuboids as an Efficient Electrocatalyst for Oxygen Evolution Reaction

This chapter is reprinted in adapted form from the below article[163] with permission from Wiley.

Park, M. G., W. Ahn, D. U. Lee, M. H. Seo, G. Jiang, Z. P. Cano, F. M. Hassan, Z. Chen, "Hollow Multivoid Nanocuboids Derived from Ternary Ni–Co–Fe Prussian Blue Analog for Dual-Electrocatalysis of Oxygen and Hydrogen Evolution Reactions", *Advanced Functional Materials*, 28 (2018) 1802129.

6.1 Introduction and Motivation

Rapidly increasing international development of renewable and green energy sources has drawn widespread attention of researchers to water-splitting oxygen and hydrogen production via the electrochemical oxygen evolution reaction (OER) and hydrogen evolution reaction (HER), respectively.[21, 164, 165] To enhance these reactions to commercially viable rates, however, high-performance electrocatalysts are required to overcome the activation energies associated with OER and HER.[166-170] Platinum (Pt) and iridium (Ir) based materials are currently known to exhibit the highest HER and OER activities, respectively; however, their scarcity and lack of stability have made them difficult to be introduced in large-scale energy conversion and storage applications. Therefore, the development of non-noble transition metal-based active catalysts with tunable structures and compositions is currently a significant energy research focal point for the global implementation of clean and efficient water-splitting technologies. Recently, catalysts derived from metal-organic frameworks (MOFs), typically synthesized using precursors consisting of transition metals and organic linkers, have emerged as promising active and

inexpensive electrocatalysts due to their intrinsic advantages of high porosity, three-dimensional structures, and compositional flexibility. In particular, MOFs with organic ligands containing carbon, nitrogen, and sulfur atoms coordinated to transition metal centers have been reported to form three dimensional and uniformly porous structures, resulting in considerably increased active surface area and enhanced physical properties. These MOFs, often composed of transition metal atoms such as nickel, cobalt, and iron, and heteroatoms such as nitrogen, sulfur, and phosphorus are characterized by strong interactions between them, which can serve as electrocatalytically active sites for HER and OER. [59, 81, 171-177]

The advantages of MOF-derived active materials in advanced energy conversion and storage applications have been recently applied to efficient electrocatalysts for fuel cells, metal-air batteries, and electrolyzers.[62, 65, 168, 176-187] For example, Gadipelli et al. recently reported a design route for the synthesis of MOF-derived electrocatalysts, in which zeolitic imidazolate framework (ZIF) was used as the template.[188] The resulting MOF catalyst containing active Co-N-C species demonstrated efficient ORR and OER activities. Yu et al. reported an active OER electrocatalyst based on porous carbon-coated nickel phosphides (NiP) prepared using Ni-based Prussian blue analogue (PBA) nanoplates as a template.[189] The structural advantages of MOFs allowed the NiP catalyst to demonstrate superior electrocatalytic activity towards OER compared to NiO and $Ni(OH)_2$ counterparts. Despite these electrocatalyst developments, however, bifunctional MOF-derived electrocatalysts active towards both HER and OER for water-splitting applications have rarely been reported to the best of our knowledge.

In this study, we introduce novel MOF-containing Ni-Co-Fe transition metal centers (denoted NCF-MOF) as a dual-function water-splitting catalyst for enhancing HER and OER activities. The morphology of the catalyst is revealed to exhibit a nano-cuboid structure with

multiple meso- and micro-sized pores prepared via a facile synthesis procedure. Transition metal-based PBA nanocubes with a chemical formula $M_x^{II}[M_y^{III}(CN)_6]_z \cdot H_2O$, where M^{II} and M^{III} are divalent and trivalent transition metal cations, respectively, were selected as MOF precursors to obtain unique compositions and multi-hollow nano-cuboid structures.[173, 190] Specifically, PBA nanocube precursors containing nickel, cobalt, and iron were utilized to maintain the general nano-cuboidal structure, while optimizing the composition of transition metal centers for efficient OER and HER activities. This makes NCF-MOF one of the most promising non-precious electrocatalysts for water-splitting applications due to several material advantages including (i) significantly extended active surface area with high porosity and robust structure, (ii) active nitrogen species formed during facile synthesis, and (iii) favorably tuned electronic structure by combining active transition metals having different number of outer electrons.

These main electrocatalytic contributors that affect OER and HER were successfully obtained through careful selection of PBA precursors and the facile synthesis procedure. Furthermore, the NCF-MOF catalyst exhibited excellent electrochemical stability, which is attributed to its highly uniform and rigid porous nano-cuboidal structure that allows rapid charge transfer and mass transport of active species to be maintained. The dual-function of the catalyst and its stability was confirmed by three-electrode half-cell evaluations and moreover was integrated onto nickel-foam supports for practical demonstrations of efficient and stable water-splitting electrodes.

6.2 Experimental Methods

6.2.1 Synthesis of MOF Precursor and MOF-based Electrocatalysts

The simple preparation procedure of metal-organic framework (MOF) electrocatalysts is presented in Scheme 1. The Prussian blue analogue (PBA) nanocubes, which were utilized as precursors, were synthesized by the co-precipitation method, where the precursors included Ni and Co (NC-PBA), Ni and Fe (NF-PBA), or Ni, Fe, and Co (NCF-PBA) ions. For the first precursor, 0.6 mmol of nickel nitrate and 0.9 mmol of sodium citrate were first dissolved in 20 ml of DI water. Next, 0.4 mmol of potassium hexacyanoferrate (III) was dissolved in another 20 ml of DI water. The two solutions were then mixed, and vigorous stirring was conducted for 12 hours to synthesize the NF-PBA precursor with uniformly distributed particle sizes. The NC-PBA and NCF-PBA precursors were synthesized by the same method, except for the use of 0.4 mmol potassium hexacyanocobaltate (III) solution for NC-PBA, and a mixed solution of 0.2 mmol potassium hexacyanocobaltate (III) and 0.2 mmol potassium hexacyanoferrate (III) for NCF-PBA. It is well known that the citrate ions prohibit the precipitation reaction from forming large-sized particles. Therefore, sufficient reaction time was required to prepare uniformly distributed precursors with small-sized particles.[189] The MOFs were obtained from the as-prepared PBA precursors through a simple hydrothermal reaction with the addition of sodium sulfide (Na_2S). 100 mg of PBA precursor and 200 mg of Na_2S were mixed in 100 ml of ethanol and transferred into a Teflon liner and stainless-steel autoclave. The hydrothermal reaction was carried out at 100 ^oC for 6 hours to induce sufficient ion exchange. Then, the intermediate product was washed, dried, ground, and heat-treated at 300 ^oC in Ar atmosphere for 3 hours to form highly crystalline MOFs. The black recrystallized MOFs were pulverized and dried in a

vacuum oven at 70 ^{o}C for 12 hours. The final MOF products containing Ni/Co, Ni/Fe, and Ni/Co/Fe centers were denoted NC-MOF, NF-MOF, and NCF-MOF, respectively.

6.2.2 Rotating Disk Electrode (RDE) Tests

A traditional half-cell system with three electrodes was utilized to explore the electrochemical activities of the MOF catalysts, where the three electrodes were a glassy carbon electrode (GCE), a saturated calomel electrode (SCE), and a platinum wire used as the working electrode, reference electrode, and counter electrode, respectively. The electrocatalytic activity towards the oxygen evolution reaction (OER) and hydrogen evolution reaction (HER) was evaluated using catalyst-loaded NFEs or via the rotating disc electrode (RDE) technique using catalyst-coated GCEs. A CHI Electrochemical Station (Model 760D) was used for all electrochemical evaluations. The measurements were conducted from 0.20 V to 0.85 V vs. SCE at 1600 rpm of rotation speed for OER, and from -0.9 V to -1.5 V vs. SCE at 1600 rpm of rotation speed for HER, with a scan rate of 10 mV s^{-1}. Pure nitrogen gas was purged for 30 min before OER, and HER evaluations, and all measurements were performed in a 0.1 M KOH solution. All measured potentials were adjusted to the reversible hydrogen electrode (RHE) scale, according to the equation; $E_{RHE} = E_{SCE} + 0.241 + 0.059pH$. Prior to electrochemical testing, the GCE (diameter: 5 mm) was polished using alumina suspension (size: 0.05 μm) on a smooth polishing cloth to obtain a uniform and smooth GCE surface, and then the polished GCE surface was ultra-sonicated in DDI water for a few seconds to remove any leftover alumina particles. The catalyst ink was prepared by combining 2 mg catalyst and 2 mg Vulcan Carbon (XC-72, VC) in 1.0 mL of pre-treated Nafion solution (mixture of 10 mL IPA and 80 μL of 5 wt% Nafion, Ion Power), followed by ultrasonication for 60 min to obtain a homogeneous suspension. 20 μL of

the as-prepared ink was dropped onto the GCE surface and dried in room temperature, achieving a loading of 0.2 mg $cm^{-2}_{catalyst}$. Meanwhile, precious metal catalysts consisting of platinum on carbon (Pt/C, 28.8 wt. % Pt) and iridium on carbon (Ir/C, 20 wt. % Ir) were utilized as benchmark catalysts to compare the electrocatalytic performances and practical efficiency of the MOF catalysts.

6.2.3 Practical Nickel Foam Electrode Tests

The catalysts were also loaded onto nickel foam electrodes (NFEs) and tested using the same three-electrode configuration described above, using the NFE as the working electrode. Prior to testing catalyst-loaded NFEs, a piece of nickel foam was cut into a 1 cm × 2 cm size and washed in 2.0 M HCl via ultra-sonication for 1 hour to remove any oxidized nickel, followed by washing ultra-sonically in acetone for 1 hour to remove organic impurities on its surface. The catalyst ink was prepared by mixing 0.5 mg catalyst and 0.5 mg VC in a 1.0 mL pre-treated Nafion solution (a mixture of 10 mL IPA and 80 uL of 5 wt% Nafion, Ion Power) followed by ultrasonication for 60 min to obtain a homogeneous ink mixture. Then, the mixture was drop-casted onto the dried NFE (active area: 1 cm^2), achieving the loading of 0.5 mg $cm^{-2}_{catalyst}$. The cycling was typically conducted at 50 mV s^{-1} scan rate in N_2-saturated electrolyte until the CV curve showed stable currents indicating a stable solid/liquid interface.

6.2.4 Electrochemical Stability Tests

Chronopotentiometry (CP) evaluation was also carried out to verify the practical stabilities of the MOF catalysts. First, catalyst-coated GCE was activated by cyclic voltammetry

(~40 cycles) in a nitrogen-saturated electrolyte. Then, CP testing was conducted at constant current densities, where 20 mA cm^{-2} and -20 mA cm^{-2} were applied to achieve sufficient OER and HER potentials, respectively. In terms of measuring the electrochemical performances, OER and HER overpotentials of catalyst-coated GCEs were measured at 10 mA cm^{-2} and -10 mA cm^{-2}, respectively, and OER and HER overpotentials of catalyst-loaded NFEs were measured at 30 mA cm^{-2} and -30 mA cm^{-2}, respectively. For easier comparison of the OER and HER overpotentials, 1.23 V vs. RHE (equilibrium potential for splitting water) and 0 V vs. RHE were used as the standard potentials for OER and HER, respectively.

6.3 Results and Discussion

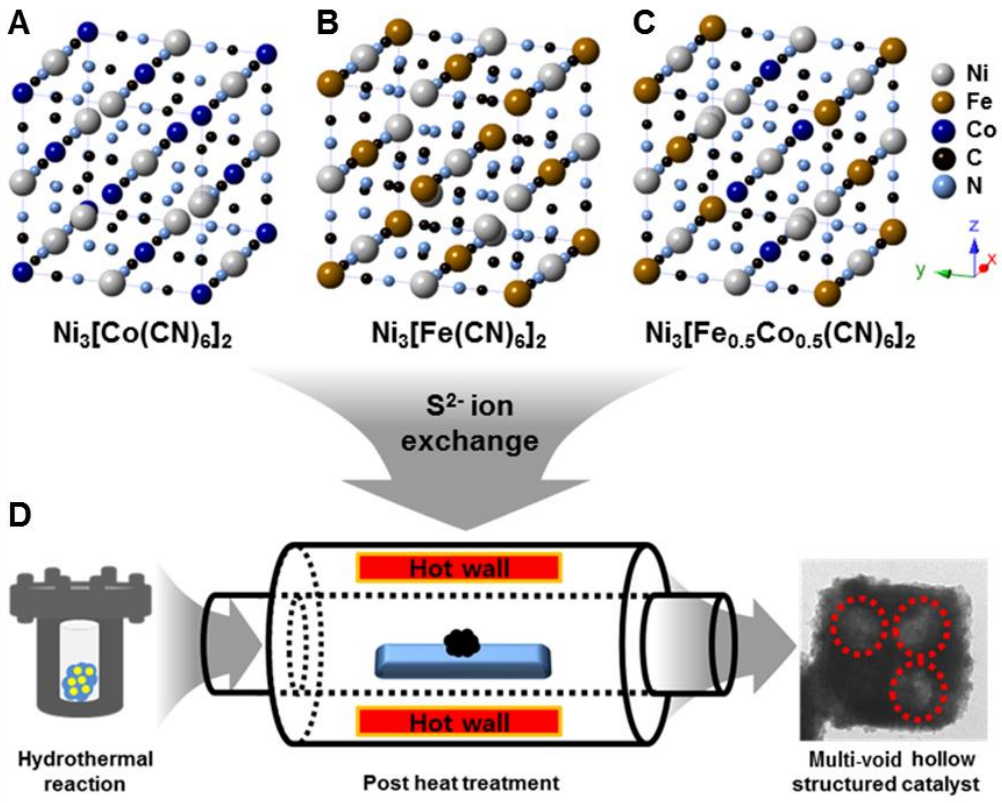

Figure 6-1. Schematic illustration of MOF electrocatalyst synthesis procedure using PBA nanocube precursors to form multi-void nano-cuboidal MOF.

A schematic illustration of the synthesis procedure of multi-void MOF nano-cuboid electrocatalysts using PBA nanocube precursors is presented in **Figure 6-1**. The PBA precursors are composed of transition metal ions (Ni, Fe and/or Co) and cyanide (CN) groups in the face-centered cubic (FCC) crystal packing arrangement.[191, 192] The PBA precursors used in this study consisted of different combinations of transition metal centers, namely Ni/Co (NC-PBA, **Figure 6-1A**), Ni/Fe (NF-PBA, **Figure 6-1B**), and Ni/Co/Fe (NCF-PBA, **Figure 6-1C**). These nanocube precursors were subjected to sulfur ion (S^{2-}) exchange and then crystallized via hydrothermal treatment followed by post-heat treatment (**Figure 6-1D**) to form highly crystalline multi-void nano-cuboids. This hierarchical hollow nano-cuboidal MOF structure is very interesting for electrocatalysis of OER and HER due to a possible increased number of active sites from the enlarged surface area. The exact morphology of the MOF catalysts, however, largely depends on the type of transition metal centers present in the PBA precursor. For example, NC-MOF (NC-PBA precursor shown in **Figure 6-2A** and **6-2B**) showed nano-cuboidal structures with an average size of 400 nm and relatively large pores on each face (**Figure 6-3A** and **6-3B**), while NF-MOF (NF-PBA precursor shown in **Figure 6-2C** and **6-2D**) showed uniformly sized cuboidal structures with an average size of 160 nm, maintaining the initial PBA precursor morphology (**Figure 6-3D** and **6-3E**). NCF-MOF (NCF-PBA precursor shown in **Figure 6-2E** and **6-2F**) exhibited general cuboid morphology with an average size of 180 nm and roughened surfaces (**Figure 6-3G** and **6-3H**).

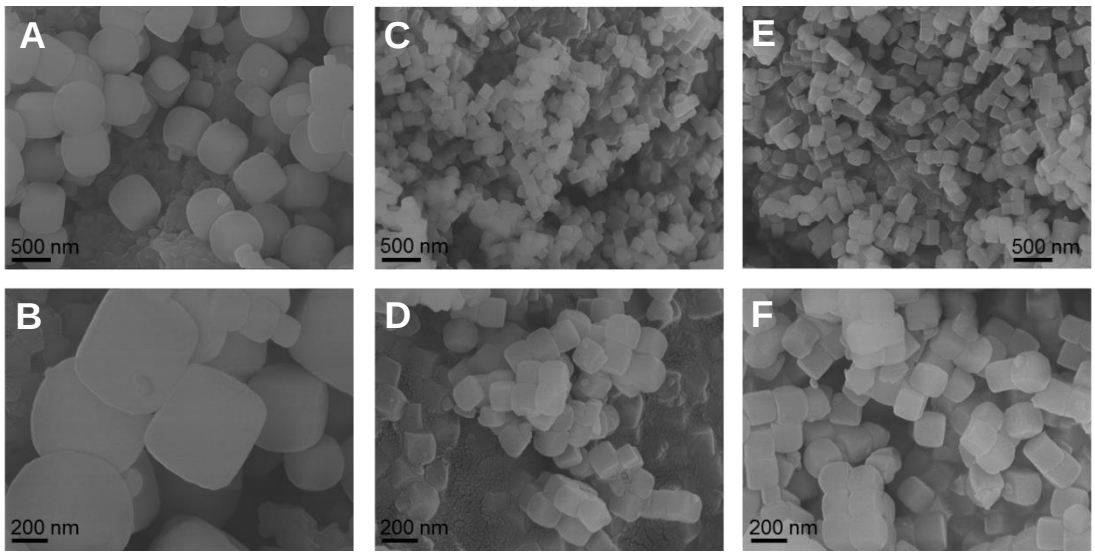

Figure 6-2. SEM images of (A and B) NC-PBA, (C and D) NF-PBA, and (E and F) NCF-PBA.

Interestingly, NF-PBA and NCF-PBA precursors were relatively smaller than NC-PBA, probably due to the presence of Fe ions. Moreover, the large pores observed in NC-MOF possibly formed during the hydrothermal processes due to very rapid ion exchanging between $[Co(CN)_6]^{3-}$ and S^{2-} ions, resulting in breakage of outer metal ions from the cuboid structures.[192] This led to the formation of NC-MOF with considerable shape change from the compact cuboid to porous structures. Unlike the significant morphological changes observed with NC-MOF from its precursor, NF-MOF and NCF-MOF largely maintained their nano-cuboidal structures. Only a slight morphology change observed with NF-MOF (roughening of its surface) was likely due to relatively lower ion exchanging power of $[Fe(CN)_6]^{3-}$ with S^{2-} anions (compared to that of $[Co(CN)_6]^{3-}$ in the case of NC-MOF), resulting in significantly less ion exchange and minimal morphological change. NCF-MOF is particularly interesting because of the presence of both $[Co(CN)_6]^{3-}$ and $[Fe(CN)_6]^{3-}$ having different ion exchanging rates which led to partial replacement with S^{2-} ions, resulting in an externally roughened surface, and internally having

multiple voids within a single nano-cuboid, which will be further discussed in the following section.

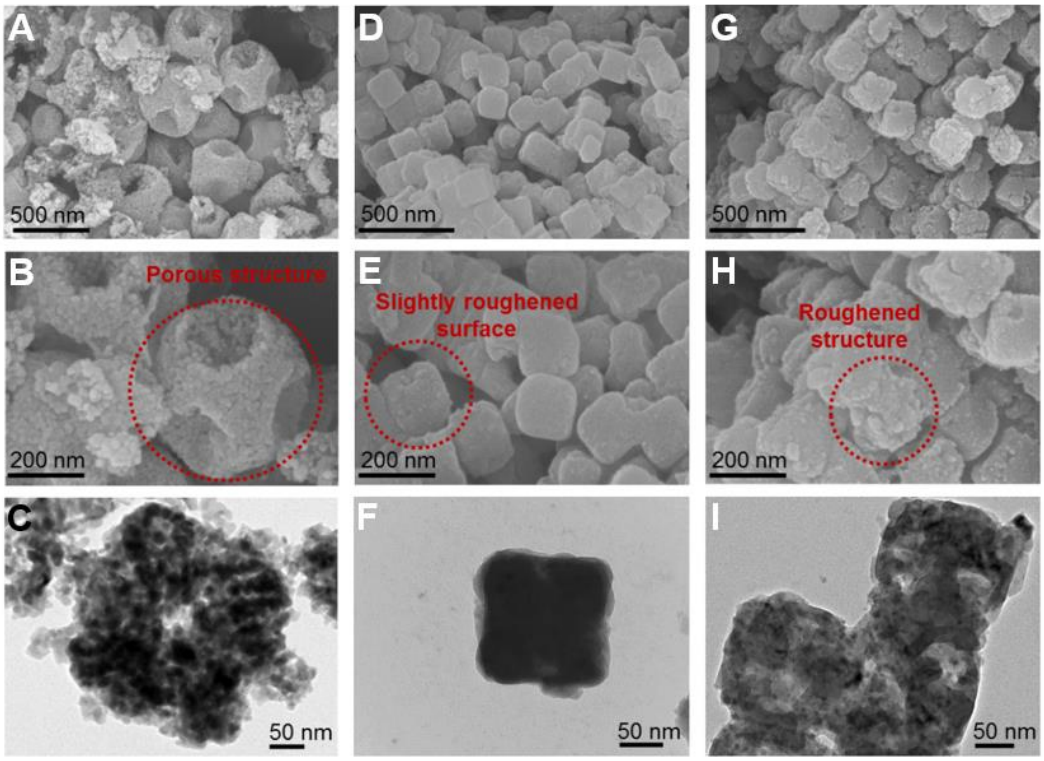

Figure 6-3. SEM (A, B, D, E, G, and H) and TEM (C, F, and I) images of various MOF morphologies. (A, B, and C) NC-MOF with large face-centered pores, (D, E, and F) NF-MOF nano-cuboids, and (G, H, and I) NCF-MOF nano-cuboids with a roughened surface.

TEM analysis was conducted to reveal the internal morphological features of the MOF catalysts. NC-MOF under TEM revealed that the large pores observed on all faces of the nano-cuboids were, in fact, interconnected, resulting in a hollow-core (**Figure 6-3C**). NF-MOF, on the other hand, maintained the non-porous nano-cuboidal structure from its precursor (**Figure 6-3F**), consistent with the SEM observations. TEM observations of NCF-MOF revealed spots within a single nano-cuboid with different brightness (**Figure 6-3I**), indicative of multiple void formations during the ion exchanging reaction.

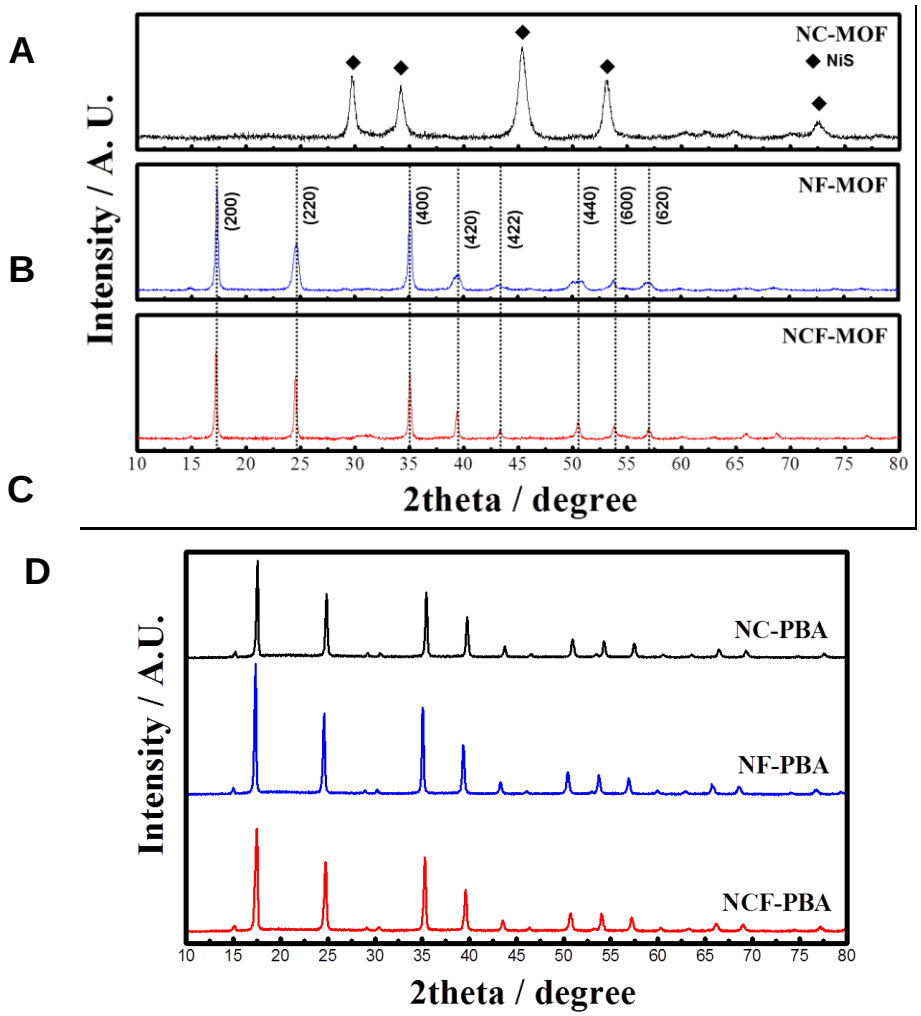

Figure 6-4. XRD patterns of (A) NC-MOF, (B) NF-MOF, and (C) NCF-MOF, and (D) NC-PBA, NF-PBA, and NCF-PBA. RD patterns of NF-MOF and NCF-MOF show peaks that closely match those of Prussian Blue Analogue (PBA) without any peaks due to impurities. In contrast, the pattern of NC-MOF matches with NiS, signifying near-complete ion exchanging of $[Co(CN)_6]^{3-}$ with S^{2-} ions.

These morphological differences again highlight different ion exchanging rates of each PBA precursor, and how they affect the final external and internal structures of the MOF catalysts. In terms of crystal structure, XRD characterization revealed that the pattern obtained from NC-MOF closely matches with that of NiS (JCPDS: 77-1624) (**Figure 6-4A**), indicative of near-complete exchange of $[Co(CN)_6]^{3-}$ with S^{2-} ions, as expected from the above microscopic analyses.[190] The obtained patterns of NF-MOF (**Figure 6-4B**) and NCF-MOF (**Figure 6-4C**), on

the other hand, matched the typical characteristic peaks of PBA, due to a relatively lower degree of $[Fe(CN)_6]^{3-}$ exchanged with S^{2-} anions, as conjectured based on morphological observations.[192] Scanning TEM (STEM) of a single NC-MOF nano-cuboid was used to obtain EDS line-scans through the mid-section (**Figure 6-5A**) and the edge (**Figure 6-5B**). The elements detected in the nano-cuboids, Ni, Co, Fe, C, N, and S, are indicated by different colors of the line-scan with the respective intensity corresponding to the amount of each element, which is separately plotted in **Figure 6-6**. The plots clearly show that the intensities of all detected elements are relatively higher at both ends of the plot compared to the center, which confirms the internally connected porous structure with a hollow core. From HRTEM images obtained from NC-MOF (**Figure 6-5C** and **6-5D**), selected area electron diffraction (SAED) patterns were also obtained at the center and the edge of the nano-cuboids, both of which reveal FCC lattice structures. In terms of composition, dark-field TEM (DFTEM) and elemental mapping were conducted to verify the compositional characteristics of NC-MOF, as presented in Figure S3E-J. The elemental maps indicate that NC-MOF is composed of nickel, nitrogen, sulfur, carbon, and residual cobalt, which clearly shows that most of the $[Co(CN)_6]^{3-}$ were in fact exchanged by S^{2-} ions, leading to the formation of NiS with hollow-core morphology. The intensity of each elemental map is in good agreement with the EDS line-scan measurements.

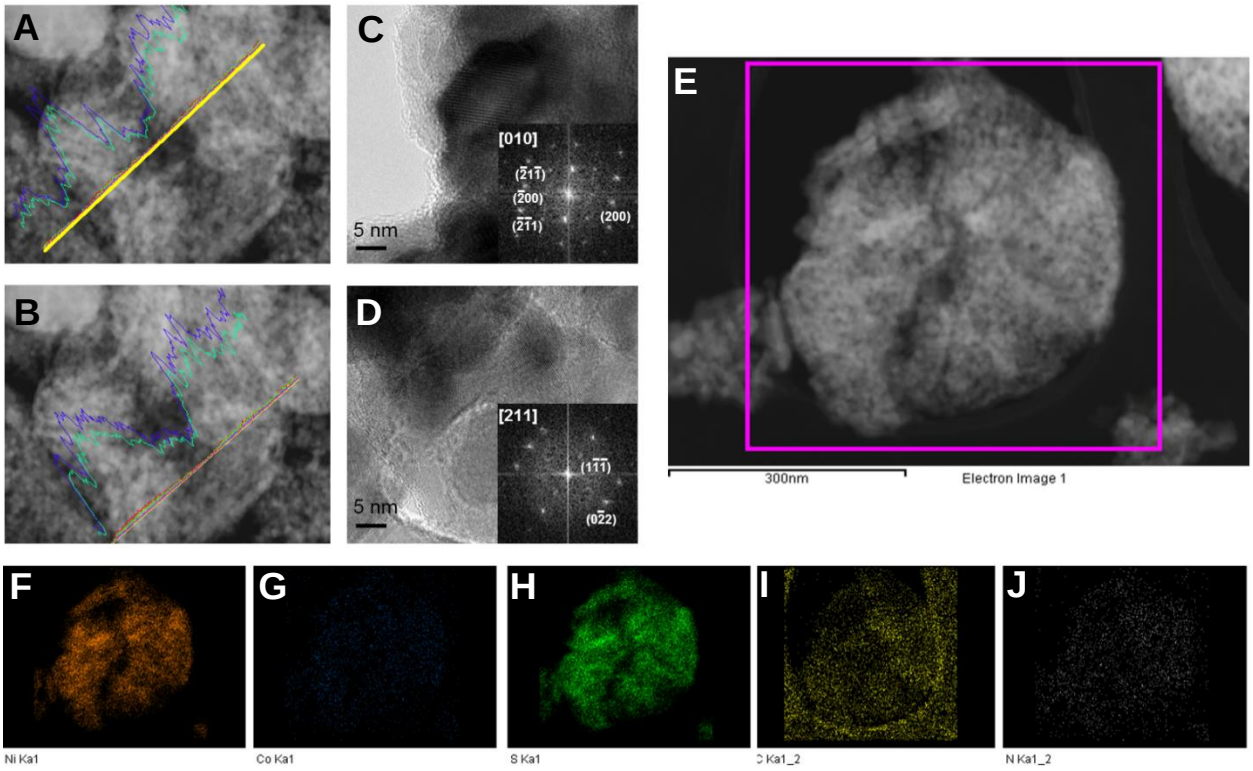

Figure 6-5. TEM analysis of NC-MOF. (A and B) STEM images with EDS line-scans obtained along the middle and edge of NC-MOF, (C and D) HRTEM images and SAED patterns obtained at the center and the edge of NC-MOF, (E) DFTEM image of NC-MOF, and the obtained elemental maps of (F) Ni, (G) Co, (H) S, (I) C, and (J) N, respectively.

Meanwhile, NF-MOF exhibited a much denser internal cuboidal core compared to that of NC-MOF, based on the STEM images shown in **Figure 6-7A** and **6-7B**, while SAED patterns obtained at the center (**Figure 6-7C**) and the edge (**Figure 6-7D**) of the nano-cuboid indicate a polycrystalline FCC structure. Based on both EDS line-scan (**Figure 6-7A**, **6-7B**, and **Figure 6-8**) and DFTEM elemental mapping (**Figure 6-7E-J**) results, relatively higher amounts of nickel and iron were detected within NF-MOF with lower amounts of carbon, sulfur, and nitrogen uniformly distributed along with both the center and edge parts. The low amount of sulfur detected is particularly important for verifying that the rate of ion exchange of $[Fe(CN)_6]^{3-}$ with S^{2-} ions was indeed slower than that of $[Co(CN)_6]^{3-}$ observed with NC-MOF. Interestingly,

higher amounts of nitrogen and carbon detected compared to NC-MOF is likely due to the decomposition of the cyanide groups in the PBA precursor during the heat-treatment process, which will be discussed in more detail later.

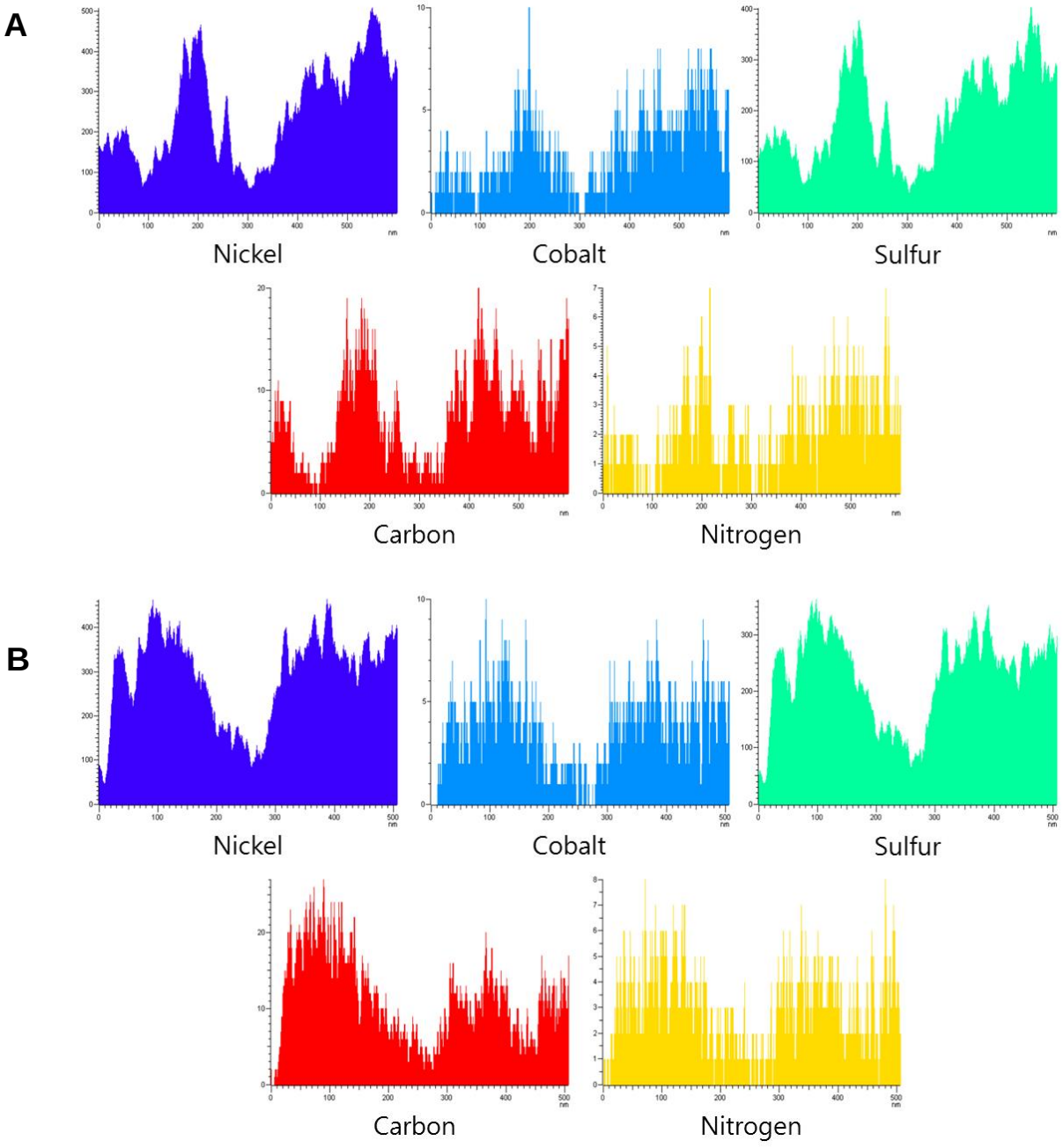

Figure 6-6. EDS line-scan results of NC-MOF along the (A) middle and (B) edge section of nano-cuboids: Ni and S are found to be distributed homogeneously, and most of $[Co(CN)_6]^{3-}$ anions are observed to be replaced by S^{2-} ions after the ion exchanging reaction.

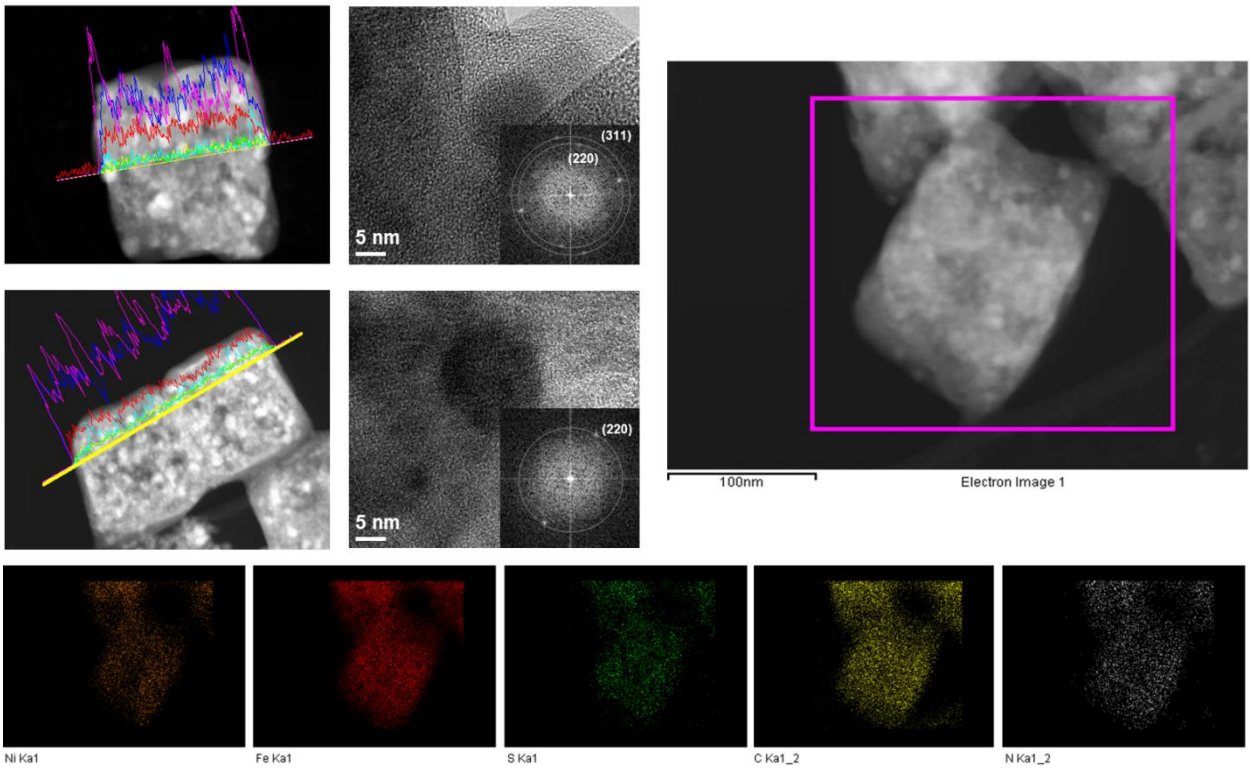

Figure 6-7. TEM analysis of NF-MOF. (A and B) STEM images with EDS line-scans obtained along the middle and edge of NF-MOF, (C and D) HRTEM images and SAED patterns obtained at the center and the edge of NF-MOF, (E) DFTEM image of NF-MOF, and the obtained elemental maps of (F) Ni, (G) Fe, (H) S, (I) C, and (J) N, respectively.

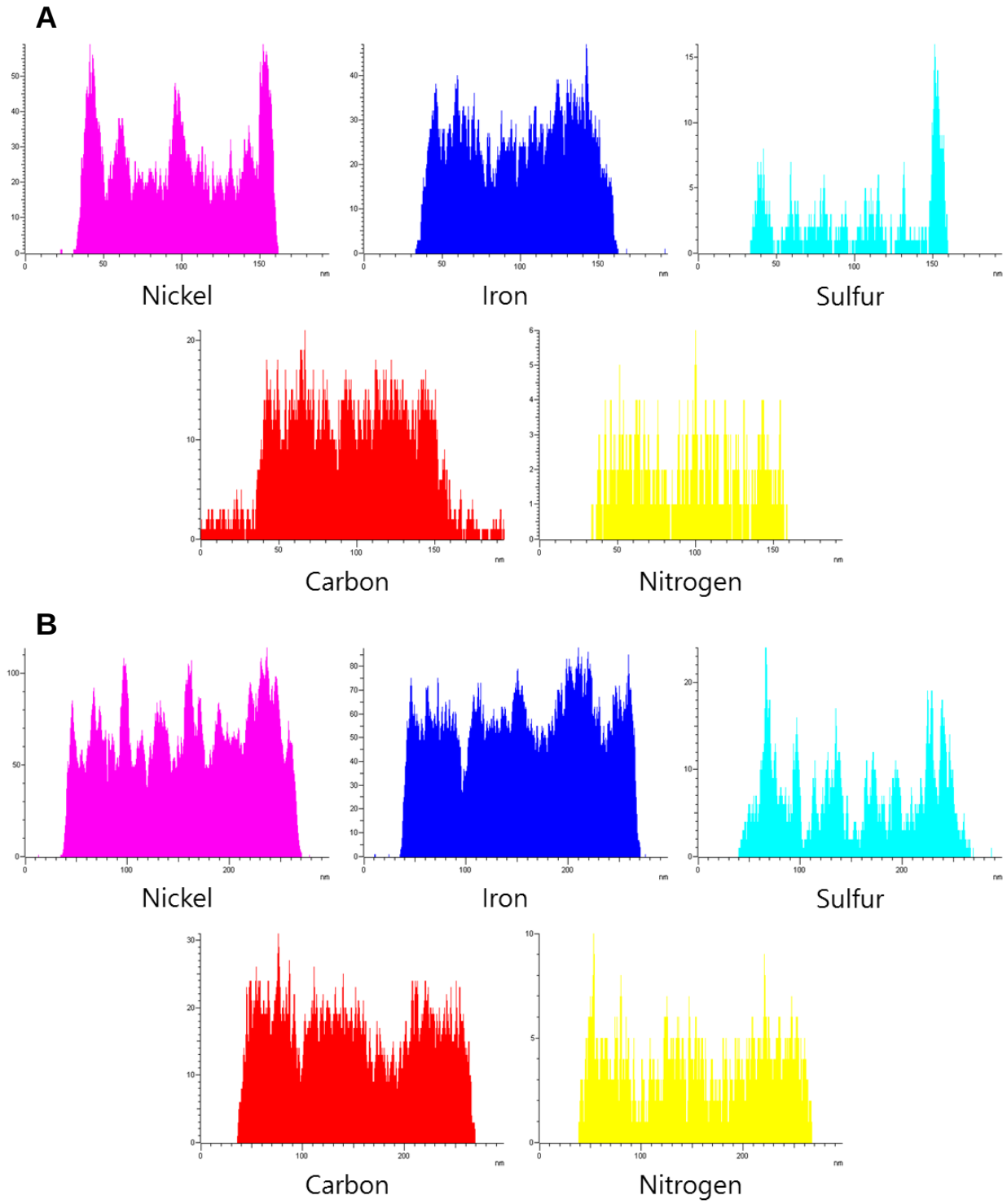

Figure 6-8. EDS line-scan results of NF-MOF along the (A) middle and (B) edge section of nano-cuboids: Interestingly, Ni and Fe ions are observed to be concentrated in an alternating pattern, and the relatively lower amount of S is observed after the ion exchanging reaction.

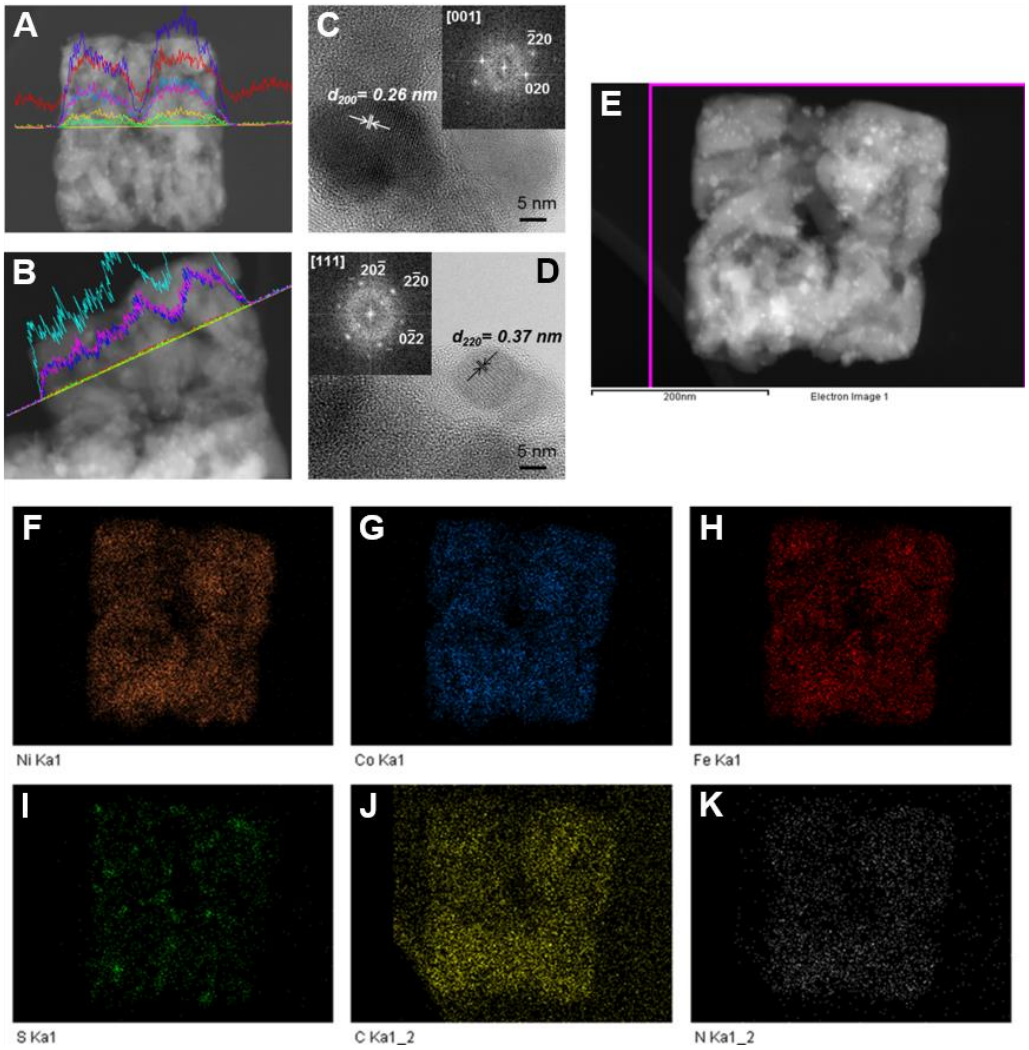

Figure 6-9. TEM analysis of NCF-MOF. (A, and B) STEM images with EELS line-scans obtained along the middle and edge of NCF-MOF, (C, and D) HRTEM images and SAED patterns obtained at the center and the edge of NCF-MOF, (E) DFTEM image of NCF-MOF, and the obtained elemental maps of (F) Ni, (G) Co, (H) Fe, (I) S, (J) C and (K) N.

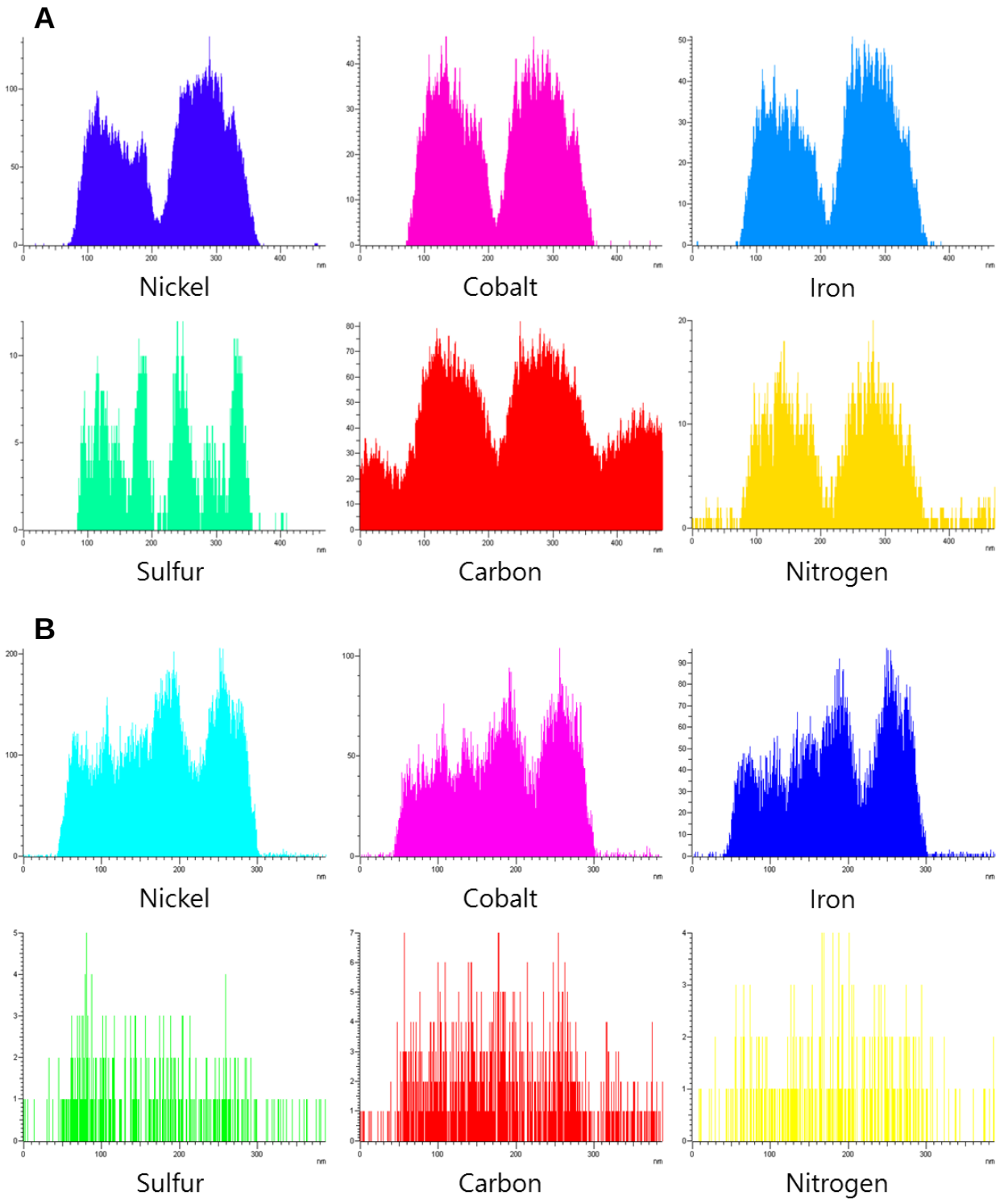

Figure 6-10. EDS line-scan results of NCF-MOF along the (A) middle and (B) edge section of nano-cuboids: Ni, Co, and Fe are observed to be distributed homogeneously, and the relatively lower amount of S is observed after the ion exchanging reaction, especially along the edge.

Based on the above characterizations of NC-MOF and NF-MOF, it is clear that combining $[Co(CN)_6]^{3-}$ and $[Fe(CN)_6]^{3-}$ anions having different rates of ion exchanging capabilities can lead to a unique morphology and composition for NCF-MOF as observed in microscopic analyses. Compared to NC-MOF and NF-MOF, the results obtained from EDS line-scans (**Figure 6-9A**, **6-9B**, and **Figure 6-10**), and DFTEM elemental mapping (**Figure 6-9E-K**) of NCF-MOF show that the three transition metals (nickel, cobalt and iron) are uniformly distributed along the middle and the edge of nano-cuboids, indicating that $[Co(CN)_6]^{3-}$ and $[Fe(CN)_6]^{3-}$ anions were only partially exchanged by S^{2-} ions. This partial ion-exchange led to the formation of multiple voids within a single nano-cuboid, where the exchange most likely progressed from the surface $[Co(CN)_6]^{3-}$ anions to the sites in the core. Accordingly, NCF-MOF is characterized by having larger inter-connected pores in the core with smaller pores near the faces of the nano-cuboid, resulting in a multi-level porous structure. The crystal structure of NCF-MOF confirmed by SAED patterns obtained from HRTEM images at the face center (**Figure 6-9C**) and the edge (**Figure 6-9D**) reveal [001] and [111] planes, respectively, as indicated by a series of bright dots from strongly diffracted crystal planes of the nano-cuboid, corresponding to a typical FCC structure.

The observed porosity of NF-MOF and NCF-MOF was quantified by measuring N_2 adsorption/desorption isotherms and pore size distribution, as presented in **Figure 6-11**. Based on the N_2 isotherms, both NF-MOF and NCF-MOF show a clear hysteresis loop in the high-pressure range from 0.6 to 1.0, indicating the presence of mesopores.[62] However, NCF-MOF adsorbed a much greater volume of N_2 resulting in a 50.7 $m^2\ g^{-1}$ BET surface area, compared to only 27.4 $m^2\ g^{-1}$ obtained with NF-MOF. In terms of the pore size distribution, despite both nano-cuboids having micro-pores (under 2 nm) and mesopores (over 2 nm), NCF-MOF was

found to have two times the accumulative pore volume compared to NF-MOF (0.29 vs. 0.14 cc g^{-1}) due to the presence of a significantly large number of mesopores. This direct evidence that NCF-MOF has enhanced specific surface area signifies a potential increase in the number of active sites for electrocatalytic processes, which can significantly improve OER and HER activities.

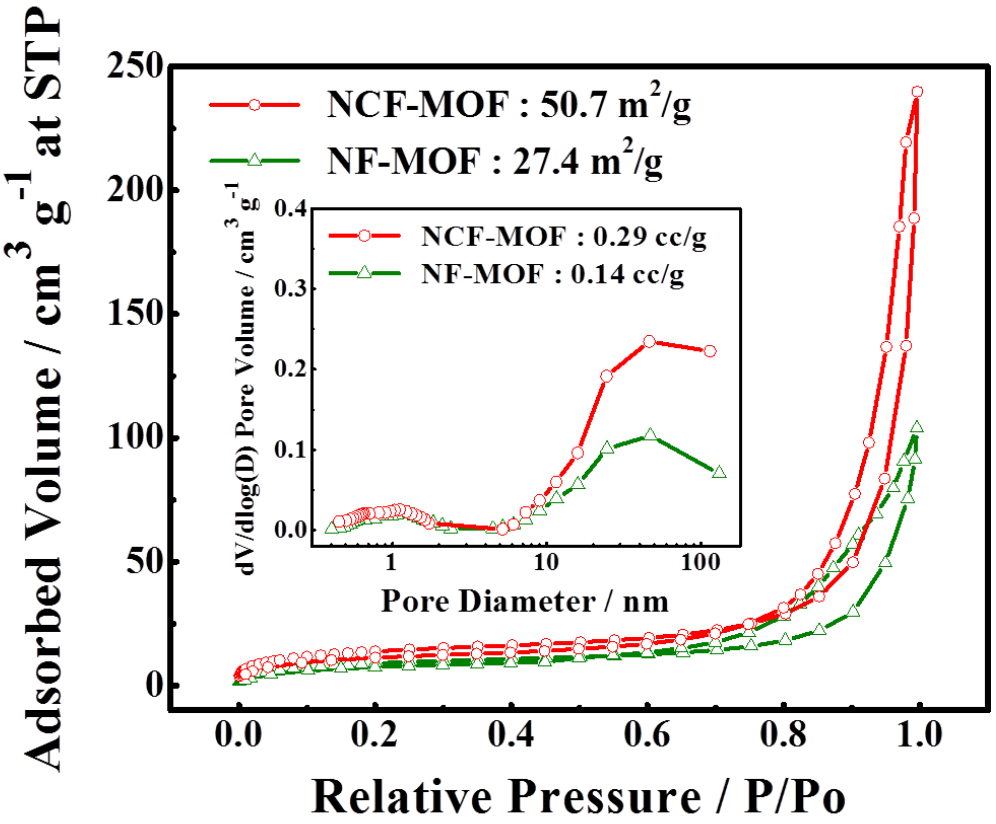

Figure 6-11. N_2 adsorption-desorption isotherms and pore size distribution (Inset) of NCF-MOF (red circles) and NF-MOF (green triangles).

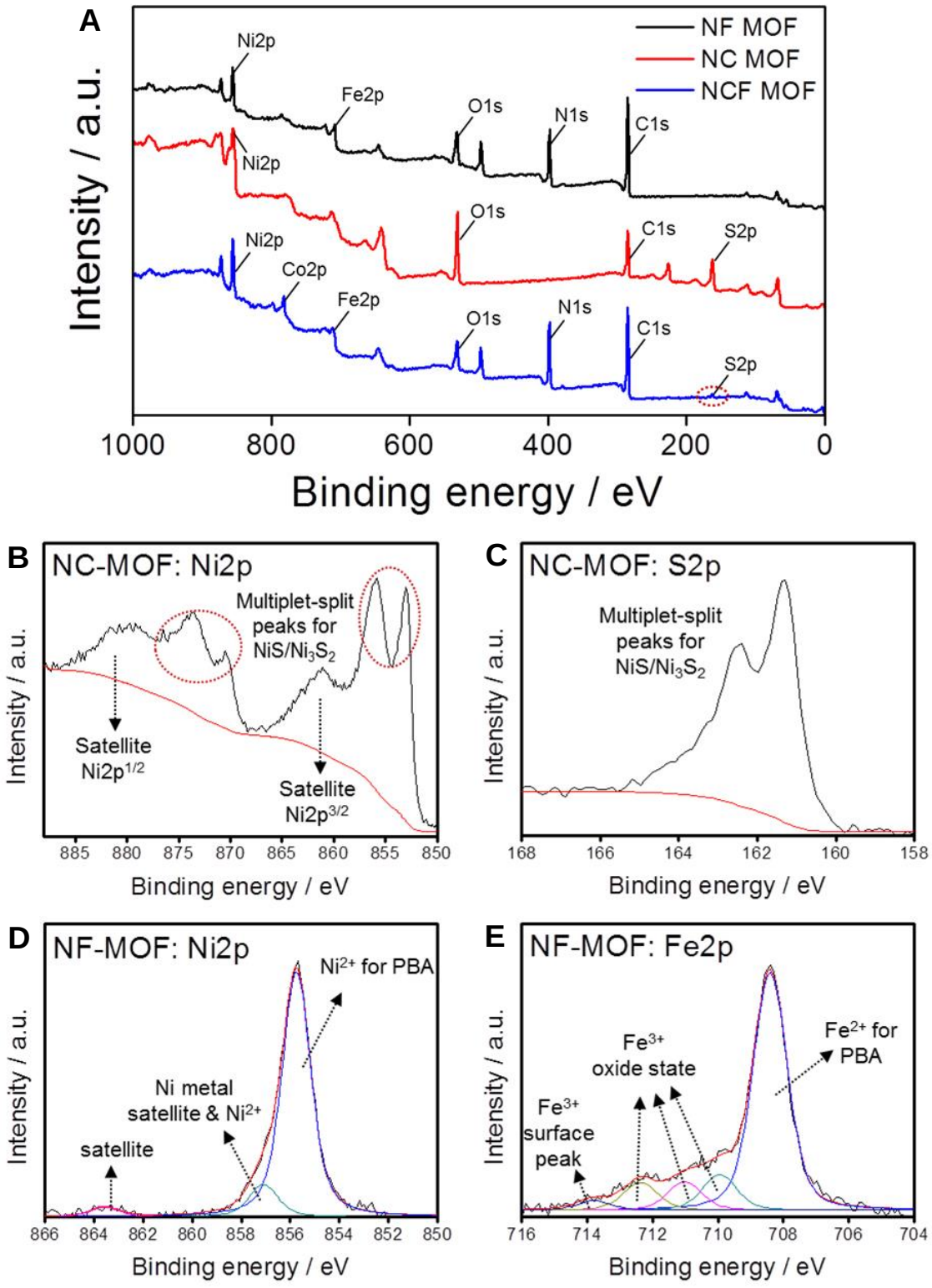

Figure 6-12. (A) Full XPS survey of NC-MOF, NF-MOF, and NCF-MOF. High-resolution XPS spectra of (B) Ni 2p and (C) S 2p of NC-MOF, (D) Ni 2p and (E) Fe 2p of NF-MOF.

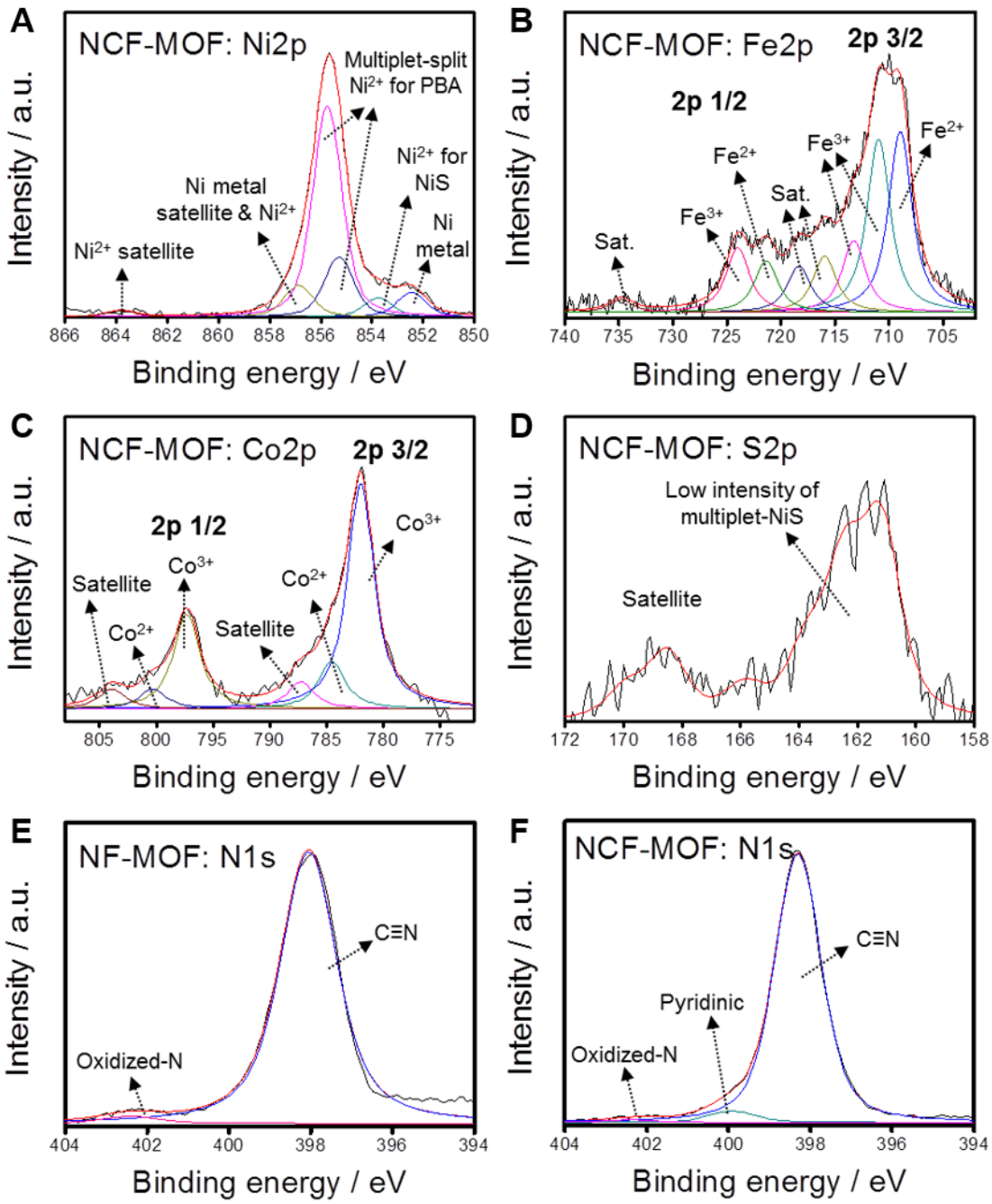

Figure 6-13. De-convoluted high-resolution XPS spectra obtained from NCF-MOF; (A) Ni 2p, (B) Fe 2p, (C) Co 2p, and (D) S 2p. De-convoluted high-resolution XPS N 1s spectra of (E) NF-MOF, and (F)NCF-MOF.

The composition of the MOF nano-cuboid catalysts was further analyzed by X-ray photoelectron spectroscopy (XPS). The survey spectrum of NF-MOF revealed Ni, Fe, O, N, and

S, while that of NCF-MOF revealed Ni, Co, Fe, O, N, C with a low intensity S peak (**Figure 6-12A**). In contrast, the spectrum of NC-MOF revealed Ni, O, C with a high intensity S peak, indicating again that most of the $[Co(CN)_6]^{3-}$ were ion-exchanged with S^{2-} ions leading to the formation of hollow-centered NiS nano-cuboids as discussed earlier. The high-resolution spectrum of selected elements present in the nano-cuboid catalysts was de-convoluted to verify the oxidation states. The high-resolution Ni 2p (**Figure 6-12B**) and S 2p (**Figure 6-12C**) spectra of NC-MOF show peaks found at binding energies that correspond to NiS and Ni_3S_2.[193] While Ni_3S_2 was detected from the XPS analysis, no peaks that corresponded to this impurity in the XRD pattern of NC-MOF were observed, which indicates that its amount may be negligibly small due to a near-complete ion exchange of $[Co(CN)_6]^{3-}$ with S^{2-} during the hydrothermal reaction. Based on the analysis of Ni 2p (**Figure 6-12D**) and Fe 2p (**Figure 6-12E**) signals from NF-MOF, it was found mainly to consist of Ni in 2+ states, and Fe with 27 % of 3+, and 73 % of 2+ states, leading to a possible chemical formula of $Ni_x^{II}[Fe_y^{II}Fe_z^{III}(CN)_6]_2$. NCF-MOF, on the other hand, was found to be composed of Ni in 2+ states (**Figure 6-13A**), Fe in 43 % and 57% of 2+ and 3+ states (**Figure 6-13B**), and Co in 17% and 83 % of 2+ and 3+ states (**Figure 6-13C**), respectively. Based on the high-resolution Ni 2p peak, it was found that a small quantity of NiS formed (5.4 %), while only low-intensity multiplet NiS peaks were observed in the high-resolution S 2p spectrum of NCF-MOF (**Figure 6-13D**), which are ascribed to the S^{2-} ions partially replacing $[Co(CN)_6]^{3-}$ during ion exchange, consistent with the above XRD and microscopic characterization. However, the lack of characteristic NiS peaks observed in the XRD patterns of NF-MOF and NCF-MOF indicate that the small quantities of NiS in these samples were amorphous. These oxidation states of the transition metals determined from XPS analysis are related to the number of valence electrons, which in turn determines the electronic

state and the number of electrons that are involved during electrocatalytic reactions.[71, 133, 194, 195]

Recently, several studies revealed that valence electrons of transition metals are highly related to the trends in adsorption energies of intermediates of the oxygen evolution reaction (OER).[71, 133, 194] In these works, metals and corresponding metal oxides were studied, and the correlation between the number of outer electrons and the adsorption energy of the intermediates such as *OH, *O, and *OOH during oxygen electrocatalysis were systematically investigated. The trends demonstrated the higher the number of outer electrons, the larger the adsorption energies of the oxygen intermediates leading to higher overpotentials towards OER. Furthermore, the trends remained similar across different structures of metals, metal monoxides, as well as perovskite oxides. In the current study, based on the oxidation states determined from the XPS analysis above, the outer electron number of Fe in NF-MOF was found to be 5.73, while those of Fe and Co in NCF-MOF were found to be 2.71 and 2.78, respectively, adding up to 5.49. Considering the number of outer electrons, it can be implied that the active surface of NF-MOF has relatively high adsorption strength with the oxygen intermediates leading to a lower OER electroactivity. Valence electrons of NCF-MOF finely tuned by the combination of active Co and Fe metal ions, on the other hand, would render relatively weaker adsorption of the oxygen intermediates, resulting in lower overpotential toward OER and more facilitated evolution of gaseous oxygen. The improved OER performance resulting from this explanation will be demonstrated by electrochemical evaluation in the next section. The obtained XPS N 1s spectra of NF-MOF and NCF-MOF were de-convoluted to verify the type of nitrogen species present in each electrocatalyst since N-doping has been reported to facilitate HER. It is noted that the N 1s peak was not detected with NC-MOF, as shown in **Figure 6-12A** due to near-complete exchange of $[Co(CN)_6]^{3-}$ with S^{2-} ions. The N species found in NF-MOF predominantly existed as C≡N

(98.7 %), which was from the remaining un-exchanged $[Fe(CN)_6]^{3-}$ anions, and the rest as oxidized-N (1.9 %) formed during the hydrothermal process (**Figure 6-13E**). Interestingly, NCF-MOF, in addition to having C≡N (94.7 %) and oxidized-N (0.9 %), also contained pyridinic N species (4.24 %) (**Figure 6-13F**). This unique N-doping of NCF-MOF is ascribed to the decomposition of free CN^- groups generated in solution during the ion exchanging process. In fact, previous studies reported that $Fe(CN)_6$ is effective in dissociating metal cyanides, decomposing CN^- in soil at temperatures lower than 100 ^oC.[196] Likewise, $Ni_3[Fe(CN)_6]_2$ groups in NCF-MOF most likely facilitated the dissociation of free $[Co(CN)_6]^{3-}$ ions in solution, producing CN^- ions which oxidize to CNO^- and then further decomposes to NH_3, a common N-doping source.[196] This N-doping is unique to NCF-MOF because the remaining $Fe(CN)_6$ groups in the nano-cuboid act as a catalyst to facilitate the decomposition of CN^- groups of the $[Co(CN)_6]^{3-}$ anions freed into the solution after ion exchanging with S^{2-}. Specifically, 9.85 % of $[Co(CN)_6]^{3-}$ in NCF-MOF was ion-exchanged with S^{2-}, and 86 % of the freed CN^- groups were found to be used as the N source based on the XPS analysis. This result is also consistent with the EDS line-scan analysis presented above, which clearly showed the presence of both nitrogen and carbon along the middle and edges of NCF-MOF. This unique N-doping within NCF-MOF, which formed during the decomposition of CN- leads to more favorable HER electrochemical activity due to the synergistic effect with neighboring transition metals such as Ni, Co, and Fe,[176, 178, 197, 198] which will be demonstrated in the next section.

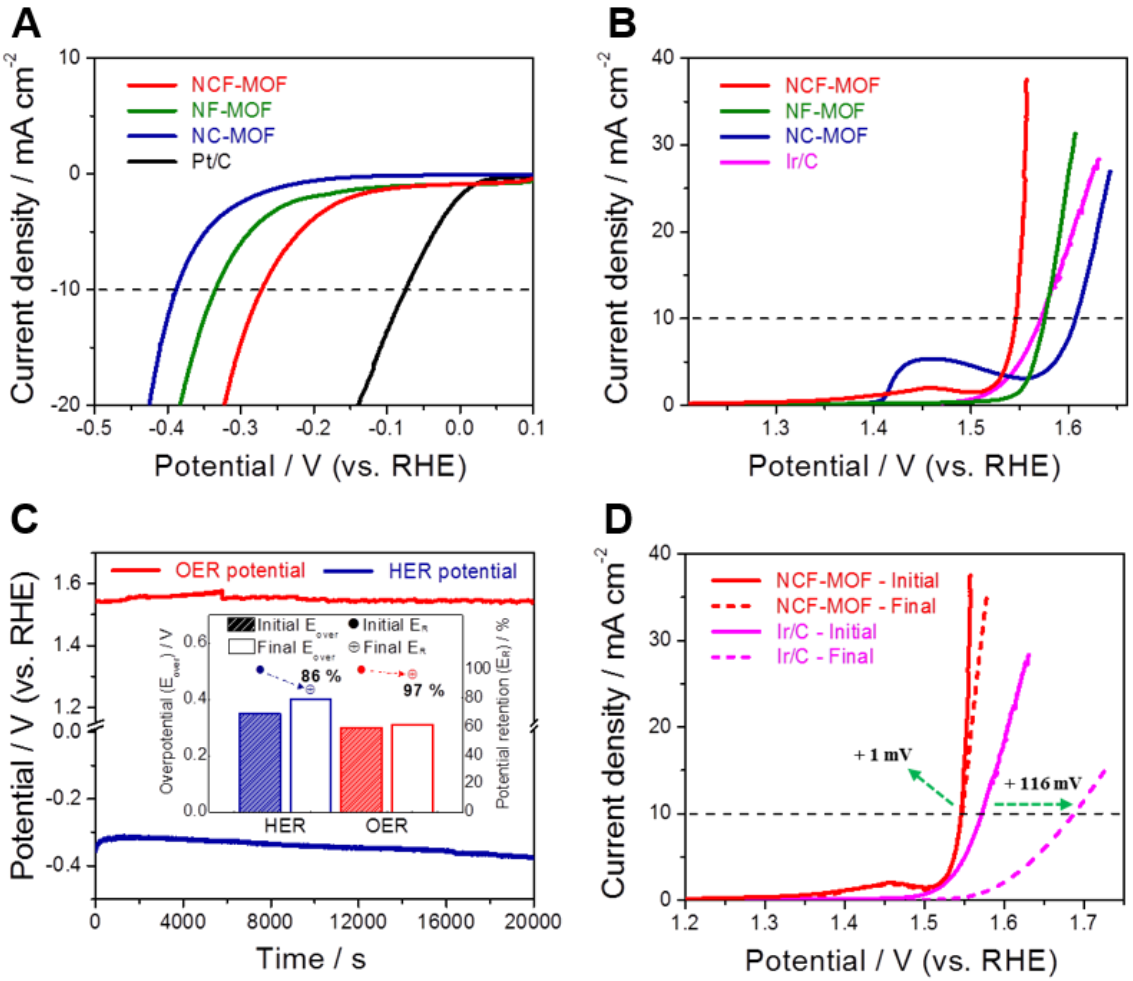

Figure 6-14. Electrochemical evaluations of MOF catalysts. (A) HER and (B) OER curves obtained with MOF catalysts and precious metal-based benchmark catalysts. (C) Chronopotentiometry (v-t) plot obtained with NCF-MOF at a fixed applied current density of -20 mA cm^{-2} for HER (blue line) and 20 mA cm^{-2} for OER (red line). The inset of C shows the changes in the overpotentials during chronopotentiometry HER and OER tests (bar graphs), and the corresponding potential retentions (dot graphs). (D) OER polarization curves of NCF-MOF and Ir/C before (solid lines) and after (dashed lines) 1,000 CV cycles.

The electrochemical OER and HER activities of the MOF electrocatalysts were investigated using a typical three-electrode half-cell configuration with a conventional glassy carbon rotating disk electrode (RDE) with 0.2 mg cm^{-2} of catalyst loading in N_2-saturated 0.1 M KOH electrolyte. Based on the HER polarization curves, NCF-MOF demonstrated the lowest overpotential (most positive absolute potential) of 0.27 V (see measurement details in

Experimental part), compared to those of NF-MOF and NC-MOF (0.34 and 0.39 V, respectively) at a current density of -10 mA cm^{-2} (**Figure 6-14A**). This excellent HER activity of NCF-MOF is comparable to some of the best known non-precious HER catalysts in the underlying condition (See Table S1 in Supplementary data), which is attributed to the reduced energy barrier for HER due to the N-doped species uniquely found in NCF-MOF.[176, 199, 200] Based on the previous study, nitrogen doping leads to a decrease in $\Delta G(H^*)$ by providing improved adsorption for H* onto the active sites.[201-204] Additionally, since the properties of materials are highly sensitive to their morphology and structure, the unique structure, as well as the N-doped surface of NCF-MOF, probably further contributes to its highly active and durable HER activity.[205] As an effective dual-function catalyst, NCF-MOF also showed the lowest OER overpotential of 0.32 V obtained at 10 mA cm^{-2} even compared to that of precious-metal benchmark catalyst Ir/C (**Figure 6-14B**), while it is superior compared to the recently reported non-precious active OER electrocatalysts (**Table 6-1**). Specifically, NF-MOF, NC-MOF, and Ir/C demonstrated 30, 60, and 20 mV higher overpotentials, respectively. The significant OER activity of NCF-MOF is also comparable to the best-reported values of recently developed non-precious metal-based OER electrocatalysts. The enhanced OER activity of NCF-MOF is attributed to the favorably tuned electronic structure by combining the number of outer electrons of active Co and Fe metal ions, which leads to reduced adsorption strength with the oxygen intermediates such as *O, *OH, and *OOH, as discussed above.

Table 6-1. Comparison of OER and HER activities for the MOF nano-cuboids with several recently reported highly active non-precious electrocatalyst in basic media (0.1 M or 1 M KOH) on different electrodes.

Electrocatalyst[a]	Overpotential at -10 mA cm^{-2} (η(HER))[b]	Overpotential at 10 mA cm^{-2} (η(OER))[c]	KOH Molarlity	Catalyst loading	Electrode	Reference
NCF MOF	0.27 V	0.32 V	0.1 M	0.2 mg cm^{-2}	Glassy carbon	This work
NCF MOF	0.11 V	0.19 V	0.1 M	1 mg cm^{-2}	Nickel foam	This work
NF-MOF	0.34 V	0.35 V	0.1 M	0.2 mg cm^{-2}	Glassy carbon	This work
NF MOF	0.14 V	0.23 V	0.1 M	1 mg cm^{-2}	Nickel foam	This work
NC-MOF	0.39 V	0.38 V	0.1 M	0.2 mg cm^{-2}	Glassy carbon	This work
NC MOF	0.18 V	0.29 V	0.1 M	1 mg cm^{-2}	Nickel foam	This work
NiO NRs-m-Ov	0.11 V	-	1 M	0.2 mg cm^{-2}	Carbon fiber paper	206
$LaCo_{0.8}Fe_{0.2}O_2$		0.35 V	0.1 M	0.23 mg cm^{-2}	Glassy carbon	207
Ni_3FeN-Nps	0.16 V	0.28 V	1 M	0.35 mg cm^{-2}	Glassy carbon	208
Mo-RF-F127/NF-NH_3	0.11 V	-	0.1 M	N/A	Nickel foam	209
Co_2B/NG	-	0.38 V	0.1 M	0.2 mg cm^{-2}	Glassy carbon	210
	0.23 V	-	1 M	0.2 mg cm^{-2}	Glassy carbon	
NiFe/$NiCo_2O_4$/NF	0.11 V	0.26 V	1 M	N/A	Nickel foam	211
Ni@NC	-	0.39 V	0.1 M	0.4 mg cm^{-2}	Glassy carbon	212
TCCN	-	0.42 V	0.1 M	1.4 mg cm^{-2}	Free-standing film	213
N-NiFe LDH		0.23 V	0.1 M	0.7 mg cm^{-2}	Nickel foam	214
Co-N-MoO_2	0.26 V		0.1 M	0.2 mg cm^{-2}	Glassy carbon	215
BCFSn	-	0.43 V	0.1 M	0.23 mg cm^{-2}	Glassy carbon	216
Co_3O_4C-NA	-	0.29 V	0.1 M	0.2 mg cm^{-2}	Cu foil	217
g-C_3N_4 NS-CNT	-	0.37 V	0.1 M	0.4 mg cm^{-2}	Glassy carbon	218
NF-NiS_2	0.12 V	0.22 V	1 M	1 mg cm^{-2}	Nickel foam	219
MoCx	0.15 V	-	1 M	0.8 mg cm^{-2}	Glassy carbon	220
S,S-CNT_{1000}	-	0.35 V	1 M	0.23 mg cm^{-2}	Pyrolytic graphite	221
$NiCo_2S_4$ NW	0.21 V	0.26 V	1 M	N/A	Nickel foam	173
	-	0.34 V	0.1 M	N/A	Nickel foam	
Ni-NiO/N-rGO	0.21 V	0.24 V	0.1 M	0.21 mg cm^{-2}	Glassy carbon	222
	0.14 V	-	1 M	1 mg cm^{-2}	Nickel foam	

a: Uni- or bifunctional electrocatalysts for OER and/or HER
b: HER overpotential measured at -10 mA cm^{-2}
c: OER overpotential measured at 10 mA cm^{-2}

To emphasize the excellent OER and HER capabilities of NCF-MOF, the catalysts were also loaded onto practical nickel foam electrodes (NFEs) commonly used in water-splitting cells (see electrode preparation details in Experimental part). Under HER conditions, NCF-MOF again demonstrated the lowest overpotential of 0.16 V obtained at a current density of -30 mA cm^{-2}, compared to those of NF-MOF and NC-MOF (0.25 and 0.30 V, respectively) (**Figure 6-15A**). Additionally, the Tafel plots obtained from the HER curves resulted in the smallest slope for NCF-MOF (114 mV dec^{-1}) compared to those of NF-MOF and NC-MOF (157 and 168 mV dec^{-1}, respectively) (**Figure 6-15B**), signifying much faster kinetics during the HER. Similarly, the lowest OER overpotential was obtained with the NCF-MOF catalyst loaded on a NFE, demonstrating 0.48 V obtained at 30 mA cm^{-2}, which is 110 and 160 mV lower than those of NF-MOF and Ir/C, respectively (**Figure 6-15C**). The OER Tafel analysis also showed the smallest slope of 49 mV dec^{-1} for NCF-MOF, compared to those of NF-MOF, NC-MOF, and Ir/C (119, 99, and 73 mV dec^{-1}, respectively) (**Figure 6-15D**), signifying the highest kinetics during the OER on NCF-MOF.

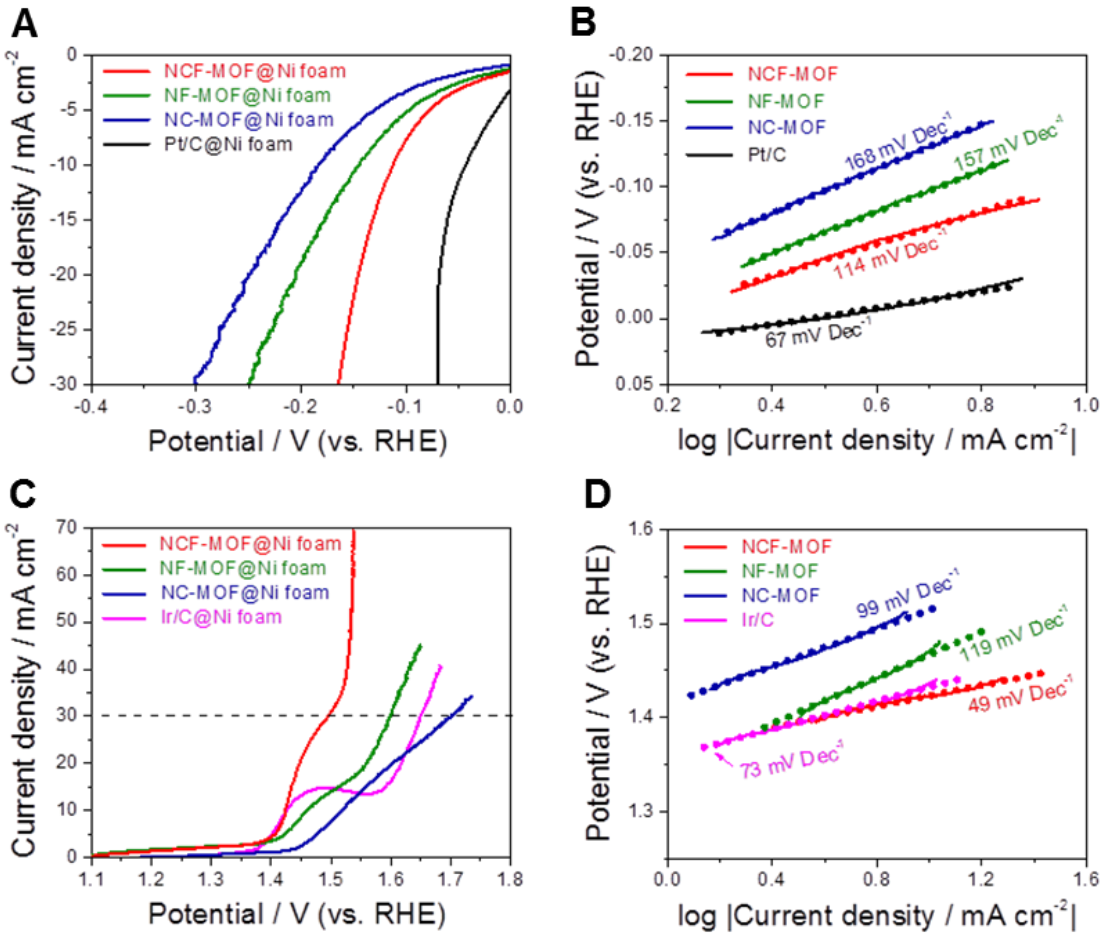

Figure 6-15. Electrochemical evaluations of MOF catalyst-loaded nickel foam electrodes. (A) HER polarization curves, and (B) HER Tafel slopes obtained with NCF-MOF, NF-MOF, NC-MOF, and Pt/C. (C) OER polarization curves, and (D) OER Tafel slopes obtained with NCF-MOF, NF-MOF, NC-MOF, and Ir/C.

In addition to the excellent dual OER and HER activities of NCF-MOF, its electrochemical stability was investigated by conducting chronopotentiometry (CP). When held at -20 mA cm^{-2}, the NCF-MOF electrode exhibited an initial HER potential of -0.34 V vs. RHE, and a voltage loss of only 0.05 V after 20,000 seconds (**Figure 6-14C**). During CP under OER conditions, the NCF-MOF electrode held at 20 mA cm^{-2} demonstrated an initial OER potential of 1.53 V vs. RHE (0.3 V of OER overpotential). After 20,000 seconds, only a 0.01 V increase in the OER potential was observed, leading to 97 % of potential retention, demonstrating very

slight degradation during the durability test (**Figure 6-14C** inset). Conducting electrochemical stability via cyclic voltammetry (CV), as commonly done in the field, further confirmed the considerably high electrochemical stability of NCF-MOF, with Ir/C used as the benchmark catalyst for comparison.[65, 181, 223] Initially, NCF-MOF displayed a significantly lower (superior) OER potential of 1.54 V vs. RHE at 10 mA cm^{-2} in comparison to 1.57 V obtained with Ir/C (**Figure 6-14D**). After 1,000 CV cycles in the highly oxidative potential window of 1.2 to 1.75 V vs. RHE, NCF-MOF showed only 1 mV of OER potential loss (99 % potential retention), while Ir/C showed a significantly more significant potential loss of 116 mV (66 % potential retention). The structural stability of NCF-MOF after the long term durability tests in both OER and HER potential regions was verified by performing TEM characterization in terms of morphology (**Figure 6-16**). The overall nano-cuboid morphology of NCF-MOF (A, B are before durability testing) was observed to be maintained after OER (C, D), and HER (E, F) durability tests in the alkaline electrolyte. The edges were observed to be somewhat roughened, which is likely due to the formation of metal hydroxides where the metal sites tend to be under-coordinated, which is consistent with the results reported in the literature.[224, 225]

The extended electrochemical stability observed with NCF-MOF during HER and OER is likely attributed to the highly rigid porous structure consisting of the robust metal-organic-frameworks, which enables it to mostly retain the initial electrocatalytic activities via retaining the framework during rigorous H_2 and O_2 gas bubbling. Additionally, during OER, even lower overpotential for NCF-MOF than the precious benchmark Ir/C catalyst leads to significantly reduced oxidation of active metals while the catalyst undergoes relatively reduced carbon-corrosion. It can be concluded that the solid and interconnected porous structure via the ternary transition metal-based MOF design, as well as the harmonized effects between Co and Fe metals

in the framework, achieved synergistic improvements in electrocatalytic activities and durability for both OER and HER.

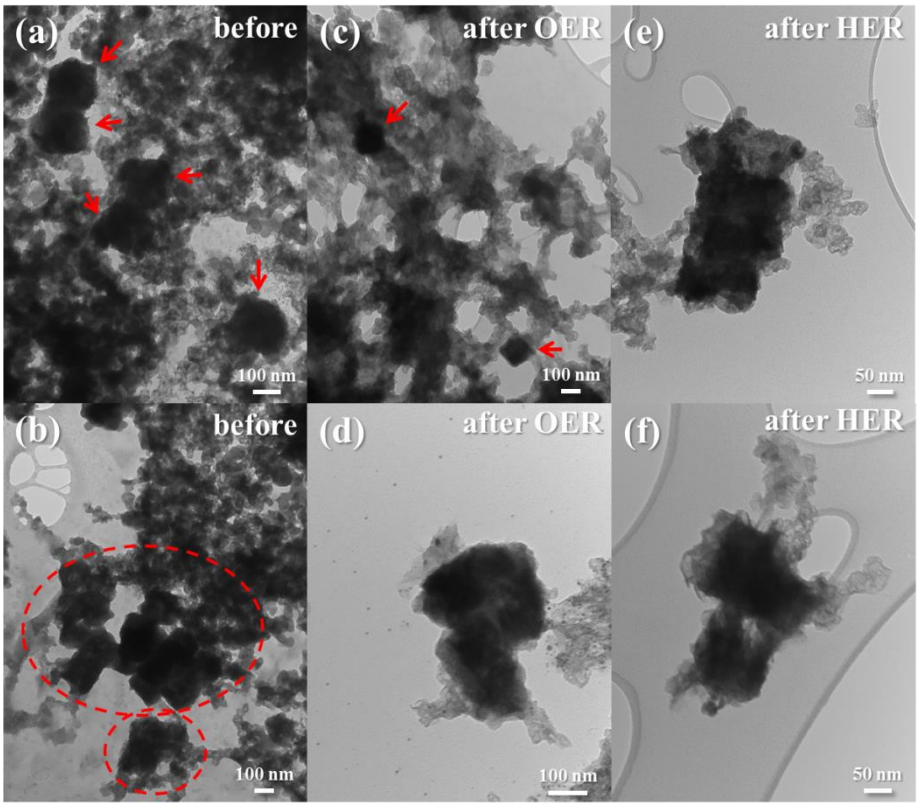

Figure 6-16. TEM images of NCF-MOF catalyst ink (carbon black included) before electrochemical tests (a and b); after durability test in the OER potential region (c and d); after durability test in the HER potential region (e and f). The NCF-MOF particles are highlighted by red arrows and dashed circles.

6.4 Summary

In summary, multi-void nano-cuboidal MOF catalysts prepared by a facile co-precipitation and post-heat treatment process was found to demonstrate high electrocatalytic activities as well as stability toward both OER and HER. The morphology and composition of the MOF catalysts was investigated by taking advantage of different ion exchanging rates of $[Co(CN)_6]^{3-}$ and $[Fe(CN)_6]^{3-}$ anions in PBA precursors with S^{2-} ions. The formation of unique

nano-cuboid morphology with high internal porosity of NCF-MOF is attributed to the ion exchanging of $[Co(CN)_6]^{3-}$ with S^{2-} ions, while relatively unreactive $[Fe(CN)_6]^{3-}$ remains stagnant but facilitates the decomposition of free CN^- groups to induce nitrogen-doping, forming HER active pyridinic nitrogen species. Additionally, the unique combination of the two precursors containing Co and Fe results in a favorably tuned electronic structure, leading to relatively reduced adsorption energy of the oxygen intermediates, which is critical for lowering the overpotential toward OER and facilitating the evolution of gaseous oxygen. In terms of electrochemical stability, after 20,000 seconds of operation NCF-MOF retained 86% and 97% of its HER and OER potentials, respectively, and far exceeded the stability of precious metal-based benchmark catalyst Ir/C, demonstrating minimal OER potential losses after 1,000 CV cycles in a highly oxidative potential window. Furthermore, the TEM analysis verified the high structural stability of NCF-MOF after the long term durability tests conducted in both OER and HER potential regions. This work exemplifies novel electrocatalyst development with high activity and durability for next-generation energy conversion and liquid-fuel production technologies, including electrochemical water-splitting cells.

7. Conclusions and Future Work

7.1 Conclusions

The objectives of the present thesis are to design and synthesize bifunctionally active and durable hierarchically porous architecture electrocatalysts consisting of non-precious transition metals. Furthermore, the effects of second transition metal substituent on the 3DOM metal oxide framework onto both electrocatalytic activity and durability is investigated through the combination of experimental and computational analysis.

The first approach to achieve the objectives is being taken by using a simple template-derived process in which the cobalt precursor solution is absorbed into the voids generated from the stack of the sacrificial polystyrene beads template, and further heating removes the template as well as oxidizes the cobalt precursor to cobalt oxides. With spinel cobalt oxides consistently being reported in the literature as efficient bifunctional oxygen electrocatalysts, the hypothesis of this project is that nano-structuring which renders three-dimensionally ordered macro/mesopores (3DOM) with robust framework would lead to significantly improved electrocatalytic activity and durability. As confirmed in the physicochemical and electrochemical characterizations, the 3DOM Co_3O_4 is capable of catalyzing both oxygen reduction and oxygen evolution reactions at accelerated rates compared to the bulk counterpart. The open and interconnected framework architecture of the catalyst renders much increased active surface area with enlarged pore volume and facilitates diffusion of reactants such as oxygen gas molecules into and out of the structure, as well as accelerates charge transfers leading to better kinetics of the oxygen electrocatalysis. In addition, the robust frameworks of the 3DOM structure demonstrate much longer stability in comparison to the bulk material showing high possibility to be used in rechargeable Zn-air

battery applications. As expected, the 3DOM Co_3O_4 enables charge-discharge cycling over 30 times that of commercial Pt/C and Ir/C precious metal-based catalysts, which is equivalent to over 400 hours of battery life.

In the following project, surface-doping of palladium (Pd) on 3DOM Co_3O_4 and its effect on the catalyst's bifunctional activity and durability under the operating conditions of a rechargeable Zn-air battery is investigated. Half-cell electrochemical testing revealed that the activities of Pd@Co_3O_4(3DOM) are highly comparable to the state-of-the-art commercial carbon-supported palladium (Pd/C), platinum (Pt/C), and iridium (Ir/C) catalysts towards ORR and OER, respectively. More importantly, Pd@Co_3O_4(3DOM) demonstrates significantly extended durability by lasting over 1000 stability cycles without any observable activity degradation. Furthermore, a practical Zn-air battery prototype with the designed catalyst reveals significantly improved charge-discharge overpotential of 0.66 V and lasted over 500 hours of operation. Ab-initio computational simulation of the oxygen reactions reveal that Pd@Co_3O_4(3DOM) is found to be superior in two ways: (i) activity-wise: the d-band center of Pd deposited on 3DOM Co_3O_4 was found to decrease significantly, resulting in increased electron abundance at the Fermi level, which in turn enhanced the overall electrical conductivity; (ii) durability-wise*:* synergistic combination of Pd and 3DOM Co_3O_4 resulted in a significantly improved corrosion resistance, due to the much higher carbon corrosion potential and bulk-like dissolution potential of Pd nanoparticles on 3DOM Co_3O_4. This investigation offers a new rational design strategy for developing highly active and durable transition metal-based oxygen electrocatalysts for electrically rechargeable Zn-air batteries.

In the last approach for accomplishing the objectives of this thesis, a cost-effective, efficient, and durable metal-organic framework (MOF)-based water-splitting catalysts is

investigated. Specifically, a ternary nickel-cobalt-iron (NCF) MOF precursor was designed to produce nano-cuboidal catalysts with multi-level porosity. Physicochemical characterizations have revealed excellent properties of the NCF-MOF electrocatalysts, including (i) the unique rigid and interconnected porous structure significantly improves material utilization and allows rapid mass transport to be maintained, (ii) the fine-tuned ternary transition metal composition optimizes the electronic structure to accelerate the intrinsically sluggish OER, and (iii) the in-situ nitrogen-doping during synthesis enhances the interaction of reaction intermediates with active sites during HER. The unique material advantages successfully render reduced overpotential and significant durability for OER and HER, resulting in excellent water-splitting reactions.

7.2 Proposed Future Work

It is recommended that future work to follow this thesis further improves the activity and durability of the non-precious transition metal-based bifunctional catalysts through nano-structuring. To successfully design and develop the bifunctionally active and durable electrocatalysts, it is required to (i) fully understand the reaction mechanisms for ORR and OER, (ii) identify the active sites of ORR and OER, (iii) verify the main factors which critically affect the activity and durability of the catalyst materials, and (iv) explore what materials can effectively catalyze the oxygen reactions with better kinetics. Accordingly, as mentioned in the body of this thesis, the chemical composition, morphology, oxidation state, crystal structure, and texture of the catalysts must be extensively investigated to obtain enhanced electrochemical performances. Specific research directions are discussed in more detail as follows:

i) Expansion of the 3DOM structure research to the use of mixed transition metals

As it was confirmed that the 3DOM morphology critically improves the activity and durability of ORR and OER in Chapter 4 and that the second transition metal deposition on the 3DOM structure provides further improvements in Chapter 5, the research on 3DOM structured catalyst materials should be expanded to employing mixed transition metals. Adoption of binary or ternary transition metals could provide unexpected synergy and further chances for finely tuning and optimizing the electrocatalytic activity of 3DOM electrocatalysts.

ii) Exploring the more MOF candidates and their hybridization

As the structural advantages of MOF, the strong bonding between transition metal centers and adjacent organic atoms such as carbon, nitrogen, and sulfur shows the great possibility of using the new class of materials for oxygen electrocatalysis. There is a variety of MOFs consisting of different crystalline structures, compositions, morphology, and porous natures. Therefore, more MOF materials can be researched for the design of highly active and durable electrocatalysts, and furthermore, their hybridization could provide unexpected synergy, which can further enhance the electrocatalytic performance.

iii) Systematic integration of the experimental analysis and the computational simulation techniques

Nowadays, advanced in-situ characterization techniques propose new insights into the nature of the active sites and the mechanism of the electrocatalytic reactions, which is gradually

shifting the mode of developing catalyst materials from the traditional empirical trial-and-error methods to precise design and synthesis at molecular or atomic levels. Moreover, thanks to the recent remarkable advances in computational techniques, it is possible to integrate the experimental methods and theoretical predictions, leading to tremendous opportunities in advancing electrochemical surface science at the atomic/molecular level, which can eventually result in many breakthroughs in the research and development of the electrocatalysts. Therefore, the use of both directions is highly recommended to design the bifunctional electrocatalysts with improved activity and durability, as well as a more cost-effective and safe manufacturing process for further extensions from academic studies to industrial production.

REFERENCES

1. F. Y. Cheng and J. Chen, *Chemical Society Reviews*, 2012, **41**, 2172-2192.
2. G. Girishkumar, B. McCloskey, A. C. Luntz, S. Swanson and W. Wilcke, *Journal of Physical Chemistry Letters*, 2010, **1**, 2193-2203.
3. J. S. Lee, S. T. Kim, R. Cao, N. S. Choi, M. Liu, K. T. Lee and J. Cho, *Advanced Energy Materials*, 2011, **1**, 34-50.
4. P. G. Bruce, S. A. Freunberger, L. J. Hardwick and J. M. Tarascon, *Nature Materials*, 2012, **11**, 19-29.
5. G. Nam, J. Park, M. Choi, P. Oh, S. Park, M. G. Kim, N. Park, J. Cho and J.-S. Lee, *ACS Nano*, 2015.
6. Z. Zhao, M. Li, L. Zhang, L. Dai and Z. Xia, *Advance Materials*, 2015, **27**, 6834-6840.
7. J. Wang, H. Wu, D. Gao, S. Miao, G. Wang and X. Bao, *Nano Energy*, 2015, **13**, 387-396.
8. M. Wakihara, *Materials Science and Engineering: R: Reports*, 2001, **33**, 109-134.
9. M. A. Worsley, P. J. Pauzauskie, T. Y. Olson, J. Biener, J. H. Satcher Jr and T. F. Baumann, *Journal of the American Chemical Society*, 2010, **132**, 14067-14069.
10. Y. Li and H. Dai, *Chemical Society Reviews*, 2014, **43**, 5257-5275.
11. J. Fu, Z. P. Cano, M. G. Park, A. Yu, M. Fowler and Z. Chen, *Advanced Materials*, 2017, **29**, 1604685.
12. I. Roche and K. Scott, *Journal of Applied Electrochemistry*, 2009, **39**, 197-204.
13. P. S. Ruvinskiy, A. Bonnefont, C. Pham-Huu and E. R. Savinova, *Langmuir*, 2011, **27**, 9018-9027.
14. L. Mao, K. Arihara, T. Sotomura and T. Ohsaka, *Chemical Communications*, 2003, 2818-2819.
15. D. U. Lee, P. Xu, Z. P. Cano, A. G. Kashkooli, M. G. Park and Z. Chen, *Journal of Materials Chemistry A*, 2016, **4**, 7107-7134.
16. Y.-J. Wang, B. Fang, D. Zhang, A. Li, D. P. Wilkinson, A. Ignaszak, L. Zhang and J. Zhang, *Electrochemical Energy Reviews*, 2018, **1**, 1-34.
17. J.-S. Lee, S. Tai Kim, R. Cao, N.-S. Choi, M. Liu, K. T. Lee and J. Cho, *Advanced Energy Materials*, 2011, **1**, 34-50.
18. F. Cheng and J. Chen, *Chemical Society Reviews*, 2012, **41**, 2172-2192.
19. Z.-L. Wang, D. Xu, J.-J. Xu and X.-B. Zhang, *Chemical Society Reviews*, 2014, **43**, 7746-7786.
20. Y. Nie, L. Li and Z. Wei, *Chemical Society reviews*, 2015, **44**, 2168-2201.
21. Y. Zheng, Y. Jiao, M. Jaroniec and S. Z. Qiao, *Angewandte Chemie International Edition*, 2015, **54**, 52-65.
22. N. T. Suen, S. F. Hung, Q. Quan, N. Zhang, Y. J. Xu and H. M. Chen, *Chemical Society Reviews*, 2017, **46**, 337-365.
23. S. Dresp, F. Luo, R. Schmack, S. Kühl, M. Gliech and P. Strasser, *Energy & Environmental Science*, 2016, **9**, 2020-2024.

24. Y. Shi and B. Zhang, *Chemical Society Reviews*, 2016, **45**, 1529-1541.
25. Y. Cheng and S. P. Jiang, *Progress in Natural Science: Materials International*, 2015, **25**, 545-553.
26. X. Fu, J. Y. Choi, P. Zamani, G. Jiang, M. A. Hoque, F. M. Hassan and Z. Chen, *ACS Applied Materials & Interfaces*, 2016, **8**, 6488-6495.
27. K. Zhang, X. Xia, S. Deng, D. Xie, Y. Lu, Y. Wang, J. Wu, X. Wang and J. Tu, *Journal of Energy Chemistry*, 2019, **37**, 13-17.
28. X. Fu, N. Li, B. Ren, G. Jiang, Y. Liu, F. M. Hassan, D. Su, J. Zhu, L. Yang, Z. Bai, Z. P. Cano, A. Yu and Z. Chen, *Advanced Energy Materials*, 2019, 9, 1803737.
29. K. Choi, I. K. Moon and J. Oh, *Journal of Materials Chemistry A*, 2019, **7**, 1468-1478.
30. H. Tan, Z. Liu, D. Chao, P. Hao, D. Jia, Y. Sang, H. Liu and H. J. Fan, *Advanced Energy Materials*, 2018, **8**.
31. X. Zhong, Y. Jiang, X. Chen, L. Wang, G. Zhuang, X. Li and J.-g. Wang, *Journal of Materials Chemistry A*, 2016, **4**, 10575-10584.
32. K. Sharma, D. Hui, N. H. Kim and J. H. Lee, *Nanoscale*, 2019, **11**, 1205-1216.
33. K. Fan, H. Chen, Y. Ji, H. Huang, P. M. Claesson, Q. Daniel, B. Philippe, H. Rensmo, F. Li, Y. Luo and L. Sun, *Nature Communications*, 2016, **7**, 11981.
34. Y. Bu, G. Nam, S. Kim, K. Choi, Q. Zhong, J. Lee, Y. Qin, J. Cho and G. Kim, *Small*, 2018, 14, 1802767.
35. X. Fan, Z. Peng, R. Ye, H. Zhou and X. Guo, *ACS Nano*, 2015, **9**, 7407-7418.
36. H. Wang, S. Min, Q. Wang, D. Li, G. Casillas, C. Ma, Y. Li, Z. Liu, L. J. Li, J. Yuan, M. Antonietti and T. Wu, *ACS Nano*, 2017, **11**, 4358-4364.
37. H. F. Wang, C. Tang, B. Wang, B. Q. Li and Q. Zhang, *Advance Materials*, 2017, **29**.
38. H. Yin, C. Zhang, F. Liu and Y. Hou, *Advanced Functional Materials*, 2014, **24**, 2930-2937.
39. S. Zhao, M. Li, M. Han, D. Xu, J. Yang, Y. Lin, N.-E. Shi, Y. Lu, R. Yang, B. Liu, Z. Dai and J. Bao, *Advanced Functional Materials*, 2018, **28**.
40. M. Zeng, Y. Liu, F. Zhao, K. Nie, N. Han, X. Wang, W. Huang, X. Song, J. Zhong and Y. Li, *Advanced Functional Materials*, 2016, **26**, 4397-4404.
41. Y. Zhu, W. Sun, W. Chen, T. Cao, Y. Xiong, J. Luo, J. Dong, L. Zheng, J. Zhang, X. Wang, C. Chen, Q. Peng, D. Wang and Y. Li, *Advanced Functional Materials*, 2018, **28**.
42. Y. Tong, P. Chen, T. Zhou, K. Xu, W. Chu, C. Wu and Y. Xie, *Angewandte Chemie International Edition*, 2017, **56**, 7121-7125.
43. S. Zhao, B. Rasimick, W. Mustain and H. Xu, *Applied Catalysis B: Environmental*, 2017, **203**, 138-145.
44. S. Dou, L. Tao, J. Huo, S. Wang and L. Dai, *Energy & Environmental Science*, 2016, 9, 1320-1326.
45. L. Roldán, A. M. Benito and E. Garcia-Bordeje, *Journal of Materials Chemistry A*, 2015.
46. Y. Liang, Y. Li, H. Wang, J. Zhou, J. Wang, T. Regier and H. Dai, *Nature Materials*, 2011, **10**, 780-786.

47. H. Chen, K. Shen, Q. Mao, J. Chen and Y. Li, *ACS Catalysis*, 2018, **8**, 1417-1426.
48. S. Jin, *ACS Energy Letters*, 2019, **4**, 1443-1445.
49. W. Chen, J. Pei, C. T. He, J. Wan, H. Ren, Y. Wang, J. Dong, K. Wu, W. C. Cheong, J. Mao, X. Zheng, W. Yan, Z. Zhuang, C. Chen, Q. Peng, D. Wang and Y. Li, *Advance Materials*, 2018, **30**, e1800396.
50. S. Liu, Z. Wang, S. Zhou, F. Yu, M. Yu, C. Y. Chiang, W. Zhou, J. Zhao and J. Qiu, *Advance Materials*, 2017, **29**.
51. J. Wang, Z. Li, Y. Wu and Y. Li, *Advance Materials*, 2018, 30, 1801649.
52. M. Zhang, Q. Dai, H. Zheng, M. Chen and L. Dai, *Advance Materials*, 2018, **30**.
53. Y. Jiang, Y.-P. Deng, J. Fu, D. U. Lee, R. Liang, Z. P. Cano, Y. Liu, Z. Bai, S. Hwang, L. Yang, D. Su, W. Chu and Z. Chen, *Advanced Energy Materials*, 2018, **8**, 1702900.
54. Y. Li, B. Jia, Y. Fan, K. Zhu, G. Li and C.-Y. Su, *Advanced Energy Materials*, 2018, **8**, 1702048.
55. H. Wang, Q.-L. Zhu, R. Zou and Q. Xu, *Chem*, 2017, **2**, 52-80.
56. Y. He, S. Hwang, D. A. Cullen, M. A. Uddin, L. Langhorst, B. Li, S. Karakalos, A. J. Kropf, E. C. Wegener, J. Sokolowski, M. Chen, D. Myers, D. Su, K. L. More, G. Wang, S. Litster and G. Wu, *Energy & Environmental Science*, 2019, **12**, 250-260.
57. J. Wang, Z. Huang, W. Liu, C. Chang, H. Tang, Z. Li, W. Chen, C. Jia, T. Yao, S. Wei, Y. Wu and Y. Li, *Journal of the American Chemical Society*, 2017, **139**, 17281-17284.
58. J. Duan, S. Chen and C. Zhao, *Nature Communications*, 2017, **8**, 15341.
59. B. Y. Xia, Y. Yan, N. Li, H. B. Wu, X. W. Lou and X. Wang, *Nature Energy*, 2016, **1**, 15006.
60. Malla P.B., Komameni S, *Advances in Soil Science*, 1990, **12**, 159-186.
61. E. Gileadi, *Cell*, 2011, **3**, 4.
62. M. G. Park, D. U. Lee, M. H. Seo, Z. P. Cano and Z. Chen, *Small*, 2016, **12**, 2707-2714.
63. D. H. W. Park, D. U. Lee, M. G. Park, R. Ahmed, D. M. H. Seo, P. L. F. Nazar and P. Z. Chen, *ChemSusChem*, 2015, **8**, 8.
64. D. U. Lee, H. W. Park, M. G. Park, V. Ismayilov and Z. Chen, *ACS Applied Materials & Interfaces*, 2014, **7**, 902-910.
65. D. U. Lee, M. G. Park, H. W. Park, M. H. Seo, X. Wang and Z. Chen, *ChemSusChem*, 2015, **8**, 3129-3138.
66. Z.-F. Huang, J. Wang, Y. Peng, C.-Y. Jung, A. Fisher and X. Wang, *Advanced Energy Materials*, 2017, **7**, 1700544.
67. M. Shao, Q. Chang, J.-P. Dodelet and R. Chenitz, *Chemical Reviews*, 2016, **116**, 3594-3657.
68. Y. Liang, Y. Li, H. Wang, J. Zhou, J. Wang, T. Regier and H. Dai, *Nature Materials*, 2011, **10**, 780-786.
69. D. U. Lee, M. G. Park, H. W. Park, M. H. Seo, X. Wang and Z. Chen, *ChemSusChem*, 2015, **8**, 3129-3138.

70. Z. Chen, A. P. Yu, D. Higgins, H. Li, H. J. Wang and Z. W. Chen, *Nano Letters*, 2012, **12**, 1946-1952.
71. M. H. Seo, H. W. Park, D. U. Lee, M. G. Park and Z. Chen, *ACS Catalysis*, 2015, **5**, 4337-4344.
72. R. Cao, J.-S. Lee, M. Liu and J. Cho, *Advanced Energy Materials*, 2012, **2**, 816-829.
73. J.-S. Lee, S. Tai Kim, R. Cao, N.-S. Choi, M. Liu, K. T. Lee and J. Cho, *Advanced Energy Materials*, 2011, **1**, 34-50.
74. F. Cheng and J. Chen, *Chemical Society Reviews*, 2012, **41**, 2172-2192.
75. Y. Li, M. Gong, Y. Liang, J. Feng, J. E. Kim, H. Wang, G. Hong, B. Zhang and H. Dai, *Nature Communications*, 2013, **4**, 1805.
76. D. U. Lee, B. J. Kim and Z. Chen, *Journal of Materials Chemistry A*, 2013, **1**, 4754-4762.
77. J. Masa, W. Xia, I. Sinev, A. Zhao, Z. Sun, S. Grutzke, P. Weide, M. Muhler and W. Schuhmann, *Angewandte Chemie International Edition*, 2014, **53**, 8508-8512.
78. X. Liu, M. Park, M. G. Kim, S. Gupta, G. Wu and J. Cho, *Angewandte Chemie International Edition*, 2015, **54**, 9654-9658.
79. X. Liu, W. Liu, M. Ko, M. Park, M. G. Kim, P. Oh, S. Chae, S. Park, A. Casimir and G. Wu, *Advanced Functional Materials*, 2015, **25**, 5799-5808.
80. Z. Chen, A. Yu, D. Higgins, H. Li, H. Wang and Z. Chen, *Nano letters*, 2012, **12**, 1946-1952.
81. T. Y. Ma, S. Dai, M. Jaroniec and S. Z. Qiao, *Journal of the American Chemical Society*, 2014, **136**, 13925-13931.
82. H. Cheng, Y.-Z. Su, P.-Y. Kuang, G.-F. Chen and Z.-Q. Liu, *J. Mater. Chem. A*, 2015, **3**, 19314-19321.
83. J. Suntivich, H. A. Gasteiger, N. Yabuuchi, H. Nakanishi, J. B. Goodenough and Y. Shao-Horn, *Nature Chemistry*, 2011, **3**, 5.
84. C.-F. Chen, G. King, R. M. Dickerson, P. A. Papin, S. Gupta, W. R. Kellogg and G. Wu, *Nano Energy*, 2015, **13**, 10.
85. J. I. Jung, H. Y. Jeong, J. S. Lee, M. G. Kim and J. Cho, *Angewandte Chemie International Edition*, 2014, **53**, 4582-4586.
86. J. W. D. Ng, M. Tang and T. F. Jaramillo, *Energy & Environmental Science*, 2014, **7**, 2017-2024.
87. C. Jin, F. Lu, X. Cao, Z. Yang and R. Yang, *Journal of Materials Chemistry A*, 2013, **1**, 12170-12177.
88. M. Prabu, K. Ketpang and S. Shanmugam, *Nanoscale*, 2014, **6**, 3173-3181.
89. F. Cheng, J. Shen, B. Peng, Y. Pan, Z. Tao and J. Chen, *Nature Chemistry*, 2011, **3**, 79-84.
90. Z. Zhuang, W. Sheng and Y. Yan, *Advanced materials*, 2014, **26**, 3950-3955.
91. Y. Liu, D. C. Higgins, J. Wu, M. Fowler and Z. Chen, *Electrochemistry Communications*, 2013, **34**, 125-129.

92. D. U. Lee, J. Scott, H. W. Park, S. Abureden, J.-Y. Choi and Z. Chen, *Electrochemistry Communications*, 2014, **43**, 109-112.
93. D. U. Lee, J.-Y. Choi, K. Feng, H. W. Park and Z. Chen, *Advanced Energy Materials*, 2014, **4**.
94. Y. Li, M. Gong, Y. Liang, J. Feng, J.-E. Kim, H. Wang, G. Hong, B. Zhang and H. Dai, *Nature Communications*, 2013, **4**, 1805.
95. X. Liu, G. Qiu and X. Li, *Nanotechnology*, 2005, **16**, 3035.
96. X. Lu, H. Chan, C.-L. Sun, C.-M. Tseng and C. Zhao, *Journal of Materials Chemistry A*, 2015.
97. J.-J. Xu, Z.-L. Wang, D. Xu, F.-Z. Meng and X.-B. Zhang, *Energy & Environmental Science*, 2014, **7**, 2213-2219.
98. C. Zhu, D. Wen, S. Leubner, M. Oschatz, W. Liu, M. Holzschuh, F. Simon, S. Kaskel and A. Eychmüller, *Chemical Communications*, 2015, **51**, 7851-7854.
99. K. S. Sing, *Pure and applied chemistry*, 1985, **57**, 603-619.
100. C. Weidenthaler, *Nanoscale*, 2011, **3**, 792-810.
101. J. Zhang, K. Sasaki, E. Sutter and R. Adzic, *Science*, 2007, **315**, 220-222.
102. M. H. Seo, M. G. Park, D. U. Lee, X. Wang, W. Ahn, S. H. Noh, S. M. Choi, Z. P. Cano, B. Han and Z. Chen, *Applied Catalysis B: Environmental*, 2018, **239**, 677-687.
103. B. Dunn, H. Kamath and J.-M. Tarascon, *Science*, 2011, **334**, 928.
104. M. E. Scofield, H. Liu and S. S. Wong, *Chemical Society Reviews*, 2015, **44**, 5836-5860.
105. Z.-L. Wang, D. Xu, J.-J. Xu and X.-B. Zhang, *Chemical Society Reviews*, 2014, **43**, 7746-7786.
106. D. Larcher and J. M. Tarascon, *Nature Chemistry*, 2014, **7**, 19.
107. Y. Li and H. Dai, *Chemical Society Reviews*, 2014, **43**, 5257-5275.
108. M. P. Browne, H. Nolan, G. S. Duesberg, P. E. Colavita and M. E. G. Lyons, *ACS Catalysis*, 2016, **6**, 2408-2415.
109. Q. Liu, Y. Wang, L. Dai and J. Yao, *Advanced Materials*, 2016, **28**, 3000-3006.
110. J. Duan, S. Chen, M. Jaroniec and S. Z. Qiao, *ACS Catalysis*, 2015, **5**, 5207-5234.
111. J. Zhang, Z. Zhao, Z. Xia and L. Dai, *Nature Nanotechnology*, 2015, **10**, 444.
112. D. U. Lee, H. W. Park, M. G. Park, V. Ismayilov and Z. Chen, *ACS Applied Materials & Interfaces*, 2015, **7**, 902-910.
113. P. Ganesan, M. Prabu, J. Sanetuntikul and S. Shanmugam, *ACS Catalysis*, 2015, **5**, 3625-3637.
114. H. W. Park, D. U. Lee, P. Zamani, M. H. Seo, L. F. Nazar and Z. Chen, *Nano Energy*, 2014, **10**, 192-200.
115. L. Li, S.-H. Chai, S. Dai and A. Manthiram, *Energy & Environmental Science*, 2014, **7**, 2630-2636.
116. P. Hohenberg and W. Kohn, *Physical Review*, 1964, **136**, B864-B871.
117. W. Kohn and L. J. Sham, *Physical Review*, 1965, **140**, A1133-A1138.
118. L. Li, S. Liu and A. Manthiram, *Nano Energy*, 2015, **12**, 852-860.

119. A. Muthukrishnan, Y. Nabae, T. Okajima and T. Ohsaka, *ACS Catalysis*, 2015, **5**, 5194-5202.
120. J. Wang, K. Li, H.-x. Zhong, D. Xu, Z.-l. Wang, Z. Jiang, Z.-j. Wu and X.-b. Zhang, *Angewandte Chemie International Edition*, 2015, **54**, 10530-10534.
121. U. I. Kramm, I. Herrmann-Geppert, J. Behrends, K. Lips, S. Fiechter and P. Bogdanoff, *Journal of the American Chemical Society*, 2016, **138**, 635-640.
122. J. Greeley, I. E. L. Stephens, A. S. Bondarenko, T. P. Johansson, H. A. Hansen, T. F. Jaramillo, J. Rossmeisl, I. Chorkendorff and J. K. Nørskov, *Nature Chemistry*, 2009, **1**, 552-556.
123. V. R. Stamenkovic, B. Fowler, B. S. Mun, G. Wang, P. N. Ross, C. A. Lucas and N. M. Marković, *Science*, 2007, **315**, 493.
124. B. Hammer and J. K. Norskov, *Nature*, 1995, **376**, 238-240.
125. B. Hammer and J. K. Nørskov, *Surface Science*, 1995, **343**, 211-220.
126. U. B. Demirci, *Journal of Power Sources*, 2007, **173**, 11-18.
127. M. Shao, K. Sasaki, N. S. Marinkovic, L. Zhang and R. R. Adzic, *Electrochemistry Communications*, 2007, **9**, 2848-2853.
128. M. H. Shao, T. Huang, P. Liu, J. Zhang, K. Sasaki, M. B. Vukmirovic and R. R. Adzic, *Langmuir*, 2006, **22**, 10409-10415.
129. J. Greeley and M. Mavrikakis, *Nature Materials*, 2004, **3**, 810-815.
130. M. Shao, P. Liu, J. Zhang and R. Adzic, *The Journal of Physical Chemistry B*, 2007, **111**, 6772-6775.
131. N. Ramaswamy, U. Tylus, Q. Jia and S. Mukerjee, *Journal of the American Chemical Society*, 2013, **135**, 15443-15449.
132. J. E. Huheey, E. A. Keiter and R. L. Keiter, *Inorganic Chemistry: Principles of Structure and Reactivity*, HarperCollins College Publishers, New York, NY, 1993.
133. F. Calle-Vallejo, O. A. Díaz-Morales, M. J. Kolb and M. T. M. Koper, *ACS Catalysis*, 2015, **5**, 869-873.
134. J. K. Seo, A. Khetan, M. H. Seo, H. Kim and B. Han, *Journal of Power Sources*, 2013, **238**, 137-143.
135. M. H. Seo, S. M. Choi, E. J. Lim, I. H. Kwon, J. K. Seo, S. H. Noh, W. B. Kim and B. Han, *ChemSusChem*, 2014, **7**, 2609-2620.
136. D. Higgins, M. A. Hoque, M. H. Seo, R. Wang, F. Hassan, J.-Y. Choi, M. Pritzker, A. Yu, J. Zhang and Z. Chen, *Advanced Functional Materials*, 2014, **24**, 4325-4336.
137. S. H. Noh, M. H. Seo, J. K. Seo, P. Fischer and B. Han, *Nanoscale*, 2013, **5**, 8625-8633.
138. G. Kresse and J. Furthmüller, *Physical Review B*, 1996, **54**, 11169-11186.
139. J. P. Perdew, K. Burke and M. Ernzerhof, *Physical Review Letters*, 1996, **77**, 3865-3868.
140. G. Kresse and J. Furthmüller, *Computational Materials Science*, 1996, **6**, 15-50.
141. G. Kresse and D. Joubert, *Physical Review B*, 1999, **59**, 1758-1775.
142. P. E. Blöchl, *Physical Review B*, 1994, **50**, 17953-17979.

143. G. Hautier, S. P. Ong, A. Jain, C. J. Moore and G. Ceder, *Physical Review B*, 2012, **85**, 155208.
144. C. Franchini, R. Podloucky, J. Paier, M. Marsman and G. Kresse, *Physical Review B*, 2007, **75**, 195128.
145. Y.-L. Lee, J. Kleis, J. Rossmeisl and D. Morgan, *Physical Review B*, 2009, **80**, 224101.
146. M. Methfessel and A. T. Paxton, *Physical Review B*, 1989, **40**, 3616-3621.
147. P. E. Blöchl, O. Jepsen and O. K. Andersen, *Physical Review B*, 1994, **49**, 16223-16233.
148. P. Kratzer, B. Hammer and J. K. No/rskov, *The Journal of Chemical Physics*, 1996, **105**, 5595-5604.
149. M. Wakisaka, S. Mitsui, Y. Hirose, K. Kawashima, H. Uchida and M. Watanabe, *The Journal of Physical Chemistry B*, 2006, **110**, 23489-23496.
150. M. H. Seo, S. M. Choi, D. U. Lee, W. B. Kim and Z. Chen, *Journal of Power Sources*, 2015, **300**, 1-9.
151. D. Su, S. Dou and G. Wang, *Scientific Reports*, 2014, **4**, 5767.
152. H.-Y. Wang, S.-F. Hung, H.-Y. Chen, T.-S. Chan, H. M. Chen and B. Liu, *Journal of the American Chemical Society*, 2016, **138**, 36-39.
153. P. W. Menezes, A. Indra, A. Bergmann, P. Chernev, C. Walter, H. Dau, P. Strasser and M. Driess, *Journal of Materials Chemistry A*, 2016, **4**, 10014-10022.
154. Y. Liang, H. Wang, J. Zhou, Y. Li, J. Wang, T. Regier and H. Dai, *Journal of the American Chemical Society*, 2012, **134**, 3517-3523.
155. X. Wang, L. Zou, H. Fu, Y. Xiong, Z. Tao, J. Zheng and X. Li, *ACS Appl Mater Interfaces*, 2016, **8**, 8436-8444.
156. H. W. Park, D. U. Lee, M. G. Park, R. Ahmed, M. H. Seo, L. F. Nazar and Z. Chen, *ChemSusChem*, 2015, **8**, 1058-1065.
157. B. Lim, M. Jiang, P. H. C. Camargo, E. C. Cho, J. Tao, X. Lu, Y. Zhu and Y. Xia, *Science*, 2009, **324**, 1302.
158. S. Zhang, X. Yuan, H. Wang, W. Mérida, H. Zhu, J. Shen, S. Wu and J. Zhang, *International Journal of Hydrogen Energy*, 2009, **34**, 388-404.
159. L. Tang, B. Han, K. Persson, C. Friesen, T. He, K. Sieradzki and G. Ceder, *Journal of the American Chemical Society*, 2010, **132**, 596-600.
160. X. Zhou, J. Qiao, L. Yang and J. Zhang, *Advanced Energy Materials*, 2014, **4**, 1301523.
161. *Journal of the American Chemical Society*, 2006, **128**, 5585-5585.
162. M. Pourbaix, 1974.
163. W. Ahn, M. G. Park, D. U. Lee, M. H. Seo, G. Jiang, Z. P. Cano, F. M. Hassan and Z. Chen, *Advanced Functional Materials*, 2018, **28**, 1802129.
164. Y. Zheng, Y. Jiao, S. Qiao and A. Vasileff, *Angewandte Chemie International Edition*, 2017.
165. Y. Pan, R. Lin, Y. Chen, S. Liu, W. Zhu, X. Cao, W. Chen, K. Wu, W. C. Cheong, Y. Wang, L. Zheng, J. Luo, Y. Lin, Y. Liu, C. Liu, J. Li, Q. Lu, X. Chen, D. Wang, Q. Peng, C. Chen and Y. Li, *Journal of the American Chemical Society*, 2018, **140**, 4218-4221.

166. Y. P. Zhu, Y. Jing, A. Vasileff, T. Heine and S.-Z. Qiao, *Advanced Energy Materials*, 2017, **7**, 1602928.
167. H. Jiang, Q. He, C. Wang, H. Liu, Y. Zhang, Y. Lin, X. Zheng, S. Chen, P. M. Ajayan and L. Song, *Advanced Energy Materials*, 2018, 8, 1800436.
168. X. Jia, Y. Zhao, G. Chen, L. Shang, R. Shi, X. Kang, G. I. N. Waterhouse, L.-Z. Wu, C.-H. Tung and T. Zhang, *Advanced Energy Materials*, 2016, **6**.
169. T. Y. Ma, J. L. Cao, M. Jaroniec and S. Z. Qiao, *Angewandte Chemie International Edition*, 2016, **55**, 1138-1142.
170. J. Zhang, L. Qu, G. Shi, J. Liu, J. Chen and L. Dai, *Angew Chem Int Ed Engl*, 2016, **55**, 2230-2234.
171. Z. Li, M. Shao, L. Zhou, R. Zhang, C. Zhang, M. Wei, D. G. Evans and X. Duan, *Advanced materials*, 2016, **28**, 2337-2344.
172. A. Mahmood, W. Guo, H. Tabassum and R. Zou, *Advanced Energy Materials*, 2016, **6**, 1600423.
173. A. Sivanantham, P. Ganesan and S. Shanmugam, *Advanced Functional Materials*, 2016, **26**, 4661-4672.
174. S. You, X. Gong, W. Wang, D. Qi, X. Wang, X. Chen and N. Ren, *Advanced Energy Materials*, 2016, **6**, 1501497.
175. X. F. Lu, P. Q. Liao, J. W. Wang, J. X. Wu, X. W. Chen, C. T. He, J. P. Zhang, G. R. Li and X. M. Chen, *Journal of the American Chemical Society*, 2016, **138**, 8336-8339.
176. K. Jayaramulu, J. Masa, O. Tomanec, D. Peeters, V. Ranc, A. Schneemann, R. Zboril, W. Schuhmann and R. A. Fischer, *Advanced Functional Materials*, 2017, **27**, 1700451.
177. J. Nai, B. Y. Guan, L. Yu and X. W. D. Lou, *Science Advances*, 2017, **3**, e1700732.
178. J. Wang, F. Xu, H. Jin, Y. Chen and Y. Wang, *Advanced materials*, 2017, **29**.
179. J. Masa, P. Weide, D. Peeters, I. Sinev, W. Xia, Z. Sun, C. Somsen, M. Muhler and W. Schuhmann, *Advanced Energy Materials*, 2016, **6**, n/a-n/a.
180. J. Ren, M. Antonietti and T.-P. Fellinger, *Advanced Energy Materials*, 2015, **5**, 1401660.
181. D. U. Lee, M. G. Park, Z. P. Cano, W. Ahn and Z. Chen, *ChemSusChem*, 2017.
182. X. Cui, S. Yang, X. Yan, J. Leng, S. Shuang, P. M. Ajayan and Z. Zhang, *Advanced Functional Materials*, 2016, **26**, 5708-5717.
183. Y. Hou, Z. Wen, S. Cui, S. Ci, S. Mao and J. Chen, *Advanced Functional Materials*, 2015, **25**, 872-882.
184. J. Fu, Z. P. Cano, M. G. Park, A. Yu, M. Fowler and Z. Chen, *Adv Mater*, 2017, **29**.
185. J. Fu, F. M. Hassan, C. Zhong, J. Lu, H. Liu, A. Yu and Z. Chen, *Adv Mater*, 2017, **29**.
186. Y. Jiang, Y.-P. Deng, J. Fu, D. U. Lee, R. Liang, Z. P. Cano, Y. Liu, Z. Bai, S. Hwang, L. Yang, D. Su, W. Chu and Z. Chen, *Advanced Energy Materials*, 2018, 8, 1702900.
187. W. Liu, J. Zhang, Z. Bai, G. Jiang, M. Li, K. Feng, L. Yang, Y. Ding, T. Yu, Z. Chen and A. Yu, *Advanced Functional Materials*, 2018, **28**, 1706675.
188. S. Gadipelli, T. Zhao, S. A. Shevlin and Z. Guo, *Energy & Environmental Science*, 2016, **9**, 1661-1667.

189. X.-Y. Yu, Y. Feng, B. Guan, X. W. Lou and U. Paik, *Energy & Environmental Science*, 2016, **9**, 1246-1250.
190. X. Y. Yu, L. Yu, H. B. Wu and X. W. Lou, *Angewandte Chemie International Edition*, 2015, **54**, 5331-5335.
191. O. N. Risset, E. S. Knowles, S. Ma, M. W. Meisel and D. R. Talham, *Chemistry of Materials*, 2012, **25**, 42-47.
192. C. L. Carvalho, A. T. Silva, L. J. Macedo, R. A. Luz, J. M. Moita Neto, U. P. Rodrigues Filho and W. Cantanhede, *International Journal of Molecular Sciences*, 2015, **16**, 14594-14607.
193. Y. Liao, K. Pan, Q. Pan, G. Wang, W. Zhou and H. Fu, *Nanoscale*, 2015, **7**, 1623-1626.
194. F. Calle-Vallejo, N. G. Inoglu, H.-Y. Su, J. I. Martínez, I. C. Man, M. T. M. Koper, J. R. Kitchin and J. Rossmeisl, *Chemical Science*, 2013, **4**, 1245.
195. J. Suntivich, K. J. May, H. A. Gasteiger, J. B. Goodenough and Y. Shao-Horn, *Science*, 2011, **334**, 1383-1385.
196. J. K. Easton, *Journal (Water Pollution Control Federation)*, 1967, 1621-1625.
197. M. Kuang, Q. Wang, P. Han and G. Zheng, *Advanced Energy Materials*, 2017, **7**, 1700193.
198. D. Y. Chung, S. W. Jun, G. Yoon, H. Kim, J. M. Yoo, K. S. Lee, T. Kim, H. Shin, A. K. Sinha, S. G. Kwon, K. Kang, T. Hyeon and Y. E. Sung, *Journal of the American Chemical Society*, 2017, **139**, 6669-6674.
199. J. K. Easton, *Journal (Water Pollution Control Federation)*, 1967, **39**, 1621-1625.
200. D. Y. Chung, S. W. Jun, G. Yoon, H. Kim, J. M. Yoo, K.-S. Lee, T. Kim, H. Shin, A. K. Sinha, S. G. Kwon, K. Kang, T. Hyeon and Y.-E. Sung, *Journal of the American Chemical Society*, 2017, **139**, 6669-6674.
201. Y. Zheng, Y. Jiao, L. H. Li, T. Xing, Y. Chen, M. Jaroniec and S. Z. Qiao, *ACS nano*, 2014, **8**, 5290-5296.
202. Y. Yang, Z. Lun, G. Xia, F. Zheng, M. He and Q. Chen, *Energy & Environmental Science*, 2015, **8**, 3563-3571.
203. J. Deng, P. Ren, D. Deng and X. Bao, *Angewandte Chemie International Edition*, 2015, **54**, 2100-2104.
204. Y. Liu, H. Yu, X. Quan, S. Chen, H. Zhao and Y. Zhang, *Scientific Reports*, 2014, **4**, 6843.
205. M. Ye, M. Wang, D. Zheng, N. Zhang, C. Lin and Z. Lin, *Nanoscale*, 2014, **6**, 3576-3584.
206. T. Zhang, M.-Y. Wu, D.-Y. Yan, J. Mao, H. Liu, W.-B. Hu, X.-W. Du, T. Ling and S.-Z. Qiao, *Nano Energy*, 2018, **43**, 103-109.
207. Y. Zhu, W. Zhou, Y. Chen, J. Yu, M. Liu and Z. Shao, *Advanced Materials*, 2015, **27**, 7150-7155.
208. X. Jia, Y. Zhao, G. Chen, L. Shang, R. Shi, X. Kang, G. I. N. Waterhouse, L.-Z. Wu, C.-H. Tung and T. Zhang, *Advanced Energy Materials*, 2016, **6**, 1502585.

209. F. Wang, Y. Sun, Y. He, L. Liu, J. Xu, X. Zhao, G. Yin, L. Zhang, S. Li, Q. Mao, Y. Huang, T. Zhang and B. Liu, *Nano Energy*, 2017, **37**, 1-6.
210. J. Masa, P. Weide, D. Peeters, I. Sinev, W. Xia, Z. Sun, C. Somsen, M. Muhler and W. Schuhmann, *Advanced Energy Materials*, 2016, **6**, 1502313.
211. C. Xiao, Y. Li, X. Lu and C. Zhao, *Advanced Functional Materials*, 2016, **26**, 3515-3523.
212. J. Ren, M. Antonietti and T.-P. Fellinger, *Advanced Energy Materials*, 2015, **5**, 1401660.
213. A. Aijaz, J. Masa, C. Rosler, W. Xia, P. Weide, A. J. Botz, R. A. Fischer, W. Schuhmann and M. Muhler, *Angewandte Chemie International Edition*, 2016, **55**, 4087-4091.
214. S. Chen, J. Duan, P. Bian, Y. Tang, R. Zheng and S.-Z. Qiao, *Advanced Energy Materials*, 2015, **5**, 1500936.
215. L. Yang, J. Yu, Z. Wei, G. Li, L. Cao, W. Zhou and S. Chen, *Nano Energy*, 2017, **41**, 772-779.
216. X. Xu, C. Su, W. Zhou, Y. Zhu, Y. Chen and Z. Shao, *Advanced Science*, 2016, **3**, 1500187.
217. T. Y. Ma, S. Dai, M. Jaroniec and S. Z. Qiao, *Journal of the American Chemical Society*, 2014, **136**, 13925-13931.
218. T. Y. Ma, S. Dai, M. Jaroniec and S. Z. Qiao, *Angewandte Chemie International Edition*, 2014, **53**, 7281-7285.
219. Q. Ma, C. Hu, K. Liu, S.-F. Hung, D. Ou, H. M. Chen, G. Fu and N. Zheng, *Nano Energy*, 2017, **41**, 148-153.
220. H. B. Wu, B. Y. Xia, L. Yu, X.-Y. Yu and X. W. Lou, *Nature Communications*, 2015, **6**, 6512.
221. A. M. El-Sawy, I. M. Mosa, D. Su, C. J. Guild, S. Khalid, R. Joesten, J. F. Rusling and S. L. Suib, *Advanced Energy Materials*, 2016, **6**, 1501966.
222. X. Liu, W. Liu, M. Ko, M. Park, M. G. Kim, P. Oh, S. Chae, S. Park, A. Casimir, G. Wu and J. Cho, *Advanced Functional Materials*, 2015, **25**, 5799-5808.
223. H. W. Park, D. U. Lee, M. G. Park, R. Ahmed, M. H. Seo, L. F. Nazar and Z. Chen, *ChemSusChem*, 2015, **8**, 1058-1065.
224. X. Xu, H. Liang, F. Ming, Z. Qi, Y. Xie and Z. Wang, *ACS Catalysis*, 2017, **7**, 6394-6399.
225. D. Friebel, M. W. Louie, M. Bajdich, K. E. Sanwald, Y. Cai, A. M. Wise, M. J. Cheng, D. Sokaras, T. C. Weng, R. Alonso-Mori, R. C. Davis, J. R. Bargar, J. K. Norskov, A. Nilsson and A. T. Bell, *Journal of the American Chemical Society*, 2015, **137**, 1305-1313.